Title
Estimating Near-Surface Elastic Structure from Low-Frequency Seismic Noise

Permalink
https://escholarship.org/uc/item/22r26284

Author
Wang, Jiong

Publication Date
2021

Peer reviewed|Thesis/dissertation

UNIVERSITY OF CALIFORNIA

Santa Barbara

Estimating Near-Surface Elastic Structure from Low-Frequency Seismic Noise

A dissertation submitted in partial satisfaction of the

requirements for the degree Doctor of Philosophy

in Earth Science

by

Jiong Wang

Committee in charge:

Professor Toshiro Tanimoto, Chair

Professor Chen Ji

Professor Robin Matoza

September 2021

The dissertation of Jiong Wang is approved.

Chen Ji

Robin Matoza

Toshiro Tanimoto, Committee Chair

August 2021

Estimating Near-Surface Elastic Structure from Low-Frequency Seismic Noise

by

Jiong Wang

ACKNOWLEDGEMENTS

Five years of my PhD degree have passed by quicker than I initially anticipated back in 2016, especially working in a desirable and supportive environment. First and foremost, none of my doctoral work would be possible without the guidance of my advisor, Professor Toshiro Tanimoto. Through his own action, he has continuously shown me what it takes to be an independent researcher with a strong sense of scientific curiosity, which I believe to be one of the most important traits as a scientist. I am grateful for Toshiro's advice and support throughout these five years. Besides my advisor, I also want to thank my other committee members, Professor Chen Ji and Professor Robin Matoza. From either my milestone exams, or just daily conversations, they have provided me great suggestions to better improve my work, and to think of ideas that I might have missed. The same appreciation goes to Professor Ralph Archuleta and Professor Zachary Eilon. Both have always been generous with their time and helped me edit my manuscripts.

Second, I want to thank my fellow group members, Aaron Anderson, Anne Lamontagne and Han Xiao, and all the other graduate students, especially ones that I have shared office with. It is always helpful to have others provide unique perspectives, and sometimes "distract" me in a good way. I also want to thank staff in the department, who has ensured me to maximize my time and efforts on my PhD study and research, without worrying about other administrative duties.

Lastly, I want to thank my parents back in China. Although we are separated by the Pacific Ocean, their constant support and care have made these past years much easier and pleasant. I could not have done everything in my life without them.

VITA OF JIONG WANG
August 2021

EDUCATION

Doctor of Philosophy in Earth Science August 2021

University of California, Santa Barbara
Advisor: Professors Toshiro Tanimoto
Dissertation: “Estimating Near-Surface Elastic Structure from Low-Frequency Seismic Noise”

Bachelor of Science, Earth Science

University of California, Santa Barbara June 2016
Graduate with Highest Honors (Top 2.5%)

PROFESSIONAL EMPLOYMENT

09/16-Present	Graduate Student Researcher, Dept. of Earth Sciences, UCSB
09/16-Present	Teaching Assistant, Dept. of Earth Sciences, UCSB

PUBLICATIONS

6. **Wang, J**., and Tanimoto, T. Layered Structure and Vs30 at Colocated Pressure and Seismic Stations in the Transportable Array, ***In Prep***.

5. Tanimoto, T., and **Wang, J**. An Inversion Algorithm for Deriving Shallow Structure using Co-located Wind, Pressure, and Seismic Data. *Journal of Geophysical Research: Solid Earth*, 2020.

4. **Wang, J**., and Tanimoto, T. Estimating Near-Surface Rigidity from Low-Frequency Noise using Co-located Pressure and Horizontal Seismic Data. *Bulletin of the Seismological Society of America*, 2020.

3. Tanimoto, T., and **Wang, J**. Shallow Elasticity Structure from Colocated Pressure and Seismic Stations in the Piñon Flat Observatory and Estimation of Vs30. *Geophysical Journal International*, 2020.

2. Tanimoto, T., and **Wang, J**. Theory for Deriving Shallow Elasticity Structure from Colocated Seismic and Pressure Data. *Journal of Geophysical Research: Solid Earth*, 2019.

1. Tanimoto, T., and **Wang, J**. Low-Frequency Seismic Noise Characteristics from the Analysis of Co-located Seismic and Pressure Data. *Journal of Geophysical Research: Solid Earth*, 2018.

AWARDS

- Geophysics Award, UC Santa Barbara, 2020
- Archuleta Family Award, UC Santa Barbara, 2019
- SSA Student Travel Grant, Seismological Society of America, 2019
- Alumni Graduate Award for Research Excellence, UC Santa Barbara, 2018, 2021
- Outstanding Graduating Senior, UC Santa Barbara, 2016
- Outstanding Academic Achievement, UC Santa Barbara, 2016

FIELDS OF STUDY

Major Field: Seismology

Studies the interaction between the low-frequency seismic noise and atmospheric pressure changes, and utilize such data to understand near-surface elastic structure for seismic hazards analysis.

ABSTRACT

Estimating Near-Surface Elastic Structure from Low-Frequency Seismic Noise

by

Jiong Wang

When large atmospheric pressure variations occur at the Earth's surface, the solid Earth deforms elastically in response. Low-frequency seismic data record such deformations. This thesis provides a better understanding of this near-surface deformation and its applications with data from the USArray Transportable Array (TA) stations after 2012.

The two main sets of data we use are: low-frequency seismic signals, recorded on the stations' broadband seismometers, and atmospheric pressures on collocated pressure sensors. We observe high coherence between seismic noise signals and pressure variations in their power spectral densities (PSDs) in the frequency band between 0.01 and 0.05 Hz. When atmospheric pressure variations are sufficiently large, recorded seismic signals varies alongside pressure data. The ratios between seismic and pressure data can be formulated to solve for near-surface elastic structure, especially the shear-modulus. Knowledge of the near-surface elastic structure is important for its application on seismic hazard and ground motion prediction studies.

We analyze data from over nine hundred TA stations from 2012 to 2019, spanning across the Central and Eastern US (CEUS) and Alaska. The two interconnected methods we develop and use for this dataset are the half-space method and the layered inversion method.

Both methods, founded with similar fundamental backgrounds, regard the excitation source as a propagating plane pressure wave on the surface that generates ground deformation. The half-space model assumes a homogeneous medium under the surface, whereas the layered model assumes a vertically heterogeneous medium. In essence, the half-space model is a unique case of the layered model. The former permits straightforward estimations of near-surface shear-modulus at fixed frequencies, but it lacks depth resolution to constrain important parameters of seismic hazards such as Vs30—the averaged shear-wave velocity down to 30 meters deep. In contrast, the layered inversion allows to estimate Vs30 by utilizing data at multiple frequencies from 0.01 to 0.05 Hz and resulting layered velocity models.

Our results for the TA stations indicate that the two methods can resolve unique geological regions such as the Appalachian Mountains, and the Mississippi Alluvium Plain. For the Appalachian Mountains, where the bedrock is likely to be near the surface, our results indicate fast Vs30 at stations located in the area. For the Mississippi Alluvium Plain, known for thick alluvial sediments near the surface, our results demonstrate slow Vs30 at stations there. Large-scale geology maps and Vs30 models also corroborate our results. Our estimated Vs30s agree with mapped Quaternary sediment depths: fast Vs30 stations are often associated with areas categorized as thin sediment, while slow Vs30 stations are observable at locations with thick underlying sediment.

TABLE OF CONTENTS

1 Introduction

During periods without earthquake signals, broadband seismometers continuously record data as “seismic background noise”. At different frequency bands, certain sources of seismic noise become dominant and surpass other sources of noise. Figure 1 presents the “New Low Noise Model” by Peterson (1993), which is representative of the seismic noise spectrum recorded at a quiet (thus “low noise”) broadband seismic station. At very low frequencies ($<10^{-3}$ Hz, labeled as “Atmospheric effects”), seismic noise is mostly caused by density change in the atmosphere (e.g., Tanimoto et al., 2015), where the mass of the atmosphere above a station changes greatly (e.g., Bormann and Wielandt, 2013). At low frequencies ($\sim 10^{-2}$ Hz, labeled as “Hum”), effect of the Earth’s free oscillation becomes dominant (e.g., Suda et al., 1998; Tanimoto et al., 1998). The excitation mechanism is hypothesized to be either pressure fluctuations in the atmosphere or the ocean infragravity waves. Two peaks in the noise spectrum at $\sim 10^{-1}$ Hz and $\sim 2*10^{-1}$ Hz (labeled as “Primary MS” and “Secondary MS”) are known as ocean microseism. Primary microseism is associated with the interaction between ocean waves and the solid Earth, whereas secondary microseism is associated with the interaction of opposing ocean waves. Ocean microseism has been widely studied (e.g., Longuet-Higgins, 1950). At high frequencies (> 1 Hz, labeled as “Cultural Noise”), seismic noise is mostly dominated by human activities such as the coupling between the traffic or machine with the solid Earth. Clear diurnal variations can be observed for seismic noise at high frequencies (McNamara and Buland, 2004).

In this dissertation, we study a unique type of seismic noise, which is signals generated by atmospheric pressure variations. Atmospheric pressure changes on the surface can cause deformation on the ground. In the half-space source model proposed in Sorrells (1971), where elastic structure is homogenous below the surface, wind-related moving pressure waves on the surface generate ground deformation. The amount of deformation depends on the near-surface elastic structure. Such interaction can be observed in data through correlations of collocated pressure and seismic power spectral densities (PSDs) between 0.01 and 0.05 Hz (Tanimoto and Wang, 2018).

The presence of pressure-related seismic signals at low frequencies has been known and studied for several decades. Efforts are initially made to understand the interaction between pressure and ground in order to remove such “unwanted” signals by data processing or preemptively circumvented by installing seismic sensors at depths (e.g., McDonald et al., 1971; Ziolkowski, 1973; Zürn et al., 2007). Similar work on reducing pressure-caused seismic noise is conducted on ocean-bottom-seismometers because such noise can disrupt earthquake signals at low frequencies (Crawford et al., 1991). Researchers also noticed that at low frequencies, two horizontal seismic components have much larger pressure-caused noise than the vertical component due to the tilt effects (Rodgers, 1968); therefore, the vertical seismic data are typically preferred due to higher signal-to-noise ratios. However, the half-space model by Sorrells (1971) suggests the amount of pressure-caused seismic noise reflects the elastic structure underneath the seismic station, which provides scientific significance of such noise signals. Recently, estimating near-surface structure information using pressure-caused seismic signal has gained more attention due to its ability to resolve structure on Mars with a single collocated station (Kenda et al., 2017; Lognonné et al., 2020). However, besides the early theoretical work by Sorrells (1971), Sorrells and Goforth (1973), and continued studies on low-frequency seismic noise (e.g., Beauduin et al., 1996; McNamara and Buland, 2004; De Angelis and Bodin, 2012; Wolin et al., 2015; Hutt et al., 2017), there is limited quantitative understanding of this phenomenon, mainly due to the scarcity of high-quality pressure sensors collocated with broadband seismometers. Collocation of pressure and seismic sensors is essential for such studies, because seismic and pressure data become incoherent with distances greater than several kilometers (Ziolkowski, 1973). The EarthScope Transportable Array (TA) deployment has significantly improved the shortage of collocated stations, with hundreds of seismic stations equipped with high-quality pressure sensors since mid-2011 (Tytell et al., 2016). Using this unprecedented dataset from these stations' collocated sensors, we can extensively investigate the process of atmosphere-ground coupling and estimate near-surface elastic structures at hundreds of new locations. Sensitivity kernels of shear-modulus at 0.01 to 0.05 Hz are mostly confined in the shallowest tens of meters, which illustrates the near-surface nature of our results.

Near-surface elastic structures in the uppermost crust (tens of meters) are essential for seismic hazard and ground motion prediction studies (e.g., Borcherdt, 1994) because soft sedimentary layers can amplify incoming seismic waves and subsequently cause more ground shaking and damage. Intuitively, the ability of our approach to resolve near-surface structure is straightforward: because of distinct site conditions, different seismic stations respond differently to surface pressure variations. Less rigid ground experiences major deformations, while more rigid ground experiences minor deformations. Scholars have applied similar principles to resolve shallow structures at the bottom of the ocean (Crawford et al., 1991) and on Mars (Kenda et al., 2017). Traditionally, obtaining accurate information on the near-surface elastic structure can be challenging and costly, as it often involves laborious field deployment and unique setup such as sonic logging and dense geophone arrays. Our approach is a single-station approach that utilizes natural environmental seismic noise; therefore, it provides an efficient and economical tool to estimate important parameters for the near-surface structure such as Vs30—the averaged shear-wave velocity down to 30 meters. In a separate study (Tanimoto and Wang, 2020), the estimated Vs30 at collocated stations in the Piñon Flat Observatory are consistent with nearby measured velocity profiles, which demonstrates the reliability of our method.

This thesis has the following four chapters. The first chapter introduces the inversion method and explains the method in detail at two TA stations. In the second chapter, we obtain half-space shear-modulus results at 784 TA stations, focusing on the stations' horizontal seismic data and pressure data. In the third chapter, we estimate Vs30 at 744 TA stations with the inversion method and compare the results with large-scale surficial geology maps. The fourth chapter provides a brief discussion on the future scientific investigations regarding the low-frequency seismic noise generated by the atmospheric pressure variations.

Chapter One explains the background theory of the inversion method, and present specific steps of the inversion method at two TA stations, KMSC and Y22D. Low-frequency collocated data across different frequency bins from 0.01 to 0.05 Hz reveal information at different depths based on sensitivity kernels. Computed through numerical differentiation, sensitivity kernels suggest that data are more sensitive to shear-modulus and bulk-modulus than to density. For the inversion, we only focus on data during time intervals with high coherence and large pressure variations to ensure the data represent the land-atmosphere coupling.

From vertically heterogeneous starting models constructed from half-space models at fixed frequencies, we aim to fit the surface observable η(f)—the ratio between vertical seismic PSDs and pressure PSDs. We compute each station's theoretical η(f) based on the updated layered model by integrating the minors of the equations of motion. After determining the final model by examining variance reduction, we can estimate Vs30 from the layered velocity models. Altogether, this chapter provides a foundation for the following two chapters.

Chapter Two presents the half-space shear-modulus at 0.02 Hz at 784 TA stations from 2012 to 2019. We adopt the source model in Sorrells (1971) and formulations in Tanimoto and Wang (2018) and estimate half-space shear-modulus by computing ratios between horizontal seismic and pressure PSDs. For each station, we analyze data yearly and apply data culling procedures, including coherence and pressure threshold.

We specifically stress the idea of only using the horizontal components of seismic data. At low frequencies (<0.05 Hz), horizontal seismic signals have much higher amplitude than vertical seismic signals due to the tilt effect (Rodgers, 1968). However, from formulations, this amount of tilt is still a function of the elastic structure. Meanwhile, because of higher amplitudes on the horizontal signals, the effects of other noise sources in this frequency band become less significant. In all, it is more advantageous to apply the half-space model with the tilt-dominated horizontal seismic data at low frequencies.

None of these 784 stations had any on-site estimated near-surface structure before this study. Our results are consistent with prior understandings of two unique geological regions in the Eastern US: the Appalachian Mountains and the Mississippi Alluvial Plain. We convert shear-modulus into shear-wave velocity (Vs) by empirical equations (Gardner et al., 1974; Brocher, 2005; Boore, 2016). We compare half-space Vs with various large-scale Vs30 models based on proxies such as topographic slopes and surface geology (Wald and Allen, 2007; Goulet et al., 2014). Despite some scatters in the correlation, large-scale trends agree between our results and various Vs30 models.

Because the half-space model is fundamentally a unique case of the layered model in the first chapter and share similar background theory, to avoid redundance, we do not include a standalone chapter on the half-space model theory. We recommend the comprehensive half-space methodology in Tanimoto and Wang (2018) as a supplement of this thesis for those with interests in the subject.

Chapter Three demonstrates how we estimate the Vs30 at 744 TA stations from the layered model with the same dataset from the previous chapter. Following the method introduced in the first chapter, this chapter also highlights the comparison between the layered model and the half-space model, and the distribution of peak depths of sensitivity kernels. Unlike the second chapter that uses the dataset on a yearly basis, here we analyze all data at each station for the entire duration. For all stations, we first select stations with good data quality for the inversion by the quality control step, which includes coherence and pressure threshold, the number of valid data points, and the number of valid frequencies. Second, we build station-specific starting models based on half-space results at fixed frequencies by aligning elastic parameters at peak depths of sensitivity kernels. We then run the inversion for nine iterations at all stations and at two cases of frequency ranges: between 0.01 and 0.05 Hz and between 0.01 and 0.04 Hz. Lastly, we set a variation reduction threshold of 5% to determine the final model out of nine iterations, meaning each additional iteration will only be considered if the misfit improvement is more than 5%. In the end, we estimate Vs30 from the final model.

We discover relationships between Vs30 and sediment depths by comparing our Vs30 results with various large-scale surficial geology maps, such as Quaternary sediment depths in Soller and Garrity (2018) and surficial materials units in Soller et al. (2009). We group TA stations with polygons on each map unit. Fast Vs30 stations often gather in units categorized with thin underlying sediment, while slower Vs30 stations are more likely to appear in regions categorized with thick sediments. We also observe a high degree of similarity between the half-space Vs at 0.02 Hz and layered Vs30. This is not a surprising result, given that sensitivity kernels at 0.02 Hz often have peak depths of 20 meters, and Vs30 is an averaged quantity for the uppermost 30 meters. Hence, half-space Vs at 0.02 Hz is comparable to Vs30. Although the inversion method is preferred due to its ability to resolve vertically heterogonous velocity models, the half-space model can still be a valid tool to understand the near-surface structure given its straightforward computation process.

1.1 Reference

Beauduin, R., P. Lognonné, J. P. Montagner, S. Cacho, J. F. Karczewski, and M. Morand (1996). The effects of the atmospheric pressure changes on seismic signals or how to improve the quality of a station, *Bulletin of the Seismological Society of America*. 86, no. 6, 1760.

Boore, D. M. (2016). Determining generic velocity and density models for crustal amplification calculations, with an update of the Boore and Joyner (1997) generic site amplification for graphic site amplification, *Bulletin of the Seismological Society of America*. 106, no. 1, 313, doi: 10.1785/ 0120150229.

Bormann, P., and E. Wielandt (2013). Seismic signals and noise, Chapter 4, in *New Manual of Seismological Observatory Practice (NMSOP-2)*, P. Bormann (Editor), IASPEI, GFZ German Research Centre for Geosciences, Potsdam, Germany, doi: 10.2312/GFZ.NMSOP-2.

Brocher, T. M. (2005). Empirical relations between elastic wavespeeds and density in the earth’s crust, *Bulletin of the Seismological Society of America*. 95, no. 6, 2081–2092, doi: 10.1785/0120050077.

De Angelis, S., and P. Bodin (2012). Watching the wind: Seismic data contamination at long periods due to atmospheric pressure field induced tilting, *Bulletin of the Seismological Society of America*. 102, no. 3, 1255–1265, doi: 10.1785/0120110186.

Gardner, G., L. W. Gardner, and A. R. Gregory (1974). Formation velocity and density-the diagnostic basics for stratigraphic traps, *Geophysics.* 39, no. 6, 759–918, doi: 10.1190/1.1440465.

Goulet, C. A, T. Kishida, T. D. Ancheta, C. H. Cramer, R. B. Darragh, W. J. Silva, Y. M. Hashash, J. Harmon, J. P. Stewart, K. E. Wooddell, et al. (2014). *PEER NGA-East database, PEER Rept. 2014/17*, https://peer.berkeley.edu/research/nga-east/products (last accessed April 2021).

Hutt, C. R., A. T. Ringler, and L. S. Gee (2017). Broadband seismic noise attenuation versus depth at the Albuquerque seismological laboratory, *Bulletin of the Seismological Society of America*. 107, no. 3, 1402–1412, doi: 10.1785/0120160187.

Lognonné, P., Banerdt, W.B., Pike, W.T. et al (2020). Constraints on the shallow elastic and anelastic structure of Mars from InSight seismic data. *Nature Geoscience*. 13, 213–220, doi:10.1038/s41561-020-0536-y.

Longuet-Higgins, M. S. (1950). A theory of the origin of microseisms. Philosophical Transactions of the Royal Society of London, *Series A: Mathematical, Physical and Engineering Sciences*, 243(857), 1–35, doi:10.1098/rsta.1950.0012.

McDonald, J.A., E. J. Douze and Eugene Herrin (1971). The Structure of Atmospheric Turbulence and its Application to the Design of Pipe Arrays, *Geophysical Journal International*, 26, no. 1-4, December 1971, 99–109, doi:10.1111/j.1365-246X.1971.tb03385.x

McNamara, D. E., and R. P. Buland (2004). Ambient noise levels in the continental United States, *Bulletin of the Seismological Society of America*. 94, no. 4, 1517–1527, doi: 10.1785/012003001.

Peterson, J. R. (1993). Observations and modeling of seismic background noise (*Open-File Rept.*): U.S. Geol. Survey. 93-322, doi: 10.3133/ofr93322.

Rodgers, P. W. (1968). The response of the horizontal pendulum seismometer to Rayleigh and love waves, tilt, and free oscillations of the earth, *Bulletin of the Seismological Society of America*. 58, no. 5, 1385–1406.

Sorrells, G. G. (1971). A preliminary investigation into the relationship between long-period seismic noise and local fluctuations in the atmospheric pressure field, *Geophysical Journal International*. 26, nos. 1/4, 71–82, doi: 10.1111/j.1365-246X.1971.tb03383.x.

Sorrells, G. G., and T. T. Goforth; Low-frequency earth motion generated by slowly propagating partially organized pressure fields. *Bulletin of the Seismological Society of America* 1973; 63 (5): 1583–1601.

Suda, N., K. Nawa, and Y. Fukao (1998). Earth's background free oscillations, *Science* 279, no. 5359, 2089–2091, doi: 10.1126/science.279.5359.2089.

Tanimoto, T., J. Um, K. Nishida, and N. Kobayshi (1998). Earth's continuous oscillations observed on seismically quiet days, *Geophysical Research Letters*. 25, no. 10, 1553–1556, doi: 10.1029/98GL01223.

Tanimoto, T., Heki, K., and J. Artru-Lambin (2015). 4.16 - Interaction of Solid Earth, Atmosphere and Ionosphere. In G. Schubert (Ed.), *Treatise on Geophysics* (2nd ed., pp. 421–443). Oxford: Elsevier, doi: 10.1016/B978-0-444-53802-4.00083-X.

Tanimoto, T., and J. Wang (2018). Low-frequency seismic noise characteristics from the analysis of co-located seismic and pressure data, *Journal of Geophysical Research: Solid Earth*. 123, no. 7, 5853–5885, doi: 10.1029/2018JB015519.

Tytell, J., F. Vernon, M. Hedlin, C. de Groot Hedlin, J. Reyes, B. Busby, K. Hafner, and J. Eakins (2016). The USArray transportable array as a platform for weather observation and research, *Bulletin of the American Meteorological Society*. 97, 603–619, doi: 10.1175/BAMS-D-14- 00204.1.

Wald, D., and T. Allen (2007). Topographic slope as a proxy for seismic site conditions and amplification, *Bulletin of the Seismological Society of America*. 97, no. 5, 1379–1395, doi: 10.1785/0120060267.

Wolin, E., S. van der Lee, T. Bollmann, D. Wiens, J. Revenaugh, F. Darbyshire, A. Frederiksen, S. Stein, and M. Wysession (2015). Seasonal and diurnal variations in long-period noise at spree stations: The influence of soil characteristics on shallow stations performance, *Bulletin of the Seismological Society of America*. 105, no. 5, 2433–2452, doi: 10.1785/0120150046.

Ziolkowski, A (1973). Prediction and suppression of long-period nonpropagating seismic noise. *Bulletin of the Seismological Society of America* 63, no. 3, 937–958.

Zürn, W, J. Exß, H. Steffen, C. Kroner, T. Jahr and M. Westerhaus (2007). On reduction of long-period horizontal seismic noise using local barometric pressure, *Geophysical Journal International*, 171, no. 2, 780–796, doi:10.1111/j.1365-246X.2007.03553.x.

1.2 Figure

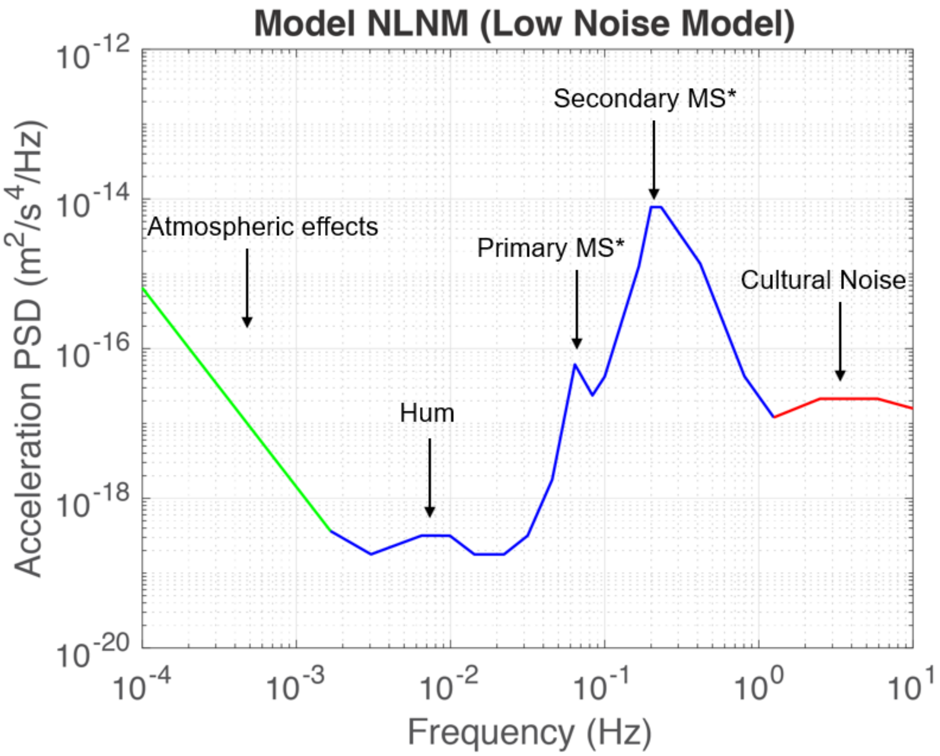

Figure 1. Seismic noise spectrum. Modified from Petersons (1993) "New Low Noise Model". MS: microseism.

2 Theory for Deriving Shallow Elasticity Structure from Colocated Seismic and Pressure Data

This chapter appeared in this form in:

Tanimoto, T., and J. Wang (2019). Theory for deriving shallow elasticity structure from colocated seismic and pressure data, *Journal of Geophysical Research: Solid Earth*. 124, no. 6, 5811–5835, doi: 10.1029/2018JB017132.

2.1 Abstract

Colocated seismic and pressure data are available at many seismic stations in the world. For frequencies approximately between 0.01 and 0.05 Hz, colocated data show evidence of strong coupling between the atmosphere and the solid Earth, especially when pressure is high. Coherence between vertical seismic data and pressure is often higher than 0.9. Such data provide information for shallow structure in the upper 50–100 m because they show how the Earth responds to surface pressure changes. We present the basic theory and an inversion scheme for shallow structure using surface observables $\eta(f) = S_z/S_p$ where f is frequency and S_z and S_p are the power spectral densities of vertical seismic data and of surface pressure data. A vertically heterogeneous medium is assumed beneath a station where density, P wave velocity, and S wave velocity change with depth. We show that the integration of the minors for the equations of motion gives a fast algorithm to compute $\eta(f)$. Using numerical differentiation, we derive depth sensitivity kernels for $\eta(f)$ with which we invert $\eta(f)$ for shallow structure, just like we invert phase velocity of surface waves for the Earth structure. Depth sensitivity kernels show that if we take density, bulk modulus, and rigidity as independent parameters, $\eta(f)$ has no sensitivity to density structure, making it mainly a function of two elastic constants. We present examples of inversion based on this formulation.

2.2 Introduction

Understanding the characteristics of seismic noise and retrieving Earth structure from the cross correlation of seismic noise have been active research fields in the last 20 years. But most studies relied on the ocean-generated seismic noise. In this study, we focus on the atmosphere-generated seismic noise and present an approach to derive shallow structure of the Earth.

One of the motivations to develop such an approach is an increasing number of colocated seismic and pressure sensors at many sites in the world. One example is the EarthScope Transportable Array (hereafter TA) after the year 2011 which typically operated about 500 colocated stations at a given time (e.g., Tytell et al., 2016). These colocated data allow us to identify the frequency range of strong coupling between the atmosphere and the solid Earth and provide us information on how the solid Earth responds to surface pressure changes.

Study on atmosphere-generated seismic noise was conducted quite actively around 1970 (e.g., Herrin et al., 1969; McDonald et al., 1971; Savino et al., 1972; Sorrells, 1971; Sorrells et al., 1971; Sorrells & Goforth, 1973) but has decreased in number over the following few decades. This topic seems to be gaining attention in the last 10 years, perhaps partly because of availability of a large number of colocated stations (e.g., De Angelis & Bodin, 2012; Hutt et al., 2017; Tanimoto & Wang, 2018; Wolin et al., 2015) and also because of its potential application to planetary seismology (Kenda et al., 2017). We note that most of these studies adopted a homogeneous half-space model in their analysis that was derived by Sorrells (1971). Exceptions are Sorrells and Goforth (1973) and Kenda et al. (2017), which applied an analysis for a multilayered medium. But even in these studies, the approach was focused on the forward modeling for a multilayered medium.

Our problem is similar to the compliance problem of ocean bottom seismology (Crawford et al., 1991, 1998). There are, however, distinct differences in the nature of problems; for ocean bottom observations of seismic noise, the two main sources are the oceanic infragravity waves and the ocean currents that cause ground tilt on the seafloor (e.g., Crawford & Webb, 2000). For our problem, the main sources are surface pressure changes by atmospheric wind, which is composed of the main stream flow and turbulence associated with it. The two problems can become similar under certain conditions and that was why Crawford et al. (1991) could use the formulas from Sorrells (1971). However, there is typically a difference by a factor of about 10–100 in the speed of pressure waves that excite deformations in the solid Earth. This difference leads to an important difference in depth resolution of structure as the lateral source speed on the surface is proportional to the depth extent of sensitivity kernels; in our case the depth resolution is typically in the upper 50–100 m, while for the ocean bottom data the depth resolution can reach 1–10 km. This suggests that the two phenomena may be similar but are in different parameter ranges. We will discuss them in more detail in the discussion.

The main goal of this paper is to present an inverse scheme for shallow crustal structure using colocated seismic and pressure data on Earth's surface. Our scheme is based on surface observables $\eta(f) = S_z/S_p$ where f is frequency and S_z and S_p are the power spectral densities (PSDs) of vertical seismic data and of surface pressure data. We will first describe how to compute η(f) for a multilayered medium as the forward problem and then show how to invert η(f) for shallow structure of the Earth.

This paper proceeds in the following order; in section 2 we report on the coherence between seismic and pressure data that indicates strong coupling between the atmosphere and the solid Earth. This occurs in a frequency band about 0.01–0.05 Hz. We develop our inverse scheme for this frequency band because of this observation. In section 3, we describe the basic formulation for the forward modeling in a multilayered medium. It is essentially the same with the formulation for Rayleigh waves or the P-SV-type waves in a layered medium (e.g., Aki & Richards, 2002, Chapman, 2004, Kennett, 1983). As we mentioned above, extension to a multilayered medium was already shown by Sorrells and Goforth (1973) and Kenda et al. (2017) but they used the static approximation for the response of the medium. We show such an approximation is not necessary. But comparison between our numerical results for finite-frequency calculations and analytical results using the static approximations (Sorrells, 1971) shows an excellent match. It indicates that the phenomenon is a quasi-static phenomenon, meaning that pressure source is at finite frequencies (0.01–0.05 Hz) but the deformation is so slow that the medium response may be approximated by a static approximation. In section 4, we add the effect of tilt in our formulation that has been known to be important in the frequency band of our study since the work of Rodgers (1968). In section 5 we show that integrating the minors for the equations of motion gives us an efficient algorithm to compute η(f). It speeds up the computation of depth sensitivity kernels in section 6. The most important point in section 6 is that if we take density, bulk modulus, and rigidity as independent parameters, depth sensitivity kernel for density almost disappears. This feature means that η(f) is basically a function of elasticity only. It justifies us to drop density in our inversion scheme. We present examples of inversion in section 7 and discuss our results and some important differences from ocean bottom compliance problems in section 8. We summarize our conclusion in section 9.

2.3 Coherence Between Surface Pressure and Seismic Motions

Coherence between colocated seismic and pressure data gives us important insights into the atmosphere-solid Earth interactions. Figures 1a and 1b show the coherence between vertical seismic data and surface pressure data at station KMSC, one of the TA stations in South Carolina. We compute coherence by evaluating

$$\boldsymbol{Coh(f)} = \left|\frac{\boldsymbol{E[X^*(f)Y(f)]}}{\sqrt{\boldsymbol{E[X^*(f)X(f)]E[Y^*(f)Y(f)]}}}\right| \qquad (\mathbf{1})$$

where X(f) and Y(f) are seismic and pressure spectra and E[] means ensemble averaging. In practice, we divide a 1-hr time series into 11, overlapping 10-min-long time series, by shifting the start time by 5 min for each time series. We simply take the average of these eleven spectra in order to get an estimate for the quantities with E[] in an hour. We used the same approach in Tanimoto and Wang (2018).

Figure 1a shows the raw coherence values for KMSC from the first 30 days of 2014. Different colors mean that they are from different 1-hr time series. We only plot the coherence from the (1-hr) time series that had high pressure PSD at 0.01 Hz, or more specifically S_p(0.01Hz) > 10 (Pa^2/Hz). This figure shows that coherence between 0.01 and

0.05 Hz is particularly high and supports the view that the Earth's surface is moving in sync with surface pressure in this frequency band (Figure 1d). Above 0.05 Hz, coherence generally decreases but we can still see values higher than 0.6 up to about 0.1 Hz, beyond which coherence above 0.6 are rarely seen.

Figure 1b shows the annual average of coherence; the thick black line is the mean and the area in blue indicates the range of one standard deviation (1σ). We obtained them by first computing coherence for the entire year of 2014 and computing the mean and standard deviations for each frequency. We used the same selection criterion $S_p(0.01\text{Hz}) > 10$ (Pa^2/Hz) for these results.

In Figure 1b, the effects from the primary microseism can be identified as a dip in coherence at about 0.06 Hz where the arrow is shown. Since the ocean-generated noise can affect seismic data but not pressure data, this decrease in coherence is expected when the primary microseism becomes large. But despite this dip, we can see relatively high coherence extending up to about 0.12 Hz in Figure 1b. This feature implies that there are some atmosphere-generated seismic noise up to about 0.12 Hz. We note, however, that Figures 1a and 1b were based on time series selected by the above high-pressure criterion. When pressure is low, the atmosphere-generated noise can be much smaller. In general, there seems to be competition between the ocean-generated seismic noise and the atmosphere-generated seismic noise for frequencies between about 0.05 and 0.12 Hz. But above 0.12 Hz, the sources of seismic noise seem to be entirely in the ocean (at least up to about 0.5 Hz).

Figure 1c shows a pressure-seismic plot at 0.02 Hz for KMSC from the entire year of 2014. Vertical seismic PSDs are shown by blue points, and horizontal PSDs are shown by red points. Each point is from a 1-hr time series. Horizontal PSD is a sum of PSDs from two seismic horizontal components. Green points are for the high-coherence time series; they are from the time intervals that had coherence higher than 0.8 between vertical seismic data and pressure and also higher than 0.8 between one of the horizontal data and pressure. These high-coherence points show relatively clean linear trends in this log-log plot, meaning that surface pressure is the controlling source of seismic noise. In these high-coherence time intervals, vertical displacements are literally in sync with surface pressure changes (Figure 1d). Vertical velocity is shifted by 90° in phase but coherence is the same as we define coherence as absolute value between 0 and 1.

Our analysis will focus on the quantity $\eta(f) = S_z/S_p$, the ratio between vertical seismic PSD and pressure PSD. In order to estimate this quantity from colocated data, we use the high-coherence time intervals. We find that coherence is the key parameter to reduce contamination from other sources. For example, time intervals that contain earthquake signals can be removed from our analysis using these coherence values.

These observations indicate that the best frequency band for our study is between about 0.01 and 0.05 Hz. In section 7 where we show examples of inversion, we limit the frequency range to from 0.01 to 0.04 Hz. In some cases, we believe we see the effects from the primary microseism around 0.05 Hz or even slightly below 0.05 Hz.

2.4 *Formulation*

2.4.1 Surface Pressure Source

The mathematical expression for the surface pressure source is derived here. Let us denote the surface pressure by P(x, y, t), where x and y are the coordinates on the surface and t is the time. We assume that pressure wave is a plane wave, propagating over a pair of colocated instruments, and take the propagation direction of pressure waves as the x axis. We also assume that this pressure wave spreads over the entire surface and has the same spectra everywhere on the surface. We clarify them below mathematically but these assumptions are the same with Sorrells (1971).

This problem is essentially a two-dimensional problem. We write this pressure source by a superposition of plane waves:

$$p(x,y,t) = p(x,t) = \frac{1}{2\pi}\int_{-\infty}^{\infty} \bar{P}(\omega')e^{i\omega' t - i\frac{\omega'}{c(\omega')}x} d\omega' \tag{2}$$

where the variable y drops out because we take the x axis along the direction of propagation. $\bar{P}(\omega')$ is the pressure spectra that is assumed to be the same everywhere on the surface; therefore, its dependence on *x* disappears. $c(\omega')$ is the pressure wave speed, and in general, it varies with frequency.

Fourier transformation of $p\ (x,t)$ can be written by

$$\begin{aligned} p(x,\omega) &= \int_{-\infty}^{\infty} p(x,t)e^{-i\omega t}\mathrm{d}t \\ &= \bar{P}(\omega)e^{-i\frac{\omega}{c(\omega)}x} \end{aligned} \tag{3}$$

where we used an integral expression for the delta function

$$\delta(\omega' - \omega) = \frac{1}{2\pi}\int_{-\infty}^{\infty} e^{i(\omega'-\omega)t}\mathrm{d}t \tag{4}$$

Now we transform $p(x,\omega)$ to the wavenumber *(k)* domain and define it by $P(k,\omega)$:

$$P(k,\omega) = \int_{-\infty}^{\infty} p(x,\omega)e^{ikx}\mathrm{d}x = 2\pi\bar{P}(\omega)\delta\left(k - \frac{\omega}{c(\omega)}\right) \tag{5}$$

In sections 3.2–3.4 we solve for the response of a layered medium in the frequency-wavenumber domain. This expression $P(k,\omega)$ becomes the surface boundary condition.

Equation (5) is essentially the same with the one used by Sorrells (1971) except for the fact that Sorrells (1971) assumed a nondispersive (constant) pressure wave c. Our observations show that pressure wave speed varies with frequency. The above derivation shows that Sorrell's formula can be used simply by replacing the constant pressure wave speed c by $c(\omega)$.

2.4.2 Response of a Multilayered Medium

We consider an excitation problem in an elastic, vertically heterogeneous medium caused by surface pressure source given in (5). In this paper, we mainly follow the formulations and notations by Takeuchi and Saito (1972). Equivalent formulations can also be found in other books (e.g., Aki & Richards, 2002, Chapman, 2004, Kennett, 1983).

We define the *x* axis (Figure 2) that coincides with the direction of pressure wave propagation. We define the *z* axis such that the top of the lowermost elastic half-space is at $z = 0$ and the surface of the Earth is at $z = H$. Density (ρ (z)), P wave velocity ($\alpha(z)$), and S wave velocity ($\beta(z)$) change with z between $z = 0$ and $z = H$.

We denote the displacements by $u_i(x, y, z, t)$ and the stress components by $\sigma_{ij}(x, y, z, t)$, where i and j are x, y, or z. The basic P-SV-type equations for Rayleigh waves are derived from the equations of motion (the momentum equations) and the constitutive relations of elasticity. Following Takeuchi and Saito (1972), we introduce the following four variables that need to be integrated over the depth. They are related to vertical displacement (u_z), vertical normal stress (σ_{zz}), horizontal displacement (u_x), and shear stress of xz component (σ_{xz}) and are defined by

$$y_1(z) = \bar{u}_z(k, z, \omega) \tag{6}$$

$$y_2(z) = \bar{\sigma}_{zz}(k, z, \omega) \tag{7}$$

$$y_3(z) = i\bar{u}_x(k, z, \omega) \tag{8}$$

$$y_4(z) = i\bar{\sigma}_{xz}(k, z, \omega) \tag{9}$$

Where we define the Fourier spectra of displacements and stress components by

$$\bar{u}_i(k, z, \omega) = \int_{-\infty}^{\infty}\int_{-\infty}^{\infty} u_i(x, z, t)e^{ikx-i\omega t}\mathrm{d}t\mathrm{d}x \tag{10}$$

$$\bar{\sigma}_{ij}(k, z, \omega) = \int_{-\infty}^{\infty}\int_{-\infty}^{\infty} \sigma_i(x, z, t)e^{ikx-i\omega t}\mathrm{d}t\mathrm{d}x \tag{11}$$

In a vertically heterogeneous medium, y_i's are continuous throughout the medium and satisfies a 4×4 matrix equation:

$$\frac{d\boldsymbol{y}}{dz} = \boldsymbol{A}\boldsymbol{y} \tag{12}$$

Where $\boldsymbol{y}$ is a column vector defined by $\boldsymbol{y} = (y_1, y_2, y_3, y_4)^{\mathrm{T}}$ and $\boldsymbol{A}$ is defined by

$$\boldsymbol{A} = \begin{pmatrix} 0 & \dfrac{1}{\lambda + 2\mu} & \dfrac{k\lambda}{\lambda + 2\mu} & 0 \\ -\rho\omega^2 & 0 & 0 & k \\ -k & 0 & 0 & \dfrac{1}{\mu} \\ 0 & -\dfrac{k\lambda}{\lambda + 2\mu} & 4k^2\mu\dfrac{\lambda + \mu}{\lambda + 2\mu} - \rho\omega^2 & 0 \end{pmatrix} \tag{13}$$

where ρ is density, λ is the Lame's constant, and μ is the rigidity (or shear modulus). All of them can vary with z.

2.4.3 Boundary Conditions

The boundary conditions at the surface ($z = H$) are given by

$$\begin{aligned} y_2(H) &= -P(k, \omega) = -2\pi\bar{P}(\omega)\delta\left(k - \frac{\omega}{c(\omega)}\right) \\ y_4(H) &= 0 \end{aligned} \tag{14}$$

where we used the equation (5).

We assume that the bottom half-space is homogeneous ($z \le 0$). In numerical computations, we typically use H = 500 m, which is the depth to the top of the lowermost half-space. This is also the starting depth of integrations, which we conduct toward the surface. Since ground motions generated by surface pressure turn out to be confined mostly to the uppermost 100 m, this assumption (H = 500) has had no practical significance for our numerical results. But the depth extent of ground motions could become large when the surface pressure wave speed becomes high (say c = 10 m/s). In such a case, we may need to push the homogeneous half-space to a deeper depth but such an adjustment is easy to accommodate in numerical computations.

We can write down two independent analytical solutions for equation (12) in the lowermost half-space that remain finite as $z \rightarrow -\infty$. There are also two other independent solutions that blow up as $z \rightarrow -\infty$. Among the two finite solutions, one of the solutions evaluated at $z = 0$ (top of the half-space) is given by (e.g., Takeuchi & Saito, 1972)

$$
\begin{aligned}
y_{11}(0) &= v_\alpha + k \\
y_{12}(0) &= \mu_0 \left(v_\beta + k\right)^2 \\
y_{13}(0) &= v_\beta + k \\
y_{14}(0) &= \mu_0 \left(v_\beta^2 + 2kv_\alpha + k^2\right)
\end{aligned}
\tag{15}
$$

where the first subscript 1 means the first set of solution and the second subscripts 1 − 4 follow the definitions in (6) – (9). If we write the density, P wave velocity, and S wave velocity in the lowermost half-space by ρ_0, α_0, and β_0, the variables in (15) are given by

$$
\begin{aligned}
\mu_0 &= \rho_o \beta_0^2 \\
v_\alpha &= \sqrt{k^2 - \frac{\omega^2}{\alpha_0^2}} \\
v_\beta &= \sqrt{k^2 - \frac{\omega^2}{\beta_0^2}}
\end{aligned}
\tag{16}
$$

At a later stage of analysis, we will replace k by ω/c because of the delta function in (14). Since c should be about the same order with wind speeds (typically 1–10 m/s), c is much smaller than α_0 and β_0. Therefore, v_α and v_β are real and positive quantities in our analysis.

The second set of solution may be given by (Takeuchi & Saito, 1972)

$$
\begin{aligned}
y_{21}(0) &= v_\alpha - k \\
y_{22}(0) &= \mu_0\left(v_\beta - k\right)^2 \\
y_{23}(0) &= -v_\beta + k \\
y_{24}(0) &= \mu_0\left(-v_\beta^2 + 2kv_\alpha - k^2\right)
\end{aligned}
\tag{17}
$$

2.4.4 Solutions

Starting with two independent solutions in (15) and (17), we integrate the matrix equation (12) from $z = 0$ to the surface ($z = H$). Let us denote the surface values of these integrations by ($y_{11}(H)$, $y_{12}(H)$, $y_{13}(H)$, and $y_{14}(H)$) and ($y_{21}(H)$, $y_{22}(H)$, $y_{23}(H)$, and $y_{24}(H)$). We take a linear combination of these independent solutions in order to satisfy the surface boundary conditions in (14). This means determining two coefficients A and B that satisfy

$$Ay_{12}(H) + By_{22}(H) = -P(k,\omega) \tag{18}$$

$$Ay_{14}(H) + By_{24}(H) = 0 \tag{19}$$

After solving for A and B, we obtain the expressions for vertical and horizontal displacements in the wavenumber-frequency domain by

$$
\begin{aligned}
\bar{u}_z(k,z,\omega) &= Ay_{11}(z) + By_{21}(z) \\
&= \frac{-y_{24}(H)y_{11}(z) + y_{14}(H)y_{21}(z)}{y_{12}(H)y_{24}(H) - y_{14}(H)y_{22}(H)} P(k,\omega)
\end{aligned}
\tag{20}
$$

$$
\begin{aligned}
i\bar{u}_x(k,z,\omega) &= Ay_{13}(z) + By_{23}(z) \\
&= \frac{-y_{24}(H)y_{13}(z) + y_{14}(H)y_{23}(z)}{y_{12}(H)y_{24}(H) - y_{14}(H)y_{22}(H)} P(k,\omega)
\end{aligned}
\tag{21}
$$

Displacement spectra at (x, z) are then obtained by transforming these quantities from the wavenumber domain to the spatial domain (x):

$$U_z(x,z,\omega) = \frac{1}{2\pi}\int_{-\infty}^{\infty} \bar{u}_z(k,\omega)e^{-ikx}\mathrm{d}k$$

$$= \left[\frac{-y_{24}(H)y_{11}(z) + y_{14}(H)y_{21}(z)}{y_{12}(H)y_{24}(H) - y_{14}(H)y_{22}(H)}\right]_{k=\frac{\omega}{c}} \bar{P}(\omega)e^{-i\frac{\omega}{c}x} \tag{22}$$

$$iU_x(x,z,\omega) = \frac{1}{2\pi}\int_{-\infty}^{\infty} i\bar{u}_x(k,\omega)e^{-ikx}\mathrm{d}k$$

$$= \left[\frac{-y_{24}(H)y_{13}(z) + y_{14}(H)y_{23}(z)}{y_{12}(H)y_{24}(H) - y_{14}(H)y_{22}(H)}\right]_{k=\frac{\omega}{c}} \bar{P}(\omega)e^{-i\frac{\omega}{c}x} \tag{23}$$

Here the wavenumber k is now replaced by ω/c because of the delta function in the boundary condition.

2.4.5 Numerical Examples

In this section, we show two numerical examples for vertical displacement using (22). The first example is a comparison of our numerical solution for a homogeneous half-space against the analytical solution. An analytical expression for the vertical displacement at an angular frequency ω can be written by (Sorrells, 1971).

$$U_z(x,z,\omega) = -\frac{c}{2\mu\omega}\left\{\frac{\alpha^2}{\alpha^2 - \beta^2} + \frac{\omega}{c}(H - z)\right\}\bar{P}(\omega)e^{-i\frac{\omega}{c}x + \frac{\omega}{c}(H-z)} \tag{24}$$

where c is pressure wave speed on the surface, μ is the rigidity (shear modulus), α is P wave velocity, and β is S wave velocity. We take the z axis as positive upward, which is opposite to the convention in Sorrells (1971).

Figure 3 shows comparison between $|U_z(x, \omega, z)/\ U_z(x, \omega, H)|$ (analytical solution) and $y_1(x, z, \omega)/\ y_1(x, H, \omega)$ (numerical solution) at 0.02 Hz for two cases, c = 1 (m/s) and c = 5 (m/s). They are normalized by their surface values. We used ρ = 2, 800 (kg/m3), α = 5.8 (km/s), and β = 3.3 (km/s) for these computations. The integration was per- formed by using the fourth-order Runge-Kutta method (e.g., Press et al., 1992). We use this integration scheme for all integrations in this paper. Figure 3 shows that analytical solutions (solid lines) and numerical solutions (dashed lines) match almost perfectly. We also confirm that the depth extent of vertical motion is proportional to pressure wave speed c from this figure.

This match in Figure 3 also means that the (quasi-) static approximation used to derive (24) (Sorrells, 1971) is justified because our numerical results were obtained for a dynamical, finite-frequency case. As it should be clear from the derivations in previous sections, we do not use static approximations for evaluating the response of the medium.

For a more realistic model of shallow structure in which density and elastic parameters change with depth, we used the model BJ97gr760 by Boore (2016). This model was essentially a model for density and S wave velocity. P wave velocity was added by using some empirical relations in Brocher (2005). Figure 4 (top) shows density, P wave velocity, and S wave velocity of this model in the upper 500 m.

Figure 4 (bottom) shows a comparison between vertical displacement for this model and that for a homogeneous half-space model. For density and seismic velocities in a homogeneous model, we used ρ = 1947.8 (kg/m3), α = 1.57108 (km/s), and β = 0.34225 (km/s), which are the surface values in the model BJ97gr760. We normalized both displacements by the surface values in order to focus on how quickly two solutions decrease with depth. Figure 4 (bottom) shows that vertical displacement for the model BJ97gr760 (blue dash) decays more quickly with depth than a homogeneous half-space model (red). This should be related to the high gradient of seismic velocities near the surface in the model BJ97gr760.

2.5 Tilt

It is well known that the tilt-induced contamination of the horizontal components becomes very large in a low-frequency band (Rodgers, 1968). For frequencies about 0.01 Hz, the tilt-induced horizontal displacements are typically 10 – 100 times larger than the horizontal displacements that are directly generated by surface pressure. Clearly, tilt effects must be included in theory.

Figure 5 describes a situation in which the surface is tilted by an angle θ. This tilt (angle θ) is caused by the rotation about the y axis, which is in-and-out of plane of this figure and is given by

$$\theta = \frac{1}{2}\left(\frac{\partial u_x}{\partial z} - \frac{\partial u_z}{\partial x}\right) \tag{25}$$

Note that at the surface, the boundary condition requires $\sigma_{xz} = 0$, which means

$$\frac{\partial u_x}{\partial z} = -\frac{\partial u_z}{\partial \mathrm{x}} \tag{26}$$

Using this formula, we can write the tile angle by

$$\theta = -\frac{\partial u_z}{\partial \mathrm{x}} \tag{27}$$

When this tilt occurs, gravitational acceleration g has nonzero projection on the horizontal component and its magnitude is given by g sin $\theta \approx g\theta$ (Figure 5) where we can assume θ is small. Horizontal displacement (at ω) is now changed by this additional effect and becomes

$$U_H(x, H, \omega) = U_x(x, H, \omega) - \frac{g\theta}{\omega^2} = U_x + \frac{g}{\omega^2}\frac{\partial U_z}{\partial x} = U_x - i\frac{g}{\omega c}U_z \qquad (28)$$

where we used the functional form in (22) for differentiation. Differentiation with respect to x is equivalent to multiplying -iω/c. The term -1/ω^2 in (28) arises because acceleration is converted to displacement in this formula. This spectra UH is the recorded spectra in seismic horizontal component.

For frequencies lower than about 0.05 Hz, the second term in (28) dominates the first term (Sorrells, 1971). We can then approximate the horizontal displacement by

$$U_H = i\frac{g}{\omega c}U_z \qquad (29)$$

For our analysis, we use particle-motion velocity instead of displacement. The relationship between vertical and horizontal velocity PSDs is given by

$$S_H(\omega) = \left(\frac{g}{\omega c}\right)^2 S_z(\omega) \qquad (30)$$

where the horizontal PSD is related to U_H by $S_H = \omega^2|U_H|^2/T$ and the vertical PSD is related to U_Z by $S_Z = \omega^2|U_Z|^2/T$. T is the length of time series used for spectral computation.

Three aspects of equation (30) are noteworthy. First, the ratio of horizontal PSD to vertical PSD is determined by pressure wave speed c at each frequency. This parameter c is important for computation of the depth sensitivity kernels because depth extent of a kernel is proportional to it (Figure 3).

Second, this relationship holds for a vertically heterogeneous medium in general, not just for a homogeneous half-space.

Third, the dominance of tilt makes the depth sensitivity of horizontal data equal to that of vertical data. Equations (30) shows that, except for the coefficient that includes g, c, and ω, horizontal PSDs are proportional to vertical PSDs. Naturally, the depth sensitivity should be the same (proportional) between horizontal and vertical data. Because of this redundancy, we formulate our inversion only for vertical component data.

It may be important to stress that these statements apply only to a low-frequency range below 0.05 Hz. The most important condition is that horizontal data must be dominated by tilt effects. For higher frequencies such as above 0.1 Hz, the directly generated horizontal deformation by pressure waves may become comparable to the tilt related signals; then, these three statements do not apply any more.

2.6 Integration of the Minors

If both seismic and pressure sensors are at the surface ($z = H$), formulas (22) and (23) suggest that there is an alternative approach for computing η(f). This is because if we put $z = H$ in both equations, both numerators and denominators become surface values of the minors for the quantities in (6) – (9). It suggests that η can be computed by integrating the equations for the minors instead of integrating the original equations of motion in (12) (e.g., Gilbert & Backus, 1966, Takeuchi & Saito, 1972, Saito, 1988, Woodhouse, 1988).

The minors for the four quantities in (6) – (9) consist of six variables, formed from two independent solutions of (12). We define them by

$$M_1(z) = y_{11}(z)y_{23}(z) - y_{21}(z)y_{13}(z) \tag{31}$$

$$M_2(z) = y_{12}(z)y_{24}(z) - y_{22}(z)y_{14}(z) \tag{32}$$

$$M_3(z) = y_{11}(z)y_{22}(z) - y_{21}(z)y_{12}(z) \tag{33}$$

$$M_4(z) = y_{11}(z)y_{24}(z) - y_{21}(z)y_{14}(z) \tag{34}$$

$$M_5(z) = y_{13}(z)y_{22}(z) - y_{23}(z)y_{12}(z) \tag{35}$$

$$M_6(z) = y_{13}(z)y_{24}(z) - y_{23}(z)y_{14}(z) \tag{36}$$

where y_{1i} and y_{2i} ($i = 1 - 4$) are two independent solutions. Using (12) and (13), we can derive formulas for dM_j/dz (j = 1−6). It turns out that $M_6(z) = -M_3(z)$ holds, leaving only five independent variables among the minors (Takeuchi & Saito, 1972). Therefore, we define the five-element vector $\mathbf{M} = (M_1, M_2, M_3, M_4, M_5)^T$. The matrix differential equation for **M** can be written by

$$\frac{d\mathbf{M}}{dz} = \mathbf{BM} \tag{37}$$

where B is defined by

$$\mathbf{B} = \begin{pmatrix} 0 & 0 & 0 & \frac{1}{\mu} & -\frac{1}{\lambda + 2\mu} \\ 0 & 0 & 0 & -\rho\omega^2 & \rho\omega^2 - 4k^2\mu\frac{\lambda + \mu}{\lambda + 2\mu} \\ 0 & 0 & 0 & k & \frac{k\lambda}{\lambda + 2\mu} \\ -\rho\omega^2 + 4k^2\mu\frac{\lambda + \mu}{\lambda + 2\mu} & \frac{1}{\lambda + 2\mu} & -\frac{2k\lambda}{\lambda + 2\mu} & 0 & 0 \\ \rho\omega^2 & -\frac{1}{\mu} & -2k & 0 & 0 \end{pmatrix} \tag{38}$$

This system can be integrated, starting with analytic solutions in the lowermost half-space. The starting vector at z = 0 can be obtained from (15) and (17):

$$
\begin{aligned}
M_1(0) &= y_{11}(0)y_{23}(0) - y_{21}(0)y_{13}(0) \\
M_2(0) &= y_{12}(0)y_{24}(0) - y_{22}(0)y_{14}(0) \\
M_3(0) &= y_{11}(0)y_{22}(0) - y_{21}(0)y_{12}(0) \\
M_4(0) &= y_{11}(0)y_{24}(0) - y_{21}(0)y_{14}(0) \\
M_5(0) &= y_{13}(0)y_{22}(0) - y_{23}(0)y_{12}(0)
\end{aligned}
\tag{39}
$$

Integrating up to the surface and obtaining $M_1(H) - M_5(H)$, we can rewrite (22) and (23) by

$$U_z(x,H,\omega) = -\left[\frac{M_4(H)}{M_2(H)}\right]_{k=\frac{\omega}{c}} \bar{P}(\omega)e^{-i\frac{\omega}{c}x} \tag{40}$$

$$iU_x(x,H,\omega) = \left[\frac{M_3(H)}{M_2(H)}\right]_{k=\frac{w}{c}} \bar{P}(\omega)e^{-i\frac{\omega}{c}x} \tag{41}$$

where $M_2(H)$, $M_3(H)$, and $M_4(H)$ are the surface values of the minors. They are vertical and horizontal displacement at the surface.

In the lowermost half-space, we use the radiation boundary condition and five elements in (39) show the values at the top of the lowermost half-space. In Crawford et al. (1998), a similar minor method was used for which they referred to Gomberg and Masters (1988) as their basis of application. Gomberg and Masters (1988) used the locked-mode approach, using the minor method and applied it to a time domain analysis of earthquake data. A time domain analysis with the locked-mode approach can be justified because artificial reflections from the bottom boundary (which is not the radiation boundary condition) can be avoided by choosing a suitable time interval. For an analysis in the frequency domain such as the compliance data analysis, it is hard to avoid this effect because artificial reflection arrives relatively quickly. If we analyze 1-hr time series as we do in section 7, reflected phases even from a depth of 1,000 km (for example) may be included in theoretical results. Crawford et al. (1998) did not provide details on this point.

2.7 Depth Sensitivity Kernels

2.7.1 Computation of $\boldsymbol{\eta}$(f) and Depth Sensitivity Kernels

We can write the quantity η(f) using the minors as

$$\eta = \frac{S_Z}{S_p} = \omega^2 \left[\frac{M_4(H)}{M_2(H)}\right]^2 \tag{42}$$

where the coefficient $\omega 2$ arises because we use velocity PSD for S_z.

Starting with the initial solution in the lowermost half-space (equation (39)), we integrate the matrix equation in (37) up to the surface $z = H$ and obtain $M_2(H)$ and $M_4(H)$. We obtain η(f) from the above equation.

If we perturb density (ρ), P wave velocity (α), or S wave velocity(β), it should lead to a perturbation of η. We can express this relationship by an integral

$$\frac{\delta\eta}{\eta} = \int_{-\infty}^{H} \left(K_\rho \frac{\delta\rho}{\rho} + K_\alpha \frac{\delta\alpha}{\alpha} + K_\beta \frac{\delta\beta}{\beta}\right) \mathrm{d}z \tag{43}$$

where K_ρ, K_α, and K_β are the depth sensitivity kernels for density, P wave velocity, and S wave velocity.

In our current approach, we use numerical differentiation to compute these kernels. We numerically perturb a parameter at a depth and compute $\delta\eta/\eta$ from which we can derive the kernels in (43).

In an alternative parameterization scheme, we can take density, bulk modulus (κ), and rigidity (μ) as three independent parameters. For this case, we can write

$$\frac{\delta\eta}{\eta} = \int_{-\infty}^{H} \left(K_\rho{}' \frac{\delta\rho}{\rho} + K_\kappa \frac{\delta\kappa}{\kappa} + K_\mu \frac{\delta\mu}{\mu} \right) \mathrm{d}z \tag{44}$$

where the density kernel in this equation $K_\rho{}'$ is different from the one K_ρ in (43). It is straightforward to show that the kernels in (43) and (44) are related by

$$K_\rho' = K_\rho - \frac{1}{2}\left(K_\alpha + K_\beta\right) \tag{45}$$

$$K_\kappa = \left(\frac{1}{2} - \frac{2}{3}\frac{\beta^2}{\alpha^2}\right) K_\alpha \tag{46}$$

$$K_\mu = \frac{2}{3}\frac{\beta^2}{\alpha^2} K_\alpha + \frac{1}{2} K_\beta \tag{47}$$

Figure 6 shows numerical examples of the depth sensitivity kernels for the model BJ97gr760. They were computed for c = 1 (m/s) at a frequency of 0.02 Hz. We first computed the kernels by integrating the 4 × 4 matrix system in (12). This requires integration of two independent vectors from the lowermost half-space to the surface and matching the surface boundary conditions. The results are shown by solid lines in Figure 6; the density kernel is green, the P wave velocity kernel is blue, and the S wave velocity kernel is red.

We also computed the kernels for the same model by integrating the equations for the minors in (37) and plotted the results by black dashed lines. This approach integrates a 5 × 5 matrix system, but the integration is needed only once over the depth. Figure 6 shows that the two approaches, not surprisingly, produced the same results.

Our experience is that the integration of the minors using (37) is faster by about 40% than the integration of the original equations in (12). This faster speed of the minor method is useful for the kernel computations in (43), as we need to integrate the equations for each perturbation of parameter from all depths.

2.7.2 Lack of Sensitivity to Density Structure

Figure 7 compares the kernels computed for the model BJ97gr760 using (43) (left) and (44) (right). The left panel shows the kernels when we took density, P wave velocity, and S wave velocity as independent parameters. The right panel shows the kernels when we took density, bulk modulus, and rigidity as parameters. A rather striking result is seen for the density kernel in the right panel, which is basically 0.

We also examined the kernels for five homogeneous structures in which we systematically changed S wave velocity but kept density and P wave velocity constant. Figures 8a–8c show the kernels when density is 2,500 kg/m3 and P wave velocity is 6.0 km/s, while S wave velocity is changed from 1.5 to 3.5 km/s at an interval of 0.5 km/s.

Figure 8a shows the rigidity kernels (K_μ). All five kernels have the maximum absolute amplitudes at about the same depth (about 16 m). Their amplitudes are such that smaller the S wave velocity, larger the maximum (absolute) amplitudes. The maximum amplitude is seen for Vs = 1.5 km/s, and the smallest maximum amplitude is found for Vs = 3.5 km/s. We also note that the width of the peak increases with the maximum amplitude. Therefore, the kernel for Vs = 1.5 km/s has the largest (absolute) amplitude and the broadest peak among the five models.

Figure 8b shows the bulk modulus kernels (K_κ) whose maximum absolute amplitudes occur at the surface. Among the five models, the maximum amplitude occurs for the model with Vs = 3.5 km/s, and the maximum amplitudes decrease for lower S wave velocity models. These amplitudes are in the reverse order of the rigidity kernels in Figure 8a.

Figure 8c shows the density kernels (K_{ρ}') that are very close to 0. They are not exactly 0 as there seems to be small, nonzero amplitude near the surface, especially for high Vs models (Vs = 3.0 and 3.5 km/s). But in comparison to K_μ and K_κ they appear almost negligible. Note that Figures 8a–8c are plotted with the same amplitude scale.

We also examined other structures, but all results showed near-zero density kernels, when we took density, κ, and μ as three independent parameters. We also confirmed similar features when we used the Lame's constant (λ) in place of the bulk modulus (κ). These results indicate that η(f) is primarily a function of two elastic constants and is quite insensitive to density structure. For a homogeneous half-space model, this is an obvious point as the analytical solution (Sorrells, 1971) contains only two elastic constants (Crawford et al., 1998). But the lack of sensitivity to density structure seems to hold for a more generally layered medium. Based on these results, we drop density term in the inversion process.

2.8 Example of Inversion

In this section, we show examples of inversion for two stations. They are KMSC in South Carolina and Y22D in Socorro, New Mexico, and were part of the EarthScope TA.

The data were downloaded from the Data Management Center of the Incorporated Research Institutions for Seismology. For pressure data, we used the infrasound sensor data at both stations. There is an option of using barometer data for pressure instead of infrasound data, but as we discussed in Tanimoto and Wang (2018), two pressure data at TA stations are consistent for the frequency range of our analysis (0.01–0.05 Hz). Use of either instrument leads to essentially the same results. For seismic data, after deconvolving the instrument response, we used ground velocity in our analysis.

In the following we discuss (1) data analysis, (2) construction of a starting model, (3) formulation of the inversion, (4) results of inversion for two stations, and (5) discussion on the results.

2.8.1 Data Analysis

For three-component seismic data and pressure data, we first computed the PSDs for every 1-hr time series from the entire year of 2014. We also compute the coherence between each seismic component and pressure data at the same time.

For each station, we measured two parameters S_z/S_p and S_H/S_p for frequencies between 0.01 and 0.04 Hz at an interval of 0.005 Hz. We excluded data above 0.04 Hz because there is some hint of contamination from the primary microseism. Use of data at 0.045 Hz may have been possible, but we stayed on the safe side as the error bars for these ratios became quite large above 0.04 Hz.

Figure 9a shows a figure for KMSC at 0.03 Hz, which plots the two ratios (S_z/S_p and S_H/S_p) against pressure PSD (S_p). As S_p becomes large, both ratios should approach constant values and those constant values are the estimates for S_z/S_p and S_H/S_p for a given frequency (0.03 Hz in this case).

In order to estimate them, we used the coherence as a guide to select data; we chose the time intervals that had the coherence larger than 0.8. By this, we mean the coherence between vertical component and pressure is larger than 0.8 and also the coherence between one of the horizontal components and pressure is larger than 0.8. We accept a case with low coherence for one of the horizontal components, because if the direction of pressure wave is very close to the azimuth of one of the horizontal components, coherence with the other (perpendicular) component can be quite low (because the other component can be noisy and has low signal-to-noise ratio).

We also added another criterion for the selection of data that the pressure PSD (S_p) should be larger than 10 (Pa^2/Hz). This is important because we should be measuring S_z/S_p and S_H/S_p when the forcing (pressure) is large and the deformation becomes large. These selected points are shown by green dots in Figure 9a. We simply take the arithmetic mean of these points for the estimates of the ratios and also compute the standard deviations from them.

There is naturally a question on how these criteria can influence the estimated ratios. As for the pressure criterion ($S_p > 10$), changing it to $S_p > 50$ or $S_p > 100$ do not change the results very much as the (green) points generally lie on a flat trend (Figure 9a).

As for the coherence cutoff values, we examined other cutoff values. The upper panel of Figure 9b shows the variations of our estimates for S_z/S_p when we changed the cutoff coherence value from 0.7 to 0.9 (at an interval of 0.05). Estimates of S_z/S_p for five frequencies (0.01–0.05 Hz) are shown with the error bars in this panel. In order to reduce clutter from overlapping error bars, we plotted the results in different colors and also by shifting the cutoff values slightly. The results show that the estimated values for S_z/S_p basically do not change from 0.7 to 0.9 (the cutoff coherence value) although the size of error bars seem to shrink slightly from 0.7 to 0.9.

The number of data points for different cutoff values is shown in the bottom panel of Figure 9b. It shows that while the number of data was from a few hundreds to a thousand for the cutoff value of 0.7, the number of data became less than about 100 for the cutoff of 0.9. Naturally, a higher coherence cutoff value reduces the number of data considerably. The lower cutoff value typically leads to more scatter in data (larger error bars), whereas the higher cutoff value could lead to biased estimates because of small number of data. In this paper, we chose the middle ground by choosing the cutoff value of 0.8. We also kept $S_p > 10$ (Pa^2/Hz) throughout our analysis.

Table 1 shows the measurements for KMSC, and Table 2 shows the measurements for Y22D. The second and the third columns in each table are our measurements for S_z/S_p and S_H/S_p. The fourth column shows our estimates for pressure wave speed c(f), based on the relation in (30). We took the ratios of S_z/S_p and S_H/S_p to obtain pressure wave speeds. The fifth column shows our estimates for the modified rigidity $\bar{\mu}$ obtained at each frequency. The modified rigidity is defined by $\overline{\mu} = (\lambda + \mu)/(\lambda + 2\mu) \cdot \mu$ and is the only controlling parameter if the medium were a homogeneous half-space (Sorrells, 1971; Tanimoto & Wang, 2018). From our data, we estimate this parameter from $\overline{\mu} = (c/2)\sqrt{S_p/S_Z}$.

We attempt to solve for a vertically heterogeneous medium and not for a homogeneous half-space, but this parameter gives us some ideas for the layered structure beneath a station. If they were constant throughout the frequency range (0.01 – 0.04 Hz), it indicates that the underlying structure is close to a homogeneous half-space. If not, it gives us some information for a vertically heterogeneous structure because $\bar{\mu}$ at lower frequencies should sense rigidity at deeper depths and represent an averaged rigidity over a wider depth range than $\overline{\mu}$ at higher frequencies. But both KMSC and Y22D showed variations of $\overline{\mu}$ from 0.01 to 0.04 Hz. We used this information for the construction of a starting model.

2.8.2 Construction of a Starting Model

We constructed a starting model for the inversion using the modified rigidity values from observation (Tables 1 and 2) and also using the model BJ97gr760 (Boore, 2016) as a reference. Note that we attempt to find a starting model that can provide a reasonably good fit to the observed η(f). Fit to data does not have to be excellent at this stage as the iterative process will improve it. However, we have had a problem in the convergence of this iterative process when a starting model did not fit the data very well. For example, we initially tried a homogeneous half-space model as a starting model but it failed at many stations.

We have found that the following approach works for most stations. First, we computed the modified rigidity for the model BJ97gr760 and sought for a matching pair of density (ρ), P wave velocity (α), and S wave velocity (β) with our observed modified rigidity. For each frequency in Tables 1 and 2, we conducted this search.

We then determined a depth to assign to each set of ρ, α, and β. For this process, we used a depth of the maximum amplitude in the rigidity kernels as the guide. An example is shown in Figure 8a; Figure 8a shows the results for 0.01 Hz and for pressure wave speed of c = 1 (m/s). The important point in this figure is that the rigidity kernel peaks appear at about 15 m in depth regardless of S wave velocity. Our numerical tests showed that the depth of these maximum peaks did not change much for layered structures. But this peak depth changed with frequency dramatically. In fact, we found that the depth is inversely proportional to the frequency f. Thus, we have an estimate for the peak depth at h = 0.15/f (m). This formula means h = 15 m for 0.01 Hz, h = 5 m for 0.03 Hz, and h = 3 m for 0.05 Hz.

We also needed to consider the influence of pressure wave speed because the depth extent of the kernels is proportional to it. But since c is simply proportional to the depth extent of kernels, it can be included by a simple multiplication of c(f) to the above formula. We can then write h = 0.15c(f)/f where the unit of c(f) is meters per second. This formula gives an approximate depth of the maximum (rigidity) kernel peak. Using this formula, we assigned a depth h to each set of ρ, α, and β that we obtained from each $\overline{\mu}$.

In this study, we had measurements of modified rigidities at seven frequencies from 0.01 to 0.04 Hz at an interval of 0.005 Hz. We assign numbers to h at 0.04 Hz to h at 0.01 Hz by h_1, h_2, … , h_7. The values of hi are in the increasing order. We assign density and seismic velocities to each depth and write them as (h_1, ρ_1, α_1, β_1), (h_2, ρ_2, α_2, β_2), … , (h_7, ρ_7, α_7, β_7).

We construct a starting model by the linear interpolation of these values for depths between h_1 and h_7. For the depth range between the surface and h1, we assumed a homogeneous layer with constant density and seismic velocities with values at h_1 (ρ_1, α_1, β_1). For depths beyond h_7, we assumed a homogeneous half-space with the values (ρ_7, α_7, β_7). We now have a starting model with which we can start the nonlinear inversion.

There are many parts in this algorithm that may be improved in the future. Use of the peak depths of rigidity kernels (for a homogeneous half-space) may appear crude. But for construction of a starting model that fits the observed η(f) reasonably well, this algorithm has worked.

2.8.3 Formulation for the Inversion

In this section we describe the basic mathematical formulation for the inversion procedure. As η(f) is primarily a function of two elastic constants, we drop the density term in the inversion process and solve for the bulk modulus (κ) and the rigidity (μ). We can then write the basic integral relationship as

$$\frac{\delta\eta}{\eta} = \int_{-\infty}^{H} \left(K_\kappa \frac{\delta\kappa}{\kappa} + K_\mu \frac{\delta\mu}{\mu} \right) \mathrm{d}z \tag{48}$$

For a frequency f, the term on the left-hand side can be written by

$$\frac{\delta\eta}{\eta} = \frac{\eta_0(f) - \eta_T(f)}{\eta_T(f)} \tag{49}$$

where $\eta_0(f)$ is the observed η at frequency f and $\eta_T(f)$ is the theoretical η for a given model, which is updated in each iteration step.

For each frequency, we have a separate equation like (48). Let us write the number of frequencies by *m*. For the data in this paper, *m* = 7. By using *i* as an index for the frequencies, we rewrite the above formula by

$$\Delta\eta_i = \frac{\eta_0^i - \eta_T^i}{\eta_T^i} \tag{50}$$

where $\Delta\eta_i$ is a shorthand expression and i = 1, 2, … , *m*.

We discretize the structure by a stack of n homogeneous layers. For convenience, we assign the same thick- ness Δz = 0.5 m to all layers. The integration in (48) becomes a sum of contributions from all layers and can be written

$$\Delta\eta_i = \sum_{j=1}^{n} \left\{ K_\kappa^{ij} \left(\frac{\delta\kappa}{\kappa}\right)_j + K_\mu^{ij} \left(\frac{\delta\mu}{\mu}\right)_j \right\} \Delta z \tag{51}$$

Including all data from *m* frequencies, we can write a matrix equation that needs to be solved at each iteration step by

$$\mathbf{Ax} = \mathbf{d} \tag{\mathbf{52}}$$

where the right-hand side is the data vector defined by

$$\mathbf{d} = [\Delta\eta_1, \Delta\eta_2, \dots, \Delta\eta_m]^T \tag{53}$$

where *T* means the transpose of a matrix (vector).

We define the solution vector **x** by

$$\mathbf{x} = \left[\left(\frac{\delta\kappa}{\kappa}\right)_1, \left(\frac{\delta\kappa}{\kappa}\right)_2, \dots, \left(\frac{\delta\kappa}{\kappa}\right)_n, \left(\frac{\delta\mu}{\mu}\right)_1, \left(\frac{\delta\mu}{\mu}\right)_2, \dots, \left(\frac{\delta\mu}{\mu}\right)_n \right]^T \tag{54}$$

where the subscript is the layer number. Because each layer has two elastic constants to be solved for, we have 2*n* elements in this vector.

The matrix **A** is defined by

$$\mathbf{A} = \begin{pmatrix} K_\kappa^{11} & K_\kappa^{12} & \dots & K_\kappa^{1n} & K_\mu^{11} & K_\mu^{12} & \dots & K_\mu^{1n} \\ K_\kappa^{21} & K_\kappa^{22} & \dots & K_\kappa^{2n} & K_\mu^{21} & K_\mu^{22} & \dots & K_\mu^{2n} \\ \vdots & \vdots & \vdots & \vdots & \vdots & \vdots & \vdots & \vdots \\ K_\kappa^{m1} & K_\kappa^{m2} & \dots & K_\kappa^{mn} & K_\mu^{m1} & K_\mu^{m2} & \dots & K_\mu^{mn} \end{pmatrix} \Delta z \qquad (55)$$

where the size of this matrix is *m* x 2*n*.

We solve the matrix equation (52) by the damped least squares (e.g., Aki & Richards, 2002). With a damping constant ϵ^2, a solution can be written by

$$\mathbf{x} = (\mathbf{A}^\mathbf{T}\mathbf{A} + \mathbf{ff}^2\mathbf{I})^{-1}\mathbf{A}^\mathbf{T}\mathbf{d} \qquad (\mathbf{56})$$

By changing this damping constant, we can get a series of solutions. We chose a damping constant such that the variance reduction in each iteration did not exceed 95%. We then update the structure by this solution and go on to the next iteration step.

2.8.4 Results for Two Stations

Figure 10 shows the results for KMSC; the top panel shows measurements for S_z/S_p from 0.01 to 0.04 Hz at an interval of 0.005 Hz. The mean for each frequency is shown by a black circle, and its standard deviation (1σ) is shown by a vertical bar. The detailed numbers are given in Table 1.

We derived a starting model according to the procedure in the last section and computed theoretical values of η(f) for it. The equations for the minors were integrated to obtain η(f). The results are shown by a blue line in the top panel. In the low-frequency range below 0.02 Hz, the blue line fits the data quite well but its deviation from the mean values (the mismatch) grew for higher frequencies. We proceeded to the iterative process to minimize these misfits.

In every iteration step, we computed the depth sensitivity kernels for the rigidity and the bulk modulus, solved for the perturbations in the rigidity ($\delta\mu/\mu$) and the bulk modulus ($\delta\kappa/\kappa$) as we described in the last section and updated the structure.

Decrease of the misfits is shown in the bottom panel (Figure 10) by the variance for each iteration step. The variance was computed by

$$\sigma^2 = \sum_{j=1}^{m} \left(\eta_o^i - \eta_T^i\right)^2 \qquad (57)$$

Denoting the variance by the starting model σ^2, normalized variance at each iteration step (σ^2/σ_0^2) is plotted in the bottom panel.

The bottom panel shows that the misfits decreased quickly although we continued the iteration steps up to the tenth iteration. We regard the structure at the 3rd iteration as the final model for KMSC as further iterations steps did not improve the fit very much. The middle panels show how the rigidity structure (left) and the bulk modulus structure (right) changed over these iteration steps. In order to avoid clutter, only the starting structure (blue), the first iteration model (green) and the third (final) iteration model (red) are shown.

We applied the same analysis to data for Y22D. Figure 11 (top) shows the fits to data by the starting model (blue), the first iteration model (green), and the second iteration model (red). Although we performed further iterations, the variance decreased quickly (Figure 11, bottom) and was already low by the second iteration. We regard the second iteration as the final step (red circle in the bottom panel) and the resulting model as the final model for Y22D. The rigidity and the bulk modulus structures through the iteration steps are shown in the middle panels.

All results of the inversion including the intermediate steps can be obtained from the data file (Tanimoto, 2018).

2.9 Discussion

2.9.1 Inversion Results and Vs30

The main purpose of presenting examples of inversion at two stations, KMSC and Y22D, was to demonstrate that the proposed algorithm works for retrieving shallow elasticity structure underneath colocated seismic and pressure instruments.

Changes in the bulk modulus structure over the course of inversion were quite small for both stations; in fact, the bulk modulus structure for Y22D basically did not change from the starting model (Figure 11, middle right). This can be understood from the depth sensitivity kernels in Figure 12. The left panels show the case for KMSC, the upper panel showing the rigidity kernels, and the lower panel the bulk modulus kernels. Similar plots for Y22D are shown on the right. Depth sensitivity kernels for all frequencies are shown in Figure 12. The effects from pressure wave speeds were incorporated in these kernels. Strictly speaking, they are the kernels for the first iteration but those sensitivity kernels did not change very much throughout the iteration steps.

The reason for the extremely small effects from the bulk modulus structure at Y22D is obvious as in com- parison to the rigidity kernels (Figure 12, top left), the bulk modulus kernels have very small amplitudes (Figure 12, bottom left). The reason we cannot see any change in the bulk modulus structures for Y22D through the iteration steps (Figure 11, middle right) is due to these small kernels. In the case of KMSC, the bulk modulus kernels are larger in comparison, especially in the upper 5–10 m (Figure 12, bottom right). This seems to be why we see a small change in the bulk modulus structure for KMSC (Figure 10, middle right). But in general, the inversion process constrains the rigidity structure primarily.

One of the applications of our approach is to compare our results against Vs30 data (Allen & Wald, 2007). Figure 13 shows the models for KMSC and Y22D in terms of density, P wave velocity, and S wave velocity. Dashed lines are the starting models, and the solid lines are the final models. Since density does not change through iteration steps in our algorithm, density structures are shown for reference only. We computed Vs30 values for the final models. The average S wave velocity for KMSC is 257 m/s, and that for Y22D is 331 m/s. U.S. Geological Survey (USGS) Vs30 values for these stations were 421 m/s for KMSC and 380 m/s for Y22D. We obtained these USGS values by interpolating the Vs30 grid values. Since the large-scale map of Vs30 is based not only on the local measurements but on the use of topographic gradients (Allen & Wald, 2007, 2009), some discrepancy should be expected. But in general two Vs30 values at both stations appear to be close despite our completely different approach with different data sets.

2.9.2 Comparison to the Compliance Approach in the Ocean Bottom Seismology

Our approach is similar to the compliance approach in the ocean bottom seismology (Crawford et al., 1991, 1998). However, in principle, seismic noise at the surface of the solid Earth can be quite different from seismic noise on the seafloor. The main differences seem to arise in excitation sources; in our problem, the sources are atmospheric winds (the main stream flow) and turbulence associated with them. For seafloor seismic noise, the sources are the oceanic infragravity waves and the ocean currents that create ground tilt on the seafloor (e.g., Crawford & Webb, 2000).

When the main stream flow (winds) is dominant in our atmospheric problem and the oceanic infragravity waves are the primary source of the seafloor seismic noise, the two approaches become quite similar. However, there is an important difference in pressure wave speeds for the two problems. For our problem, pressure wave speeds are typically in the range 1 – 10 m/s (e.g., Tables 1 and 2). For the seafloor compliance analysis, the source of excitation is the speed of the infragravity waves whose dispersion relation is given by

$$\omega^2 = gk \tanh(kH) \tag{58}$$

where H is the ocean depth and ω and k are the angular frequency and wavenumber of infragravity waves. Figure 14 shows the phase speed ($c = \omega/k$) of the infragravity waves, derived from this dispersion formula, and plotted against frequency. Since phase speeds also vary with an ocean depth H, four difference cases of ocean depths are shown (H =100, 500, 1,000, and 2,000 m).

For the frequency range of our analysis (0.01 – 0.05 Hz), Figure 14 shows that phase speeds of the oceanic infragravity waves are approximately between 30 and 120 m/s. This is about 10 – 100 times larger than the speed of our atmospheric pressure sources (Tables 1 and 2). Since the depth sensitivity of compliance data is proportional to this speed, it means that ocean bottom compliance data are sensitive to much deeper depth, approximately 10 – 100 times deeper. In general, we can say that ocean bottom compliance data are sensitive to the upper 1 – 10 km of the crust, while our data are sensitive only to the upper 50 – 100 m from the Earth's surface.

2.9.3 Justification of the Plane Wave Source Model

It is well known that lateral coherence distance of atmospheric pressure is small (e.g., McDonald et al., 1971), typically less than 50 m. Unless special conditions arise, such as strong, sustained winds in a uniform direction, coherence between two pressure sensors at a distance about 100 m is usually close to 0. On the other hand, our pressure wave speed estimates in Table 1, for example, is about c = 2 m/s. At 0.01 Hz, this means the wavelength is 200 m. Why is it then that the pressure coherence at a distance about 100 m is almost 0?

We believe that destruction of coherence at short distances (< 100 m) occurs from the effects of atmospheric turbulence. This is because turbulence can create many eddies with varying length scales because of the energy cascading process of atmospheric turbulence (e.g., Davidson, 2015; Landau & Lifshitz, 1987; Thorne & Blandford, 2017). These eddies can act as multiple pressure sources on the surface. The frequency range of our analysis, 0.01–0.05 Hz, is in such an inertial range of turbulence. In such a situation, even if a wavelength may be 200 m, pressure coherence can be destroyed within a short distance by contributions from different sources.

But then how can we justify our relatively simple plane wave source model? We believe that it may be justified when a main stream flow (wind) is strong and associated turbulence effects are relatively small in comparison. Similar conditions happen in wind-tunnel experiments (e.g., Frisch, 1995), for example. This point was already discussed by Sorrells and Goforth (1973) who stated that a plane wave source model in Sorrells (1971) is a gross oversimplification but may be justified if the turbulent velocity fluctuations are small compared to the main stream velocity. Then they went on to analyze a model that possessed the observed statistical properties of the wind-generated pressure field and concluded that its transfer functions are experimentally indistinguishable from those associated with a plane wave pressure field.

This conclusion by Sorrells and Goforth (1973) might suggest that a stream flow is not necessary and the random pressure field is all that is necessary. But we can show from wind data that when there is high coherence between pressure and seismic data, relatively strong winds actually exist. Figure 15 is a figure of the wind speed PSD plotted against the pressure PSD at two stations, KMSC and Y22D. Both PSDs are at 0.02 Hz and were computed for every 1-hr time interval in 2014.

There is much scatter in Figure 15, but the overall correlation between wind speed (vertical axis) and pressure (horizontal axis) can be clearly identified. Time intervals of high coherence (> 0.7) between pressure and vertical seismic data are plotted in red and show that they are generally in high wind time intervals.

For measurements of $\eta(f)$, we typically choose a high pressure range $S_p > 10$ (Pa^2/Hz), which corresponds to a range for wind data approximately $1 \leq S_w \leq 50$ (m^2/s^2/Hz) in Figure 15. This range of S_w is equivalent to wind speed between about 1 and 7 (m/s). For time intervals with wind speed less than 1 (m/s), coherence between colocated pressure and seismic sensors are clearly low in Figure 15. This low coherence probably means that seismic signals are generated but they are comparable or smaller than seismic signals generated by other sources such as the ocean-generated seismic noise. Clearly, the response of solid Earth by surface pressure changes is very difficult to measure in such cases.

For our goal of retrieving shallow structure, we select high-pressure and high-coherence time intervals for the analysis because seismic deformation is large during those times and the signal-to-noise ratio is generally high. Figure 15 indicates that they correspond to relatively high wind speed time intervals. We speculate that there are relatively strong stream flows during those times and our approach of modeling by a moving pressure source (which can be decomposed into plane waves) may be justified for these selected data.

2.10 Summary

We developed a scheme to invert the colocated seismic and pressure data for depth variation of elasticity. This method is based on measurements of frequency-dependent surface observables $\eta(\mathrm{f})$, which are defined by the ratios between vertical seismic PSD (S_z) to pressure PSD (S_p). We invert this quantity $\eta(\mathrm{f})$ for shallow elasticity structure in the upper 50–100 m just like we invert phase velocity of surface waves for the crust and upper mantle structure.

We showed that theoretical values for $\eta(\mathrm{f})$ can be computed for a layered seismic model by integrating the minors for the P-SV-type equations of motion. This approach can speed up the analysis by about 40% in comparison to the scheme that integrates the original P-SV-type equations of motion.

Using numerical differentiations, we developed an approach to compute the depth sensitivity kernels for $\eta(\mathrm{f})$. One of the most important features in these kernels is that if we took density, the bulk modulus and the rigidity as independent parameters, the density kernels become almost 0. The quantity $\eta(\mathrm{f})$ is basically independent of density structure and is a function of two elastic constants beneath a station. This feature gives us justification to drop density from the inversion process. Lack of dependence on density structure was clear in the analytical solutions for a homogeneous half-space (Sorrells, 1971), but this feature is also true in vertically heterogeneous structures.

We applied our inversion scheme to data at two stations, KMSC and Y22D, from the EarthScope TA. In both cases, the nonlinear, iterative least squares inversion converged quickly. Comparison of our Vs30 values, average S wave velocity in the top 30 m, are in good agreement with USGS Vs30 values at these stations.

2.11 Reference

Aki, K., & Richards, P. G. (2002). *Quantitative seismology: Theory and methods* (2nd ed.). Sausalito: University Science Books.

Allen, T., & Wald, D. J. (2007). Topographic slope as a proxy for global seismic site condition (Vs30) and amplification around the globe (*Open-File Rept.*): U.S. Geol. Survey. 2007-1357, 69.

Allen, T. I., & Wald, D. J. (2009). On the use of high-resolution topographic data as a proxy for seismic site condition (Vs30). *Bulletin of the Seismological Society of America, 99*(2A), 935–943. https://doi.org/10.1785/0120080255

Boore, D. (2016). Determining generic velocity and density models for crustal amplification calculations, with an update of the Boore and Joyner (1997) generic site amplification for Vs(z)=760 m/s. *Bulletin of the Seismological Society of America*, *106*, 316–320.

Brocher, T. (2005). Empirical relations between elastic wavespeeds and density in the Earth's crust. *Bulletin of the Seismological Society of America*, *95*, 2081–2092.

Chapman, C. H. (2004). *Fundamentals of seismic wave propagation*. Cambridge, UK: Cambridge University Press.

Crawford, W. C., & Webb, S. C. (2000). Identifying and removing tilt noise from low-frequency (<0.1Hz) seafloor vertical seismic data. *Bulletin of the Seismological Society of America*, *90*(4), 952–963. https://doi.org/10.1785/0119990121

Crawford, W. C., Webb, S. C., & Hildebrand, J. A. (1991). Seafloor compliance observed by long-period pressure and displacement measurements. *Journal of Geophysical Research*, *96*(B10), 16,151–16,160.

Crawford, W. C., Webb, S. C., & Hildebrand, J. A. (1998). Estimating shear velocities in the oceanic crust from compliance measurements by two-dimensional finite difference modeling. *Journal of Geophysical Research*, *103*(B5), 9895–9916.

Davidson, P. A. (2015). *Turbulence an introduction for scientists and engineers* (2nd ed.). Oxford, UK: Oxford University Press.

De Angelis, S., & Bodin, P. (2012). Watching the wind: Seismic data contamination at long periods due to atmospheric pressure-field-induced tilting. *Bulletin of the Seismological Society of America*, *102*(3), 1255–1265. https://doi.org/10.1785/012110186

Frisch, U. (1995). *Turbulence*. Cambridge, UK: Cambridge University Press.

Gilbert, F., & Backus, G. (1966). Propagation matrices in elastic wave and vibration problems. *Geophysics*, *31*, 326–332.

Gomberg, J. S., & Masters, T. G. (1988). Waveform modelling using locked-mode synthetic and differential seismograms: Application to determination of the structure of Mexico. *Geophysical Journal International*, *94*, 193–218.

Herrin, T. J., Tolstoy, I., & Kraft, D. W. (1969). Atmospheric pressure background fluctuations in the mesoscale range. *Journal of Geophysical Research*, *74*(6), 1321–1329. https://doi.org/10.1029/JB074i006p01321

Hutt, C. R., Ringer, A., & Gee, L. S. (2017). Broadband seismic noise attenuation versus depth at the Albuquerque Seismological Laboratory. *Bulletin of the Seismological Society of America*, *107*(3), 1402–1412. https://doi.org/10.1785/0120160187

Kenda, B., Lognonne, P., Spiga, A., Kawamura, T., Kedar, S., Banerdt, W. B., et al. (2017). Modeling of ground deformation and shallow surface waves generated by Martian dust devils and perspectives for near-surface structure inversion. *Space Science Reviews*, *211*, 501–524. https://doi.org/10.1007/s11214-017-0378-0

Kennett, B. (1983). *Seismic wave propagation in a stratified medium*. Cambridge, UK: Cambridge University Press.

Landau, L. D., & Lifshitz, E. M. (1987). *Fluid mechanics* (2nd ed.)., Course of Theoretical Physics, vol. 6. New York, USA: Pergamon Press. McDonald, J. A., Douze, E. J., & Herrin, E. (1971). The structure of atmospheric turbulence and its application to the design of pipe arrays. *Geophysical Journal of the Royal Astronomical Society*, *26*, 99–109.

Press, W. H., Teukilsky, S. A., Vetterling, W., & Flannery, B. (1992). *Numerical recipes in Fortran the art of scientific computing* (2nd ed.). Cambridge UK: Cambridge University Press.

Rodgers, P. (1968). The response of the horizontal pendulum seismometer to Rayleigh and Love waves, tilt, and free oscillations of the Earth. *Bulletin of the Seismological Society of America*, *58*, 1385–1406.

Saito, M. (1988). Disper80: A subroutine package for the calculation of seismic normal-mode solutions. In D. J. Doornbos (Ed.), *Seismological algorithms: Computational methods and computer programs*. London: Academic Press Inc.

Savino, J., McKamy, K., & Hade, G. (1972). Structures in earth noise beyond twenty seconds—A window for earthquakes. *Bulletin of the Seismological Society of America*, *62*, 141–176.

Sorrells, G. (1971). A preliminary investigation into the relationship between long-period seismic noise and local fluctuations in the atmospheric pressure field. *Geophysical Journal of the Royal Astronomical Society*, *26*, 71–82.

Sorrells, G., & Goforth, T. (1973). Low-frequency earth motion generated by slowly propagating partially organized pressure fields. *Bulletin of the Seismological Society of America*, *63*, 1583–1601.

Sorrells, G., MacDonald, J. A., Der, Z., & Herrin, E. (1971). Earth motion caused by local atmospheric pressure changes. *Geophysical Journal of the Royal Astronomical Society*, *26*, 83–98.

Takeuchi, H., & Saito, M. (1972). Seismic surface waves. In B. A. Bolt (Ed.), *Methods in computational physics* (Vol. 11). New York: Academic Press Inc.

Tanimoto, T. (2018). Inversion data files for Tanimoto and Wang 2018. https://doi.org/10.5281/zenodo.1757099

Tanimoto, T., & Wang, J. (2018). Low-frequency seismic noise characteristics from the analysis of co-located seismic and pressure data. *Journal of Geophysical Research: Solid Earth*, *123*, 5853–5885. https://doi.org/10.1029/2018JB015519

Thorne, K. S., & Blandford, R. D. (2017). *Modern classical physics*. New Jersey, USA: Princeton University Press Princeton.

Tytell, J., Vernon, F., Hedlin, M., de Groot Hedlin, C., Reyes, J., Busby, B., et al. (2016). The USArray transportable array as a platform for weather observation and research. *Bulletin of the Seismological Society of America*, *97*, 603–619. https://doi.org/10.1175/ BAMS-D-14-00204.1

Wolin, E., van der Lee, S., Bollman, T. A., Wiens, D. A., Revenaugh, J., & Darbyshire, F. A. (2015). Seasonal and diurnal variations in long-period noise at SPREE stations: The influence of soil characteristics on shallow stations performance. *Bulletin of the Seismological Society of America*, *105*(5), 2433–2452. https://doi.org/10.1785/0120150046

Woodhouse, J. H. (1988). The calculation of eigenfrequencies and eigenfunctions of the free oscillations of the Earth and the Sun. In D. J. Doornbos (Ed.), *Seismological algorithms: Computational methods and computer programs*. London: Academic Press Inc.

2.12 Figures and Tables

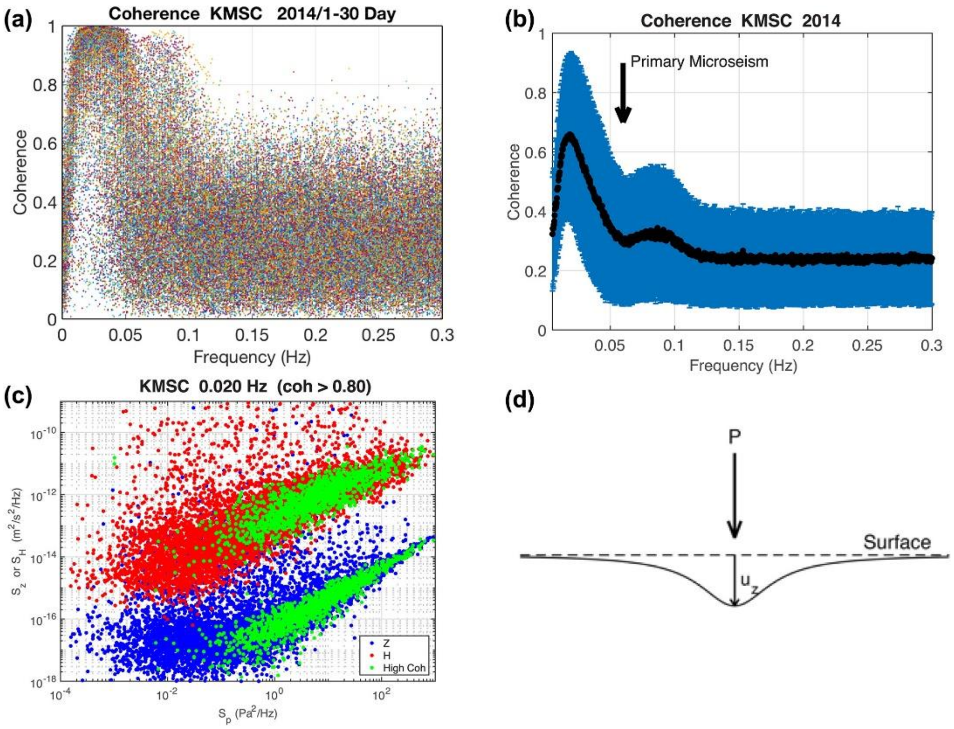

Figure 1. (a) Raw coherence values at station KMSC in South Carolina between vertical seismic data and pressure data from the first 30 days in 2014. Each point represents coherence from 1-hr time interval. High coherence is found for frequencies between 0.01 and 0.05 Hz for which we develop our approach. (b) Average coherence over a year (2014) for station KMSC. The means are shown by a thick black line, and one standard deviation is indicated by the blue area. The arrow is placed at 0.06 Hz, an approximate frequency of the primary microseism. (c) Seismic power spectral densities (PSDs) versus pressure PSD plot. Blue points are vertical PSDs (S_Z), and red points are horizontal PSDs. Horizontal PSDs are the sum of two horizontal PSDs. Green points indicates high - coherence time intervals with coherence higher than 0.8. More details are discussed in the main text. (d) Between 0.01 and 0.05 Hz, ground displacements are literally in sync with pressure variations.

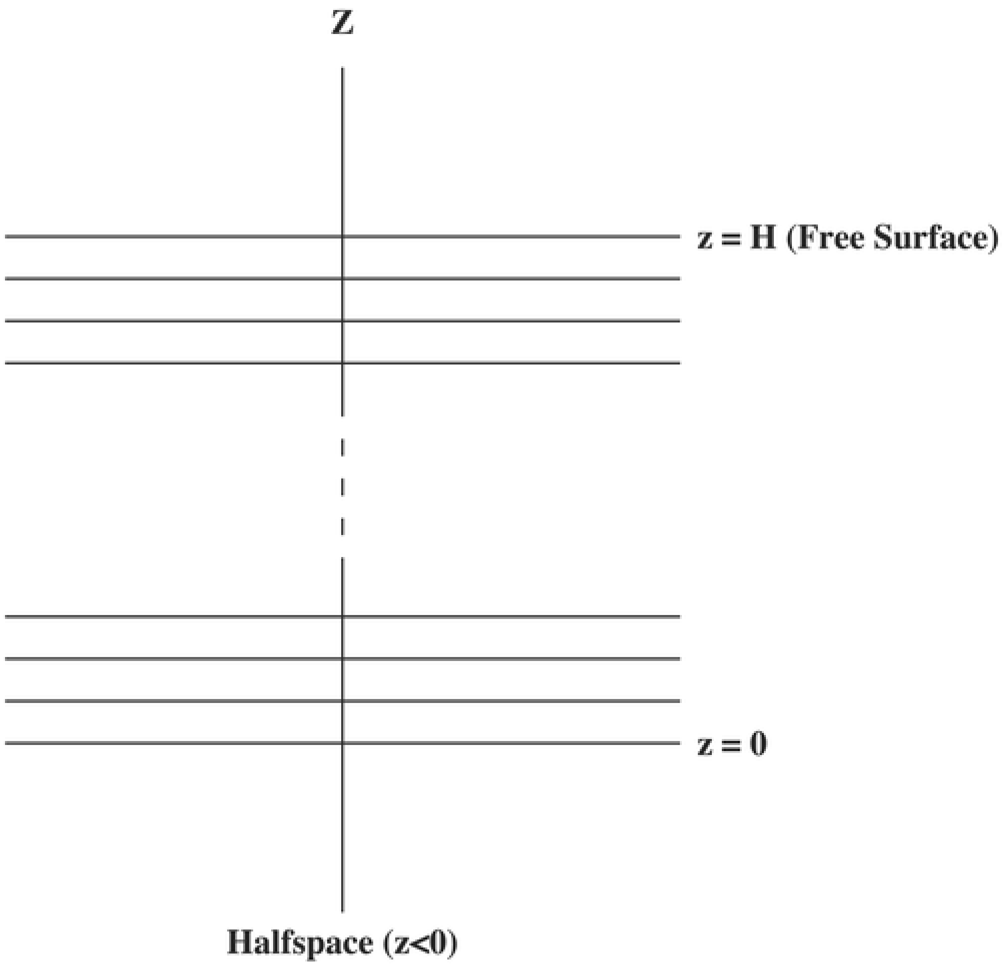

Figure 2. The lowermost half-space is assumed to be homogeneous. Density, P wave velocity, and S wave velocity change with z continuously between z=0 (the top of the lowermost half-space) and z=H (the Earth's surface).

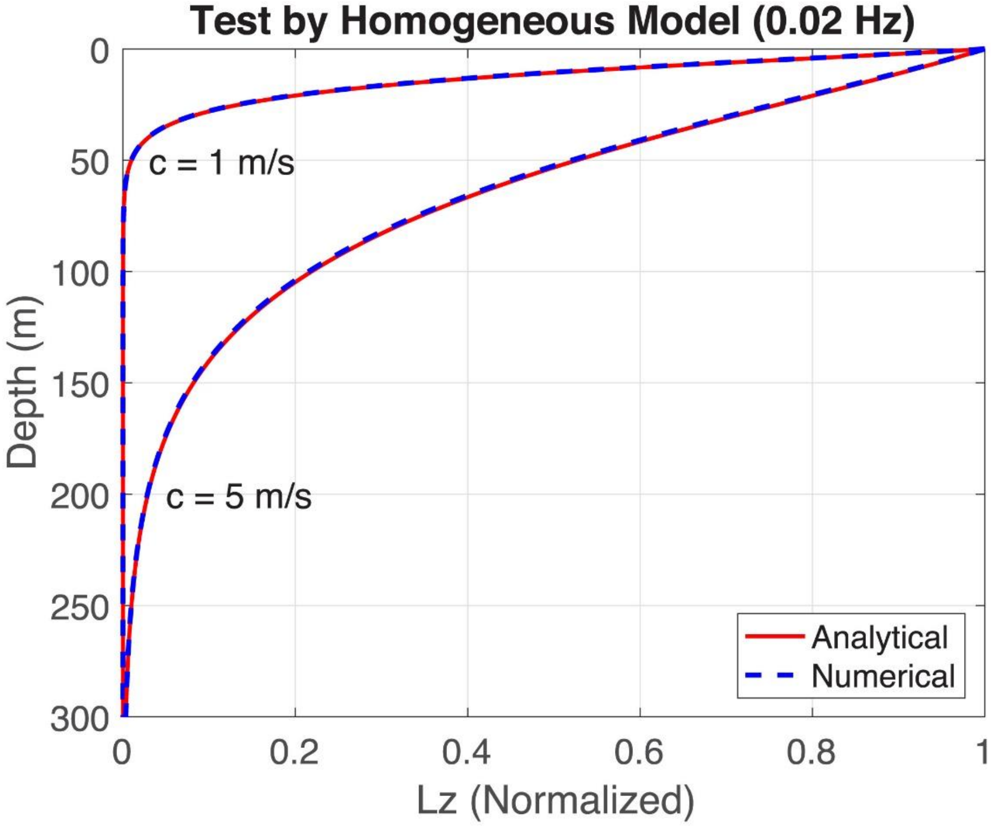

Figure 3. Comparison between analytical solutions (red) and numerical solutions (dash) for vertical displacements in a homogeneous elastic half-space. Two cases (pressure wave speed c=1 m/s and c=5 m/s) are shown. Analytical solutions use the static approximation for the response of the medium, while numerical solutions integrate the dynamic P-SV system equations. Excellent match between them indicates that the quasi - static approximation by Sorrells (1971) is justified.

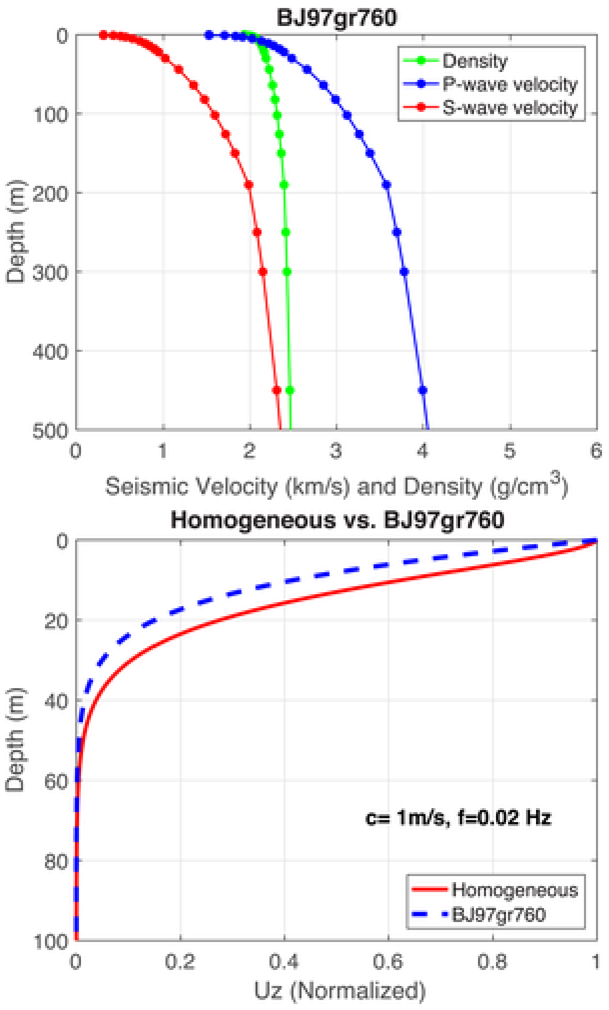

Figure 4. (top) An example of a vertically heterogeneous model BJ97gr760 (Boore, 2016). Density, P wave velocity, and S wave velocity in the upper 500 m are shown. (bottom) Comparison of vertical displacements between a homogeneous half‐space model (red) and BJ97gr760. Both are normalized by surface values. Vertical displacements for the model BJ97gr760 are confined to a depth range closer to the surface.

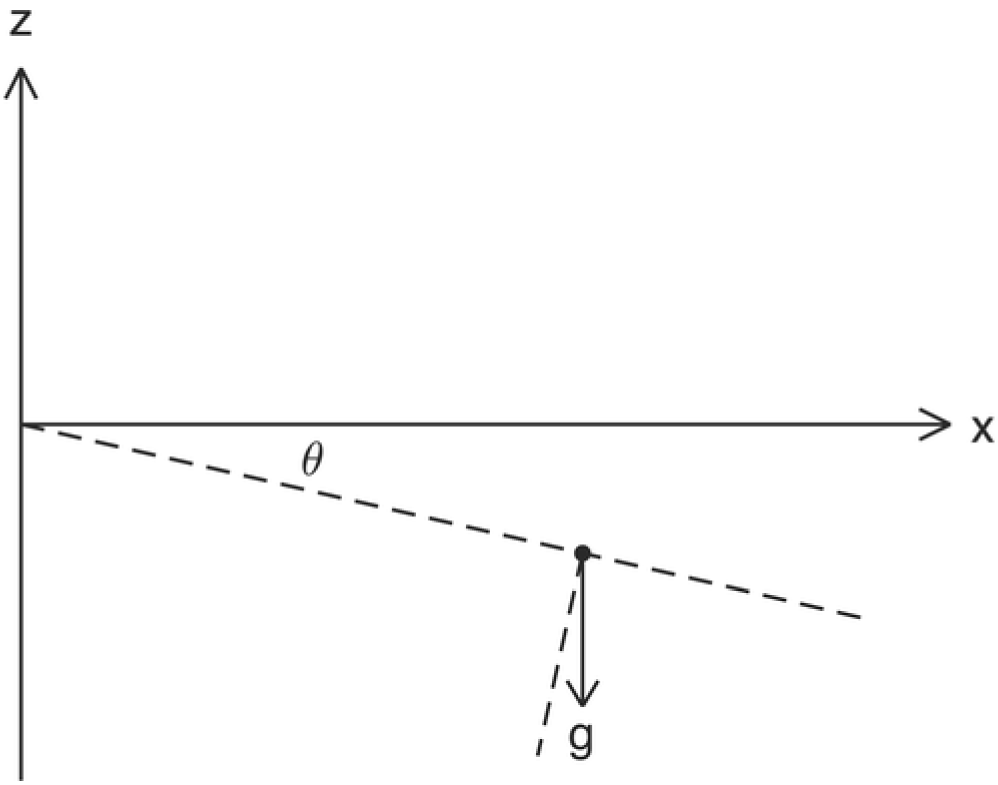

Figure 5. Tilt and projection of gravitational acceleration on the horizontal component (the x axis). In our convention, θ is positive in the clockwise direction from the x axis and the projection of g is in the positive direction of x (*g*sin θ).

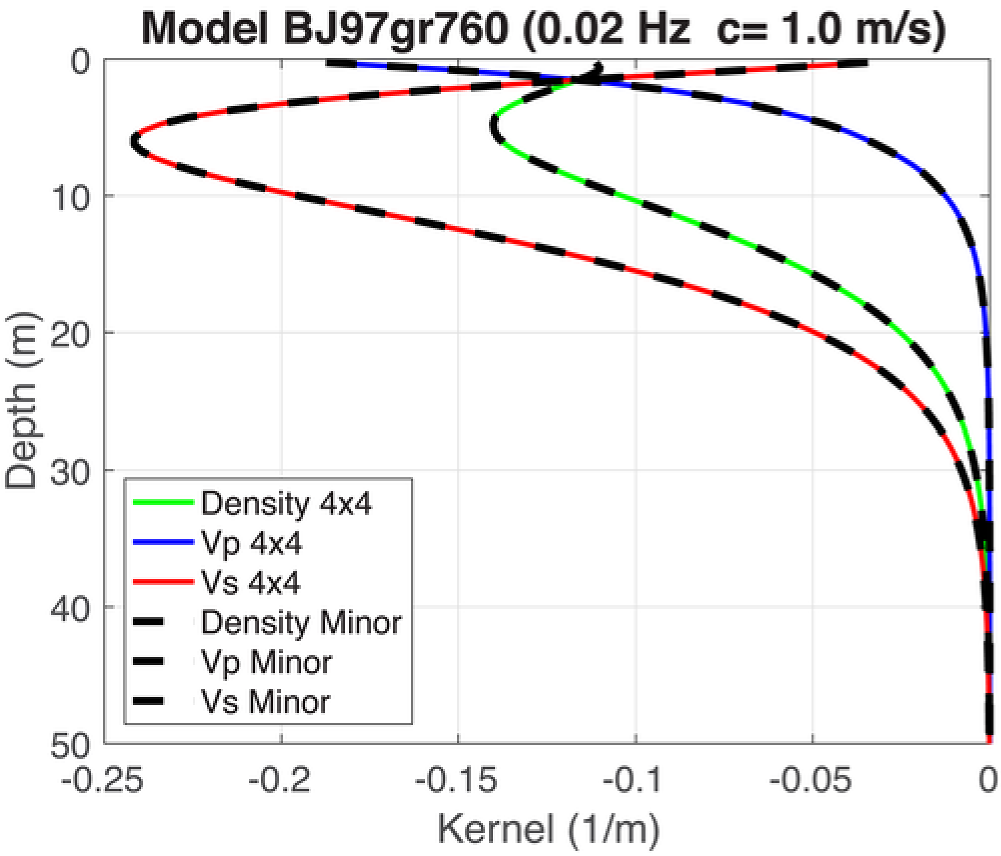

Figure 6. Depth sensitivity kernels for density (green), P wave velocity (blue), and S wave velocity (red) for BJ97gr760. The integration of the 4 × 4 Rayleigh wave system (equation 12) yielded the solid lines with colors. The integration of the minors (equation 37) yielded the dashed lines. The results agree quite well. The integration of the minors is faster in terms of computation time by about 40%

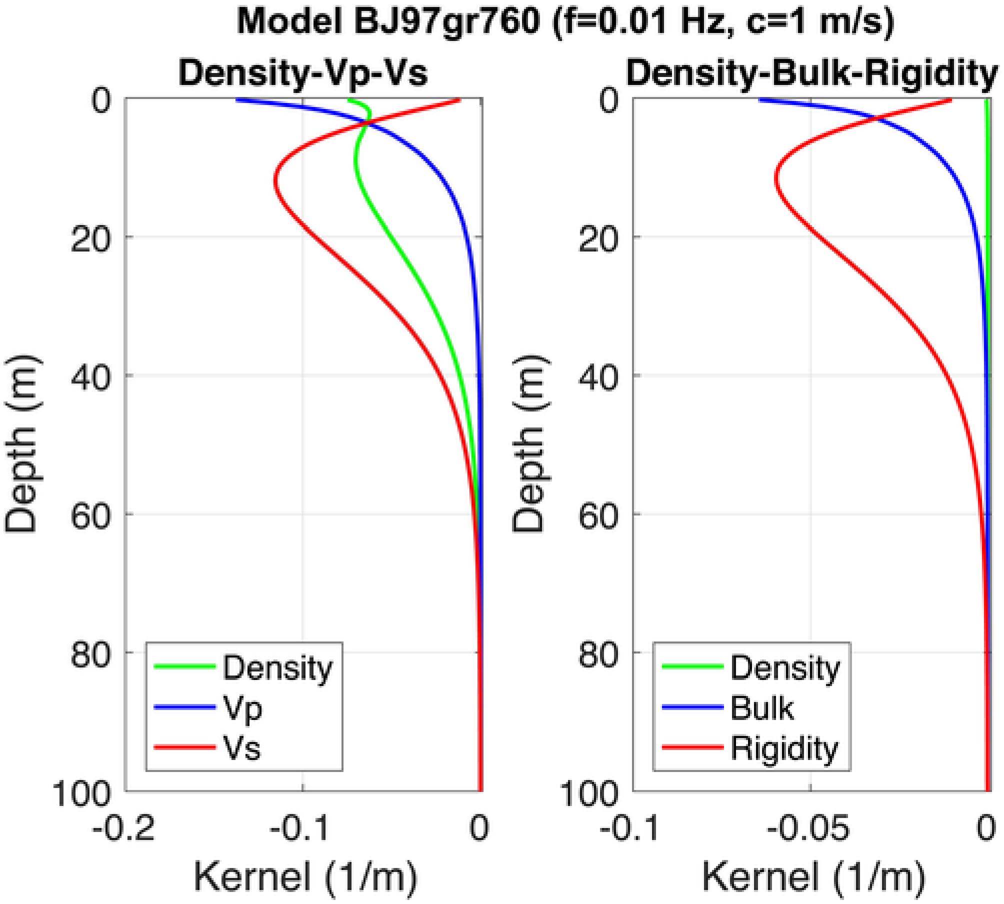

Figure 7. Kernels for BJ97gr760. The left panel shows the kernels for density (K_ρ), P wave velocity (K_α), and S wave velocity (K_β), and the right panel shows the kernels for density (K_ρ’), bulk modulus (K_κ), and rigidity (K_μ). In the latter scheme (right), the density kernel (K_ρ’) disappears almost entirely.

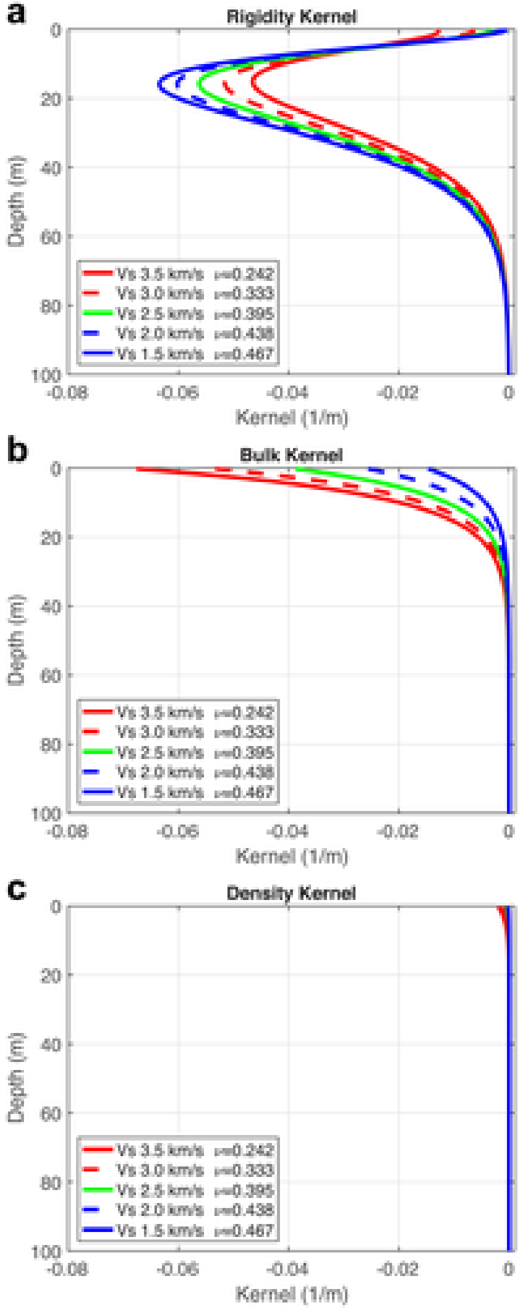

Figure 8. (a) The rigidity kernels (K_μ) for five homogeneous models. P wave velocity and density were fixed at 6 (km/s) and 2,500 (kg/m^3) for all models, while S wave velocities were changed from 1.5 to 3.5 km/s at an interval of 0.5 km/s. All rigidity kernels peak at a depth about 15 m. Lower the S wave velocity, higher the maximum (absolute) amplitude of the kernel. The maximum amplitude is found for Vs = 1.5 km/s. (b) The bulk modulus kernels (K_κ) for the same five models. All kernels reach the maximum at the surface. In contrast to the rigidity kernels, the higher the S wave velocity, the higher the maximum amplitude at the surface. (c) Density kernels are nearly 0 for all five models.

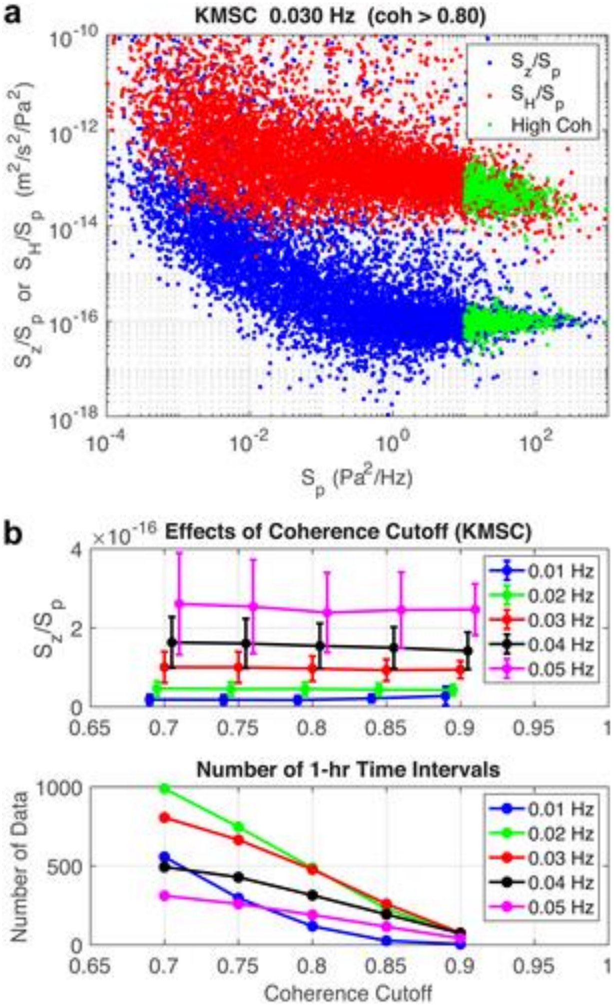

Figure 9. (a) Blue points are the ratios of vertical power spectral density (PSD) to pressure PSD (S_z/S_p) plotted against pressure PSD (S_p). Red points are the ratios of horizontal PSD to pressure PSD (S_H/S_p) plotted against S_p. This is an example for KMSC at 0.03 Hz. In the high pressure range, both ratios should approach constant values. Green points are for the time intervals that had high coherence (>0.8) and high pressure S_p>10 (Pa^2/Hz). Green points were used to estimate the ratios and their error estimates. (b) The top panel shows variations of our estimates for the ratios when we change the coherence cutoff value from 0.7 to 0.9 at an interval of 0.05. The estimates of the ratios were not affected very much for the choice of coherence cutoffs. We used points with coherence higher than 0.8 for our analysis. The bottom panel shows the number of data for different cutoff values of coherence. Naturally, the number of data decreases for higher coherence cutoff.

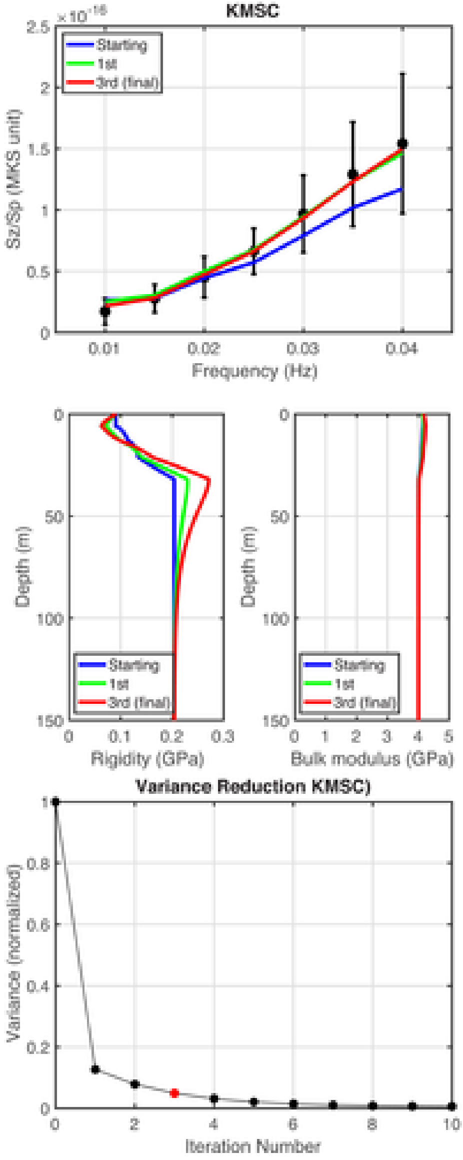

Figure 10. Inversion for shallow structure at KMSC. The top panel shows the fit to η(f) by the starting model (blue line), the fit by the first iteration model (green line), and the fit by the third iteration model (red line). We regard the third model as the final model. The fit to data does not improve dramatically after the first iteration. The middle panels show the rigidity model (left) and the bulk modulus model (right) plotted against depth from the surface to a depth 150 m. The bottom panel shows the reduction of the total variance at each iteration step. The red circle indicates our choice of the final model (the third iteration model).

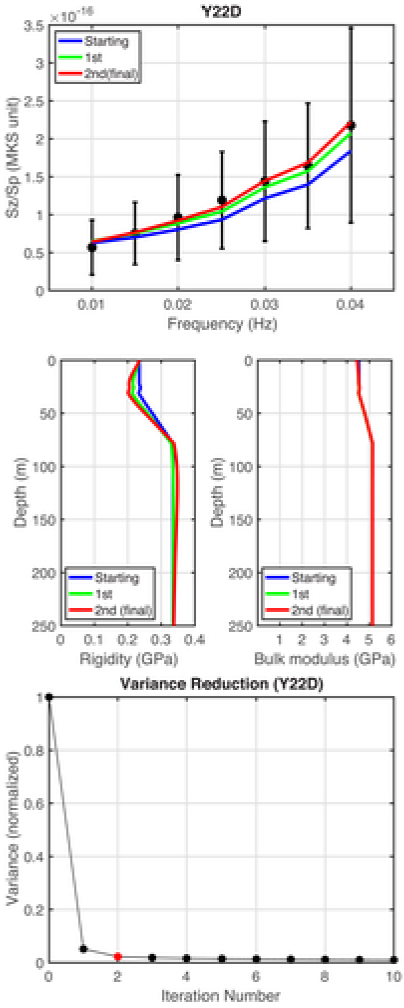

Figure 11. Inversion for structure at Y22D. The top panel shows the fit to η(f) by the starting model (blue line), the fit by the first iteration model (green line), and the fit by the second iteration model (red line), which we regard as the final model. The middle panels show the rigidity model (left) and the bulk modulus model (right) plotted against depth from the surface to a depth 250 m. The bottom panel shows the reduction of the total variance for each iteration. The red circle indicates the final model (the second iteration model).

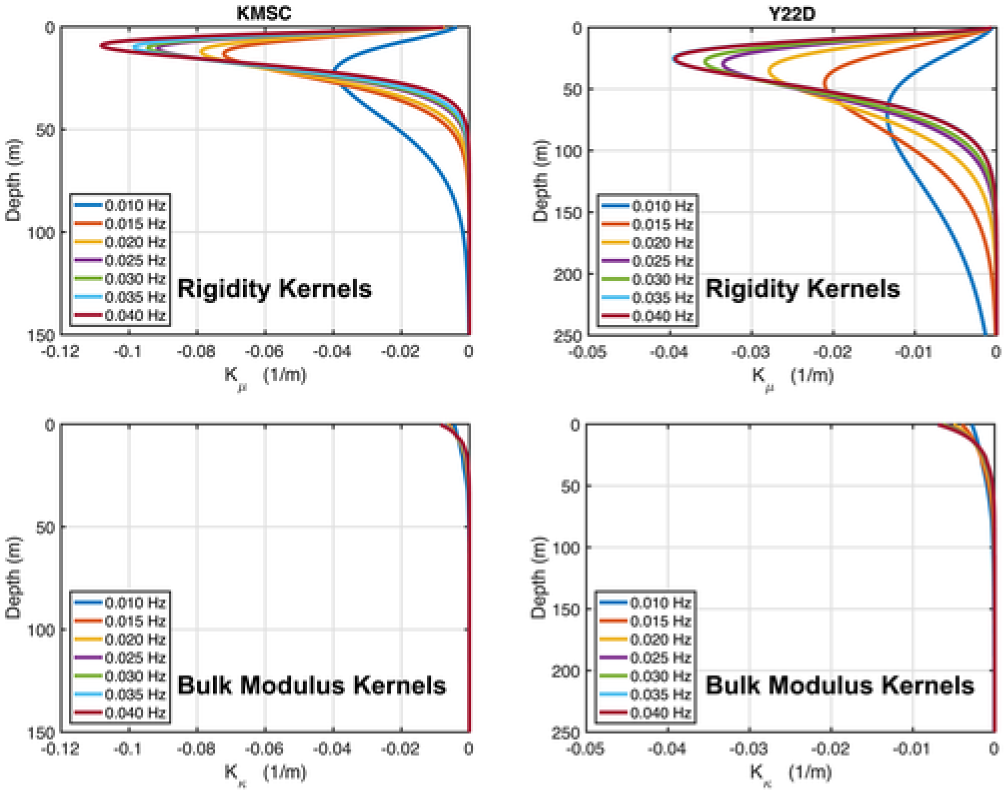

Figure 12. The depth sensitivity kernels for rigidity at each frequency are shown in the top panels, and the kernels for bulk modulus are shown in the bottom panels. The kernels for KMSC are shown on the left and those for Y22D are shown on the right. These kernels are for the starting model, but the basic characteristics of these kernels do not change very much from iteration to iteration. At both stations, the bulk modulus kernels are much smaller than the rigidity kernels. It suggests that rigidity structures are primarily constrained by the inversions (at least for selected two stations).

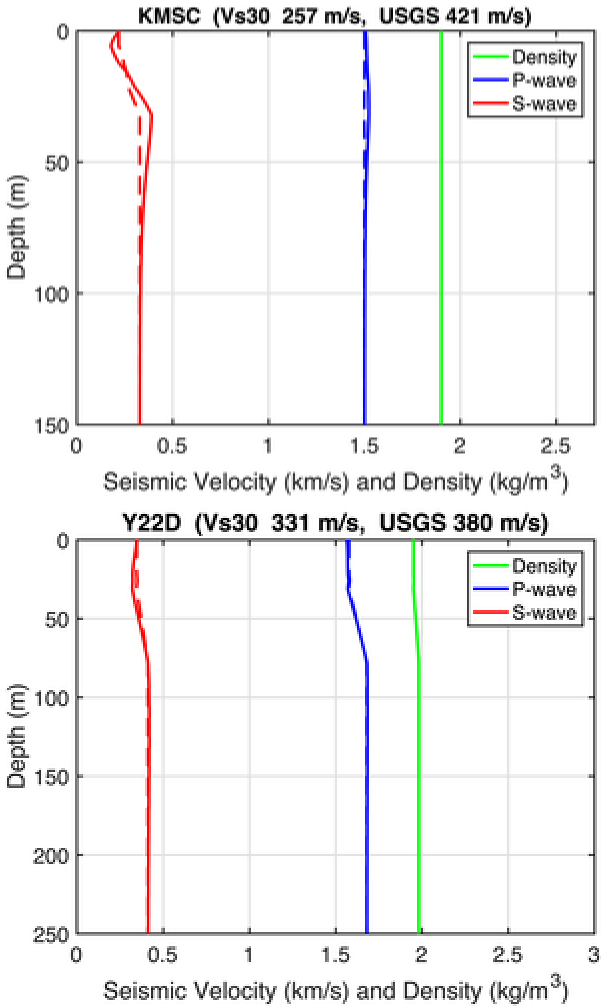

Figure 13. The structure results were converted to density (green), P wave velocity (blue), and S wave velocity structures (red) and plotted. Those for the starting model are shown by dashed lines, and those for the final models are shown by solid lines. The top panel is for KMSC, and the bottom panel is for Y22D. Averaged S wave velocity in the top 30 m (Vs30) in our final model are shown in the title. Also, the U.S. Geological Survey (USGS) Vs30 velocity is given after that. The difference for KMSC (257 m/s vs. 421 m/s) may appear large but considering the differences of our approach from the conventional approach of determining Vs30, those numbers seem quite close. The case for Y22D is particularly close (331 m/s vs. 380 m/s).

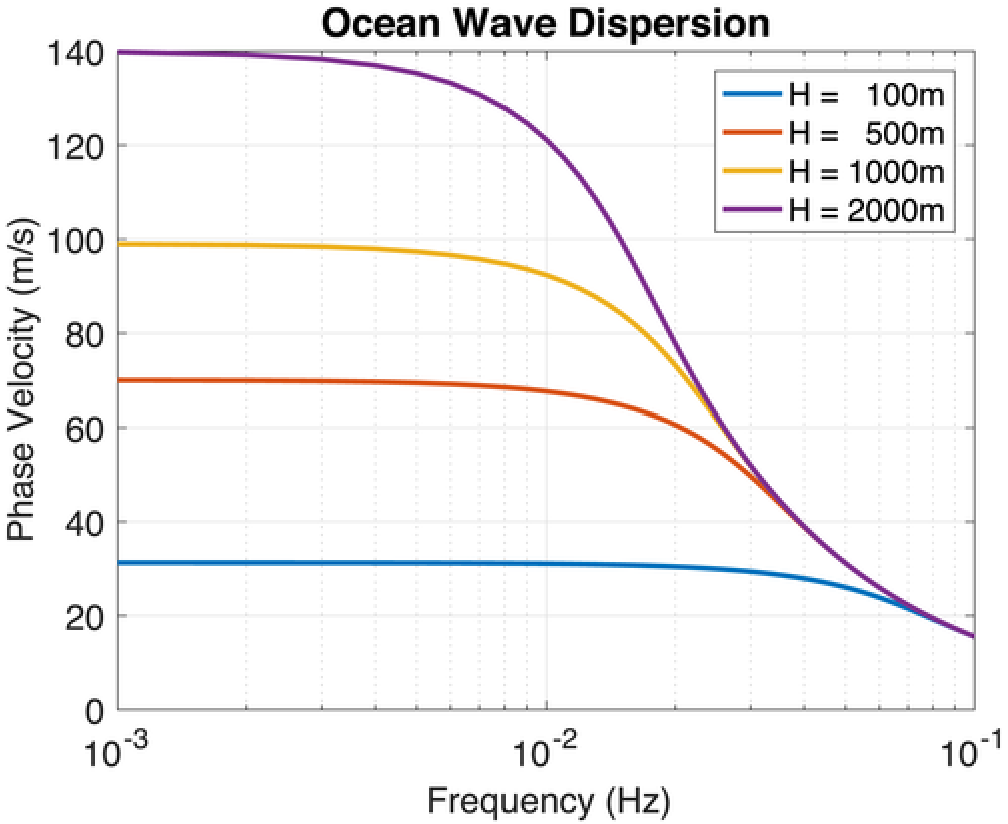

Figure 14. Dispersion of oceanic infragravity waves. Phase speed (c=ω/k) is plotted as a function of frequency. Four cases of ocean depths, 100, 500, 1,000, and 2,000 m are shown. For the frequency range 0.01–0.05 Hz, phase speed varies from about 30 to 120 m/s, approximately 10 – 100 times the pressure wave speed of our atmospheric problems.

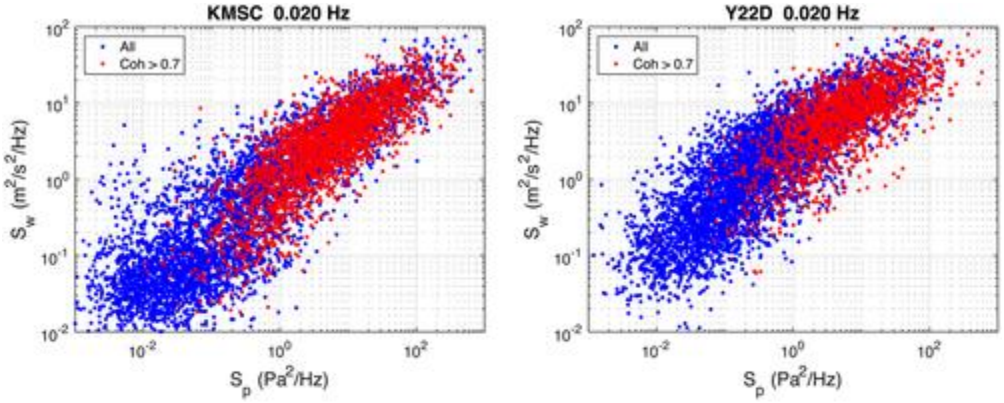

Figure 15. Wind speed power spectral densities are plotted against pressure power spectral densities for KMSC and Y22D. They are at 0.02 Hz and were computed for every 1-hr time interval in 2014. Red points indicate the time intervals when the coherence between vertical seismic data and pressure was higher than 0.7. Our selected data are generally from high wind time intervals.

Frequency (Hz)	S_Z/S_p ($10^{-18}\frac{m^2}{Pa^2s^2}$)	S_H/S_p ($10^{-18}\frac{m^2}{Pa^2s^2}$)	Pressure Wave Speed (m/s)	$\overline{\mu}$ (GPa)
0.010	17.23±10.66	1.461E+05 ± 9.829E+04	1.69±0.77	0.204±0.069
0.015	27.80±11.47	1.505E+05 ± 1.026E+05	1.41±0.56	0.134±0.046
0.020	45.16±16.66	9.236E+04 ± 5.394+04	1.72±0.60	0.128±0.037
0.025	66.26±18.70	7.548E+04 ± 4.160E+04	1.85±0.57	0.114±0.031
0.030	96.73±31.55	5.654E+04 ± 3.291E+04	2.15±0.72	0.109±0.032
0.035	129.16±42.56	4.444E+04 ± 2.554E+04	2.40±0.80	0.106±0.030
0.040	154.17±57.04	3.763E+04 ± 1.885E+04	2.50±0.78	0.101±0.025

Table 1. Measurements for KMSC. Note that S_z/S_p and S_H/S_p are measured and pressure wave speeds and $\overline{\mu}$ are computed from them.

Frequency (Hz)	S_Z/S_p ($10^{-18}\frac{m^2}{Pa^2s^2}$)	S_H/S_p ($10^{-18}\frac{m^2}{Pa^2s^2}$)	Pressure Wave Speed (m/s)	$\overline{\mu}$ (GPa)
0.010	56.78±36.01	6.108E+04 ± 3.819E+04	4.76±2.12	0.316±0.099
0.015	75.33±41.01	3.866E+04 ± 2.274E+04	4.59±1.84	0.264±0.078
0.020	96.26±56.15	2.702E+04 ± 1.859E+04	4.65±2.10	0.237±0.082
0.025	119.04±63.80	1.982E+04 ± 1.179E+04	4.83±1.94	0.222±0.066
0.030	143.97±78.98	1.313E+04 ± 7.611E+03	5.44±2.17	0.227±0.066
0.035	164.42±82.39	9.952E+03 ± 4.842E+03	5.73±2.00	0.223±0.054
0.040	217.62±128.22	7.637E+03 ± 4.325E+03	6.58±2.69	0.223±0.063

Table 2. Measurements for Y22D. Note that S_z/S_p and S_H/S_p are measured and pressure wave speeds and $\overline{\mu}$ are computed from them.

3 Estimating Near-Surface Rigidity from Low-Frequency Noise Using Collocated Pressure and Horizontal Seismic Data

This chapter appeared in this form in:

Wang, J., and T. Tanimoto (2020). Estimating Near-Surface Rigidity from Low-Frequency Noise Using Collocated Pressure and Horizontal Seismic Data, *Bulletin of the Seismological Society of America*. 110, no. 4, 1960–1970, doi: 10.1785/0120200098.

3.1 Abstract

We propose a single-station approach to estimate near-surface elastic structure using collocated pressure and seismic instruments. Our main result in this study is near-surface rigidity (shear modulus) structure at 784 EarthScope Transportable Array (TA) stations in operation from mid-2011 to the end of 2018 using coherent horizontal seismic and pressure signals at 0.02 Hz. We isolate time periods for which surface pressure change is the dominant excitation source for seismic signals by searching for data windows with large pressure variations and high-seismic-pressure coherence. We emphasize the importance of using horizontal seismic components for two reasons: first, horizontal seismic signals are significantly higher than vertical signals at 0.02 Hz due to ground tilt, and second, we can analytically compute the predicted horizontal signals without an assumption of atmospheric pressure wavespeed (which is required for predicting the vertical excitation). Sensitivity kernels from 0.01 to 0.05 Hz show that this pressure–seismic coupling is mostly dependent on rigidity shallower than 50 or 100 m. Our estimates of shallow elastic structure show good spatial agreement with large-scale surface geological features. For instance, stations in the Appalachian Mountains mostly have high rigidity, whereas low-rigidity sites dominate the Mississippi Alluvial Plain. Because of the lack of measured velocity profiles, we quantitatively validate our approach by comparing with V_{S30} models that are based on proxies such as topographic slopes and large-scale surface geology. We estimate near-surface rigidity at 784 TA stations, where these locations have no prior structure information. Our method provides independent information for seismic hazard studies.

3.2 Introduction

When the atmosphere exerts large pressure on the ground, the solid Earth deforms elastically. This interaction has been known and studied since the 1970s, particularly with a model proposed by Sorrells (1971). The amount of deformation reflects the elastic response of the underlying medium. This deformation is recorded as low-frequency seismic noise by broadband seismic instruments and is significant for frequencies between 0.01 and 0.05 Hz as shown by Sorrells (1971), Sorrells et al. (1971), and Sorrells and Goforth (1973). In the context of low-frequency seismic noise, outside of our focused frequency band (0.01–0.05 Hz), there is a primary microseism that starts to dominant above 0.06 Hz (e.g., Bormann and Wielandt, 2013), and the effect of gravitational attraction on the sensor mass from the atmospheric density perturbation is strongest near 3 mHz (Zürn and Wielandt, 2007). Within our focused frequency band, there are potentially some effects from Earth's hum up to 15 mHz (e.g., Suda et al., 1998; Tanimoto et al., 1998) and 26 s microseism signals (Shapiro et al., 2006); however, when pressure variations are large, seismic signals are dominated by surface pressure changes. To explain the mechanism of ground deformation under surface pressure changes, Sorrells (1971) proposed a homogeneous half-space model, in which wind-related moving pressure waves on the ground generate low-frequency seismic signals. Notwithstanding continued study of low-frequency seismic noise (e.g., Beauduin et al., 1996; McNamara and Buland, 2004; De Angelis and Bodin, 2012; Wolin et al., 2015; Hutt et al., 2017), we still have limited quantitative understanding of low-frequency seismic noise, partly because of the historic rarity of stations with collocated pressure and seismic sensors, especially with high-quality pressure sensors accurately measuring the atmospheric pressure. Long-duration collocated records are required to find sufficient time intervals when pressure variations at stations are large enough to exceed other noise sources, allowing us to study the phenomenon of land–atmosphere interaction. Since mid-2011, the EarthScope Transportable Array (TA) has installed high-quality pressure instruments alongside seismic instruments (Tytell et al., 2016), providing an unprecedented dataset to study how the ground deforms under pressure variations. Here, we investigate the process of atmosphere–ground coupling and retrieve the near-surface (tens of meters from the surface) rigidity.

We established the background theory and formulation in our previous study in 2018 (Tanimoto and Wang, 2018). We adopted Sorrells's formulation, applied it to a small subset of TA stations, and developed and tested a procedure for analyzing collocated pressure and seismic signals at 0.01 and 0.02 Hz. The analysis allowed derivation of rigidity structure at those stations. In this article, we extend our previous analysis and compute near-surface rigidity values at 784 TA stations from 2012 to 2018. With the same basic theory as our 2018 project, this article highlights the usage of only horizontal seismic signals. Low-frequency horizontal signals have much larger amplitudes than vertical signals because of large ground tilt, which makes horizontal tilt signals clearly distinguishable from other noise sources such as ocean-generated seismic noise. Meanwhile, half-space rigidity can still be calculated without measuring the vertical seismic component. Our approach can improve existing shallow structural models across the United States such as the U.S. Geological Survey (USGS) V_{S30} model (Wald and Allen, 2007), with implications for seismic hazard analysis (e.g., Shearer and Orcutt, 1987). Our estimations of rigidity at many TA stations provide valuable information at locations without measured velocity profiles.

In the following sections, we present our data analysis procedure, the theoretical basis for the rigidity calculation, spatial rigidity results, and a comparison of our estimates with two proxy-based V_{S30} models.

3.3 Data and Methods

We analyze all TA stations with collocated infrasound pressure sensors and broadband seismometers from 1 January 2012 to 1 January 2019. For the EarthScope (USArray) network, atmospheric pressure data can be obtained from either infrasound sensors (Hyperion microbarometer) or barometers (Setra 278 microbarometer). Pressure variations above 0.01 Hz from two pressure instruments are consistent (Tanimoto and Wang, 2018). In this study, we use the pressure data from infrasound instruments. Raw seismic data from TA stations have a sampling rate of 100 Hz (HH*), and raw pressure data have a sampling rate of 40 Hz (BDF). We use 1 Hz channels (LH*; LDF;) for all pressure and seismic data because they are sufficient for analyzing 0.01–0.05 Hz signals.

For TA stations in the contiguous United States, seismometers and pressure sensors are housed within vaults, and pressure sensors are connected to the outside through an inlet tube to allow measurement of atmospheric surface pressure. The configuration described previously can be found in figure 4 of Tytell et al. (2016). The configuration of Alaska TA stations can be found on the USArray website (see Data and Resources); the setup of the Alaska TA stations is similar to contiguous TA stations in terms of the spacing between pressure and seismic measurements. Because of the consistency of installation protocols among TA stations, it provides a natural control to avoid the complexity of recorded low-frequency noise that might arise from different installation types (e.g., vault, direct burial). All seismic and pressure data are downloaded from the Incorporated Research Institutions for Seismology (IRIS) Data Management Center, and the data are a product of the EarthScope USArray project (see Data and Resources).

For all seismic and pressure data, we compute the power spectral density (PSD) using 1 hr time series throughout the time span of each station, which is typically 2 yr (Tytell et al., 2016). Hourly PSDs are effective while studying seismic noise at low frequencies (e.g., McNamara and Buland, 2004). For each 1 hr time series, we detrend, apply a Hanning window, compute Fourier spectra, deconvolve instrument response, and obtain PSDs at frequencies between 0.01 and 0.05 Hz with an increment of 0.005 Hz. In this article, we mainly report the rigidity estimates at 0.02 Hz, but the estimates from adjacent frequencies provide similar results (see the supplemental material available to this article), and later we elucidate the reason of choosing 0.02 Hz. The frequency dependence of halfspace rigidity estimates provides a basis for the layered model (Tanimoto and Wang, 2019), which is not discussed in this project.

Figure 1a shows a simplified model of pressure plane waves propagating on the Earth's surface. This excitation source model is the same as figure 3a in Tanimoto and Wang (2018), which follows Sorrells (1971). This panel shows that plane pressure waves are propagating in the azimuth ϕ from the east (the x axis). A typical collocated station is located at the origin of this coordinate system. The propagating plain waves are from surface pressure changes caused by atmospheric winds, which are composed of mainstream flow and atmospheric turbulence (Tanimoto and Wang, 2019). Large pressure changes can cause elastic deformation of the ground and become the dominant source of energy at low-frequency band of 0.01–0.05 Hz, as we can show in the pressure–seismic plots.

Figure 1b illustrates the standard data-analysis steps in our method. We perform the same analysis on all TA stations. Details of each steps described in the flow chart are explained further in the following sections.

In the Data and Methods section, we discuss our data-culling procedures based on coherence analysis, correlation between pressure and seismic signals, fundamental equations, characteristics of tilt-dominated horizontal seismic signals, use of the trimmed mean method, and uncertainty constraints.

3.3.1 Data Culling using Coherence and Pressure

When low-frequency seismic data are mostly generated by atmospheric pressure variations, coherence between pressure and seismic signals becomes high. Low coherence indicates that low-frequency seismic noise is predominated by non-pressure noise sources, so we limit our analysis to time intervals with coherence higher than a threshold value (explained later). We compute hourly coherence between seismic and pressure signals at all stations and use them for the data culling. Coherence is computed between the vertical seismic component and pressure (V-P), between the north–south seismic component and pressure (NS-P), and between the east–west seismic component and pressure (EW-P). We compute coherence by its standard definition:

$$\boldsymbol{Coh(f)} = \left| \frac{\boldsymbol{E[X^{*}(f)Y(f)]}}{\sqrt{\boldsymbol{E[X^{*}(f)X(f)]E[Y^{*}(f)Y(f)]}}} \right| \qquad \mathbf{(1)}$$

in which *E[]* represents ensemble averaging and *X(f)*, *Y(f)* are seismic and pressure spectra, respectively. In practice, we divide 1 hr time series into 11 overlapping 10 min time series by shifting each starting time by 5 min. The ensemble spectrum is the average of these 11 spectra. Pressure and seismic signals often have peak coherence between 0.01 and 0.03 Hz (Tanimoto and Wang, 2018). As increasing frequencies approach 0.05 Hz, coherence starts to decrease, for which the ocean-generated primary microseism (typically near 0.06 Hz) starts to dominate.

We implement a three-step data-culling process to choose time intervals for the analysis. First, we only include horizontal PSDs at time intervals when both NS-P and EW-P coherences are higher than 0.7. Time intervals that are dominated by other signals such as earthquakes will be culled by this step because coherence between local pressure and seismic signals will become low. Other low-coherence time intervals are likely affected by energy from ocean waves. Only horizontal seismic PSDs are relevant for the half-space rigidity calculation. We examined different choices of coherence cutoff values between 0.5 and 0.9. Lower coherence cutoff values yield less culling but may contain more contamination from unwanted noise. Higher coherence cutoff values can lead to more precise estimates at individual stations, but the number of stations that pass the culling process becomes quite low. We choose 0.7 to balance both effects. Second, we use time intervals when the local pressure variations are large (pressure PSDs higher than 1 Pa^2/Hz) to ensure high-signal-to-noise ratios because direct ground deformation is more significant as a response to higher local pressure variations, whereas seismic signals from other noise sources remain the same. Third, we only report rigidities at stations that have at least 50 1 hr time intervals that passed the previous quality control steps in each year (i.e., >50 green points in Fig. 2) to ensure the robustness of our results.

There are 912 collocated stations with available data from 2012 to 2018. After the data-culling process and visual inspection of the data (see supplemental material for erroneous examples), the number of stations used for rigidity estimation decreased to 784. There are two possibilities to physically explain why culled stations have low coherence throughout this time period. First, these stations may never experience large pressure variations because of their local microclimates. Second, near-surface structure below the station may be too rigid; therefore, the amount of deformation caused by pressure changes is too small to be separated from other noise sources. These culled stations aside, the 784 qualifying stations clearly show that the surface pressure changes are the dominating factor for seismic noise when pressure variations are large and coherence is high.

3.3.2 Pressure-Seismic Plots

Following an approach we developed in Tanimoto and Wang (2018), we plot pressure signals against seismic signals at 0.02 Hz and name them pressure–seismic plots. Figure 2 shows pressure–seismic plots of two TA stations, 355A and I05D, which both show surface-pressure PSDs plotted against horizontal and vertical seismic PSDs on log–log scales. Plotted horizontal PSDs are the sum of north–south and east–west PSDs (Tanimoto and Wang, 2018). All points represent hourly data points in 2012. “Coherent” points are time intervals selected by the data-culling procedure described in the previous section. Linear correlations between pressure and seismic data support the idea that our data-culling procedure effectively picks out time intervals when seismic signals are generated by atmospheric pressure variations. Although low-frequency seismic noise can be complex and caused by other various factors such as sensor type, temperature change, and other sources mentioned in the Introduction, the linear trend among green points implies that atmospheric pressure changes are indeed the controlling factor for low-frequency seismic noise and is generally present in all three seismic components when pressure variations are large. These plots nicely illustrate the importance of careful data selection from long-recording stations; if one were to blindly analyze collocated data at low frequencies without focusing on specific time intervals or to look at data with too short of a duration, one would include data along the flat parts of Figure 2 that are uncorrelated and then introduce false information in terms of the land–atmosphere interaction.

We generate these pressure–seismic plots for all stations. These pressure–seismic plots help visualize the correlation between pressure and seismic signals. This correlation is key to our analysis of shallow rigidity.

3.3.3 Rigidity Calculation

The fundamental relationships between seismic PSDs and pressure PSDs are described by equations (2) and (3). These relationships include the homogeneous half-space assumption; detailed derivation can be found in Tanimoto and Wang (2018). In equation (2), we already dropped the term of pressure-generated horizontal deformation and kept only the term of tilt-related noise because the tilt term is much larger at low frequencies. The general expression of theoretical horizontal signals is equation (9) and is discussed in the next section.

$$\frac{S_H(\omega)}{S_P(\omega)} = \frac{g^2}{4\omega^2\mu^2}\left(\frac{\lambda + 2\mu}{\lambda + \mu}\right)^2 = \frac{g^2}{4\omega^2\bar{\mu}^2} \tag{2}$$

$$\frac{S_Z(\omega)}{S_P(\omega)} = \frac{c^2}{4\mu^2}\left(\frac{\lambda + 2\mu}{\lambda + \mu}\right)^2 = \frac{c^2}{4\bar{\mu}^2} \tag{3}$$

in which we define

$$\bar{\mu} = \frac{\lambda + \mu}{\lambda + 2\mu}\mu \tag{4}$$

and $\frac{\lambda+\mu}{\lambda+2\mu}$ can be rewritten as

$$\frac{\lambda + \mu}{\lambda + 2\mu} = 1 - \left(\frac{V_S}{V_P}\right)^2 \tag{5}$$

$S_H(\omega) = \frac{|\omega U_H|^2}{T}$, $S_Z(\omega) = \frac{|\omega U_Z|^2}{T}$, and $S_P(\omega) = \frac{|P(\omega)|^2}{T}$ are the horizontal seismic velocity PSD, vertical seismic velocity PSD, and pressure PSD, respectively. $U_H(\omega)$, $U_Z(\omega)$, and $P(\omega)$ are Fourier spectra of horizontal seismic displacement, vertical seismic displacement, and pressure, respectively. T is the length of time series (1 hr). $S_H(\omega)$ is the sum of two horizontal PSDs (Tanimoto and Wang, 2018). g is the gravitational acceleration (9.8 m/s^2). c is the pressure wavespeed at the surface. ω is the angular frequency. λ is the Lamé's first parameter. μ is the rigidity (elastic shear modulus).

In equations (2) and (3), there are two unknowns $\bar{\mu}$ and c. $\bar{\mu}$ is the "modified" rigidity that differs from μ by a factor of $\frac{\lambda+\mu}{\lambda+2\mu}$, and c is the speed of main-stream pressure waves. However, equation (2) indicates that we can estimate $\bar{\mu}$ from the ratio $\frac{S_H(\omega)}{S_P(\omega)}$ without measuring $\frac{S_Z(\omega)}{S_P(\omega)}$. All of our rigidity results in this article are hereafter based on $\frac{S_H(\omega)}{S_P(\omega)}$ only. After getting estimates of $\bar{\mu}$, the pressure wavespeed c can be determined from equation (3).

From these equations, it is evident that we can only directly determine $\bar{\mu}$ from data instead of μ. $\bar{\mu}$ typically approaches μ near the surface because μ is small near the surface (e.g., Brocher, 2005, 2016) where there are often unconsolidated layers.

We can empirically convert $\bar{\mu}$ to μ and V_S using a combination of equations (5) (Tanimoto and Wang, 2018), $\mu = \rho V_S^2$ and equations (6) – (8) subsequently. Although we can only directly constrain $\bar{\mu}$, we convert $\bar{\mu}$ into V_S because V_S is more commonly used in seismic hazard studies (e.g., Vs30). Equations (6) – (8) are empirical relations among density and seismic velocities from Gardner et al (1974), Brocher (2005), and Boore (2016):

For $V_S < 0.3$ km/s:

$$\rho = 1 + \frac{1.53V_S^{0.85}}{0.35 + 1.889V_S^{1.7}} \tag{6}$$

For 0.3 km/s < V_S < 3.55 km/s

$$\rho = 1.74V_P^{0.25} \tag{7}$$

For V_P:

$$V_P = 0.9409 + 2.0947V_S - 0.8206V_S^2 + 0.2683V_S^3 - 0.0251V_S^4 \tag{8}$$

3.3.4 Justification for Using Horizontal Data Only

$$S_H(\omega) = \left\{\frac{c}{2(\lambda + \mu)} - \frac{g}{2\omega\mu}\frac{\lambda + 2\mu}{\lambda + \mu}\right\}^2 S_{p(\omega)} \tag{9}$$

One major difference between this project and that of Tanimoto and Wang (2018) is that here we emphasize the use of only horizontal signals for estimating half-space rigidity. This change is justified by consideration of equation (9). Equation (9) is the general expression of theoretical horizontal seismic signals under surface pressure loading. The first term represents horizontal ground deformation, which should have comparable amplitude to vertical deformation. The second term represents ground tilt on the horizontal component that has been studied since Rodgers (1968). In observed low-frequency horizontal signals, the tilt term is much larger than the actual deformation because $\frac{g}{2\omega\mu}$ becomes large; therefore, the first term is dropped and turns equation (9) into (2). However, the amount of horizontal tilt is still a function of the elastic response of the solid Earth. At the same time, the horizontal amplitude from pressure-caused tilt can be much larger and surpass other sources of noise that could potentially be masking direct pressure-caused ground deformation in the vertical signals. This can be observed in the pressure–seismic plots (e.g., Fig. 2), where the horizontal amplitude is much larger than the vertical amplitude. Therefore, it is naturally more advantageous to only analyze "tilt-contaminated" horizontal signals for the half-space model using equation (2) because of the high-signal-to-noise ratio.

3.3.5 Trimmed Means and Uncertainties

To obtain robust $\frac{S_H(\omega)}{S_P(\omega)}$ values for estimating rigidity, we use a 20% trimmed mean method (e.g., Wilcox, 2012), for which we trim off the 20% most extreme values from both ends of the sorted vector of $\frac{S_H(\omega)}{S_P(\omega)}$ ratio. Figure 3 shows the procedure and effectiveness of the trimmed mean method. For station E45A in 2012, the trimmed mean does not differ much from the arithmetic mean because there are no significant outliers. However, for station 758A in 2012, there are several outliers at ratios around 10^{-10}, whereas most values lie between 10^{-14} and 10^{-12}. As a result, the arithmetic mean is significantly skewed to a higher value, whereas the trimmed mean value more accurately describes the majority of data at the station. In the case of 758A, the 20% trimmed mean is a much better metric to quantify the behavior of the station. We tested trimmed means with different percentages (5%, 10%, 20%, and 30%), and they gave similar results; 20% proved to be a good balance between effectively eliminating outliers and keeping as much of the data as possible.

The procedure for determining uncertainties is tied to the trimmed mean method. For a single station in each year, we estimate uncertainty by first calculating rigidity values from all individual $\frac{S_H(\omega)}{S_P(\omega)}$ ratios from time intervals that passed the quality control criteria (see earlier) and fell within trimmed bounds. For example, at a single station, if there are 100 $\frac{S_H(\omega)}{S_P(\omega)}$ ratios within 20% trimmed bounds (i.e., vertical solid lines in Fig. 3c,d), we compute 100 rigidity values using equation (2). Then we use one standard deviation of the distribution of rigidity values at each station as the uncertainty. Uncertainty estimates for $\bar{\mu}$ and V_S are generally between 10% and 30% after applying the 20% trimmed mean method. We estimate rigidity and uncertainty for every individual year rather than for the entire station duration because it allows for examining temporal variations from year to year. Most stations operated at the same location for 2 years or less (Tytell et al., 2016). TA backbone stations are exceptions and some backbone stations remained operational from 2012 to 2018. We calculate rigidities for all 7 yr at 13 backbone stations. Results from different years are consistent within uncertainties. The consistency suggests our method is accurately measuring stable, site-specific structure that do not change much from year to year (as expected for near-surface geology). The multiyear plots can be found in the supplemental material.

3.4 Rigidity Results

3.4.1 Depth Sensitivity Kernels

In a separate study (Tanimoto and Wang, 2019), we developed a theory to calculate the depth sensitivity kernels of rigidity. The method is based on numerical differentiation.

Sensitivity kernels depend strongly on frequencies and are also controlled by atmospheric pressure wavespeed c, which can be estimated from equations (2) and (3). Because observed pressure wavespeeds do not vary much between stations, sensitivity kernels peak at similar depths between different stations. In Figure 4, we show rigidity sensitivity kernels computed at two stations 355A and I05D (the same pair of stations as in Fig. 2). Density, V_P, and V_S profiles in each starting model are simply converted from our half-space rigidities ($\bar{\mu}$) at 0.02 Hz at two stations (218.4 MPa for 355A and 616.1 MPa for I05D) using equations (6) – (8). Density, V_P, and V_S values of starting models are 1948 kg/m3, 1572 m/s, and 343 m/s, respectively, for 355A and are 2048 kg/m3, 1922 m/s, and 575 m/s for I05D, respectively. In Figure 4, it is clear that our data in the frequency range from 0.01 to 0.05 Hz constrain elastic rigidity of the top 50 or 100 m beneath each station, by looking at peak depths of kernels at these frequencies. In this project, we report rigidity values at 0.02 Hz. We select 0.02 Hz mainly because the sensitivity kernels for different stations often peak at around 20–40 m at 0.02 Hz; therefore, results at 0.02 Hz are potentially comparable to V_{S30}, which is a time-averaged quantity to 30 m depth.

3.4.2 Spatial Rigidity Results

Figure 5 shows the V_S estimates derived from rigidities at 784 TA stations. Values (with uncertainties) computed at each station are listed in the supplemental material. There are two noticeable geological features in Figure 5. First is a region in the northeast United States that has many high-rigidity V_S stations. This area corresponds to the Appalachian Mountains, where high-rigidity bedrock is exposed at or near the surface, producing high V_S. Second is a region in the Mississippi Alluvial Plain that has many low-rigidity/V_S stations. This area is mostly composed of soft alluvial sediments with low rigidity; therefore, shallow low-V_S layers are expected. The eight highest rigidity stations are in Alaska, and 40 out of 50 highest rigidity stations are either in Alaska or Yukon Territory in Canada. These stations may be recording less deformation under pressure loading because of permafrost near the surface, which is predicted to have high rigidity. The two lowest rigidity stations are also located in Alaska (R32K and S32K). Both stations are located on islands within the Alexander Archipelago and could potentially be sitting on soft alluvial deposits. In Figure 5, most stations are located in the eastern contiguous United States because pressure sensors were routinely installed at TA stations for deployment after mid-2011, postdating TA deployment in the western United States.

Figure 6 demonstrates differences in values between three groups: all stations in the contiguous United States (excluding stations in Alaska and Canada), stations on the Appalachian Mountains, and stations on the Mississippian Alluvial Plain. The first group includes the other two groups. Stations identified as “Appalachian” and “Mississippi” are mapped in Figure 7c and listed in the supplemental material. The box plot shows statistical analysis of the distribution of converted V_S values for these three groups of stations. Although the error bars (±2.7σ) are large and overlapping for “all” and “Appalachian” stations, the median values (lines in the center of each box) are quite distinct among the three groups of stations. Group “all” includes 622 contiguous United States’ stations with a median V_S of 382.3 m/s, with 25th and 75th percentile values of 314.6 m/s and 511.5 m/s, respectively. The “Appalachian” group includes 127 stations with a median V_S of 564.9 m/s, with 25th and 75th percentile values of 445.4 m/s and 691.9 m/s, respectively. The 31 “Mississippi” stations have a median V_S of 233.4 m/s, with 25th and 75th percentile values of 195.2 m/s and 273.0 m/s, respectively. All “Mississippi” stations’ V_S values are consistent within the group (no outlier point). The box plot confirms the spatial features observed in Figure 5: for stations in the contiguous United States, most high- V_S stations are along the Appalachian region, and most low- V_S stations are located within the Mississippi Alluvial Plain. This result is consistent with our general knowledge of near-surface geology in the eastern United States.

3.4.3 Comparison with Various V_{S30} Models

The sensitivity kernels illustrated in Figure 4 show a peak of 20 – 30 m at 0.02 Hz, which is the depth range of a commonly used parameter in seismic hazard studies: V_{S30}. V_{S30} is averaged V_S down to 30 m. Unfortunately, there are no measured V_{S30} values at any TA station. Therefore, we seek quantitative validation of our approach by comparing our results at 0.02 Hz with two proxy-based V_{S30} models. Figure 7 illustrates the correlation between V_{S30} values from two models and our converted V_S results. The USGS V_{S30} model mainly uses topographic slopes as a proxy to infer V_{S30} (Wald and Allen, 2007). Figure 7a,b shows correlation between our results and V_{S30} interpolated from USGS's 30 arcsec grid. Selected "Appalachian" and "Mississippi" stations' names are listed in the supplemental material. There is an upper limit of 900 m/s in the USGS V_{S30} model, hence the sharp boundary denoted as vertical dashed lines in Figure 7a,b. Correlations between our V_S and USGS proxy-inferred V_{S30} at all 784 stations (all points in Fig. 7a) show large scattering. However, if we focus only on "Appalachian" and "Mississippi" stations in Figure 7a, we clearly find two distinct subgroups of the entire dataset, for which "Mississippi" stations generally have low V_{S30} and low-converted V_S and "Appalachian" stations generally have high V_{S30} and high-converted V_S. Figure 7b highlights this pattern by focusing on these two subgroups of stations, revealing a (weak) correlation between the USGS model and our results.

Figure 7d shows comparison between our results and the Central and Eastern North America (CENA) V_{S30} model from Goulet et al (2014) at 216 TA stations. V_{S30} values are obtained from the supplemental materials of Goulet et al (2014). Goulet et al (2014) uses various measured profiles (none nearby TA stations) and various proxy-based V_{S30} models in CENA to produce "preferred" V_{S30} values. We observe positive correlation between our results and the CENA V_{S30} model, especially at lower V_{S30} ranges, which further validates our approach.

3.5 Conclusion

We have presented a single-station method for measuring shallow elastic structure using pressure and horizontal seismic data from collocated stations in the EarthScope TA. The method uses low-frequency (0.01– 0.05 Hz) horizontal seismic noise generated by the atmospheric pressure loading on the solid Earth. When studying the interaction between low-frequency seismic noise and surface-pressure variations, it is crucial to select data during time intervals with large pressure changes and high-seismic-pressure coherence. Our method uses natural noise as the source of data and is cost-effective compared with traditional approaches that often involve geophone array or drilling; both require laborious field work of multi-person teams. We determine near-surface rigidity at 784 stations, finding regional correlation between our results and surface geological features such as in the Appalachian Mountains and the Mississippi Alluvial Plain. The existence of largescale patterns is somewhat surprising because near-surface structure can manifest substantial lateral heterogeneity. The regional patterns in our rigidity estimates demonstrate that there is a good deal of consistency in surface rocks or sediments across some large geological provinces; the spatial correlation between our results and regional geology in the Appalachian Mountains and the Mississippi Alluvial Plain supports such a connection. The correlation between two proxy-based V_{S30} models and our results in the Appalachian Mountains and the Mississippi Alluvial Plain validates the potential of using our method as an independent metric to improve V_{S30} maps. There is no measured velocity profiles at 784 TA stations. Our estimated near-surface rigidity at these stations provides new information for seismic hazard studies. We believe further comparison and tests on V_{S30} models are important because the existence of near-surface low-rigidity layers has the potential to drastically amplify seismic ground motions; our approach and results can contribute to this field of study.

3.6 Data and Resources

All seismic and pressure data are openly available and were acquired from Incorporated Research Institutions for Seismology (IRIS) at ds.iris.edu/mda/TA using ObsPy (Beyreuther et al. (2010), available at https://github.com/obspy/obspy/wiki). The entire dataset is the product of the Transportable Array (TA) project from the EarthScope USArray available at www.usarray.org/researchers/data. The configuration of Alaska TA stations can be found in Figure 4 available at www.usarray .org/alaska#station-design. The basemap of Figure 5c is the U.S. Geological Survey (USGS) VS30 model available at earthquake.usgs.gov/data/vs30. Our seismic and pressure output files used for plotting and computed rigidity results' files can be obtained at http://dx.doi.org/10.5281/zenodo.3669335 (Seismic and pressure data for Wang and Tanimoto). All figures were generated using MATLAB (http:// www.mathworks.com/products/matlab) and Generic Mapping Tools (GMT, Wessel et al., 2013), available at http://gmt.soest.hawaii.edu. All websites were last accessed in February 2020. The supplemental material includes Figure S1 mentioned in the Data and Methods section, Figures S2 and S3 mentioned in the Data culling using coherence and pressure section, and Tables S1–S3 mentioned in the Spatial rigidity results section. Tables S1–S3 are in separate .csv files.

3.7 Reference

Beauduin, R., P. Lognonné, J. P. Montagner, S. Cacho, J. F. Karczewski, and M. Morand (1996). The effects of the atmospheric pressure changes on seismic signals or how to improve the quality of a station, *Bulletin of the Seismological Society of America*. 86, no. 6, 1760.

Beyreuther, M., R. Barsch, L. Krischer, T. Megies, Y. Behr, and J. Wassermann (2010). Obspy: A python toolbox for seismology, *Seismological Research Letters*. 81, no. 3, 530–533, doi: 10.1785/gssrl.81.3.530.

Boore, D. M. (2016). Determining generic velocity and density models for crustal amplification calculations, with an update of the Boore and Joyner (1997) generic site amplification for graphic site amplification, *Bulletin of the Seismological Society of America*. 106, no. 1, 313, doi: 10.1785/ 0120150229.

Bormann, P., and E. Wielandt (2013). Seismic signals and noise, Chapter 4, in *New Manual of Seismological Observatory Practice (NMSOP-2)*, P. Bormann (Editor), IASPEI, GFZ German Research Centre for Geosciences, Potsdam, Germany, doi: 10.2312/GFZ.NMSOP-2.

Brocher, T. M. (2005). Empirical relations between elastic wavespeeds and density in the earth’s crust, *Bulletin of the Seismological Society of America*. 95, no. 6, 2081–2092, doi: 10.1785/0120050077.

De Angelis, S., and P. Bodin (2012). Watching the wind: Seismic data contamination at long periods due to atmospheric pressure field induced tilting, *Bulletin of the Seismological Society of America*. 102, no. 3, 1255–1265, doi: 10.1785/0120110186.

Gardner, G., L. W. Gardner, and A. R. Gregory (1974). Formation velocity and density-the diagnostic basics for stratigraphic traps, *Geophysics* 39, no. 6, 759–918, doi: 10.1190/1.1440465.

Goulet, C. A, T. Kishida, T. D. Ancheta, C. H. Cramer, R. B. Darragh, W. J. Silva, Y. M. Hashash, J. Harmon, J. P. Stewart, K. E. Wooddell, et al. (2014). *PEER NGA-East database*, *PEER Rept*. *2014/17*, https://peer.berkeley.edu/research/nga-east/products (last accessed February 2020).

Hutt, C. R., A. T. Ringler, and L. S. Gee (2017). Broadband seismic noise attenuation versus depth at the Albuquerque seismological laboratory, *Bulletin of the Seismological Society of America*. 107, no. 3, 1402–1412, doi: 10.1785/0120160187.

McNamara, D. E., and R. P. Buland (2004). Ambient noise levels in the continental United States, *Bulletin of the Seismological Society of America*. 94, no. 4, 1517–1527, doi: 10.1785/012003001.

Rodgers, P. W. (1968). The response of the horizontal pendulum seismometer to Rayleigh and love waves, tilt, and free oscillations of the earth, *Bulletin of the Seismological Society of America*. 58, no. 5, 1385–1406.

Shapiro, N. M, M. H. Ritzwoller, and G. D. Bensen (2006). Source location of the 26 sec microseism from cross-correlations of ambient seismic noise, *Geophysical Research Letters*. 33, no. 18, L18310 , doi: 10.1029/2006GL027010.

Shearer, P. M., and J. A. Orcutt (1987). Surface and near-surface effects on seismic waves theory and borehole seismometer results, *Bulletin of the Seismological Society of America*. 77, no. 4, 1168–1196.

Sorrells, G. G. (1971). A preliminary investigation into the relationship between long-period seismic noise and local fluctuations in the atmospheric pressure field, *Geophysical Journal International*. 26, nos. 1/4, 71–82, doi: 10.1111/j.1365-246X.1971.tb03383.x.

Sorrells, G. G., and T. T. Goforth (1973). Low-frequency earth motion generated by slowly propagating partially organized pressure fields, *Bulletin of the Seismological Society of America*. 63, no. 5, 1583–1601.

Sorrells, G. G., J. A. McDonald, Z. A. Der, and E. Herrin (1971). Earth motion caused by local atmospheric pressure changes, *Geophysical Journal International*. 26, nos. 1/4, 83–98, doi: 10.1111/j.1365-246X.1971 .tb03384.x.

Suda, N., K. Nawa, and Y. Fukao (1998). Earth's background free oscillations, *Science* 279, no. 5359, 2089–2091, doi: 10.1126/science.279.5359.2089.

Tanimoto, T., J. Um, K. Nishida, and N. Kobayshi (1998). Earth's continuous oscillations observed on seismically quiet days, *Geophysical Research Letters*. 25, no. 10, 1553–1556, doi: 10.1029/98GL01223.

Tanimoto, T., and J. Wang (2018). Low-frequency seismic noise characteristics from the analysis of co-located seismic and pressure data, *Journal of Geophysical Research: Solid Earth*. 123, no. 7, 5853–5885, doi: 10.1029/2018JB015519.

Tanimoto, T., and J. Wang (2019). Theory for deriving shallow elasticity structure from colocated seismic and pressure data, *Journal of Geophysical Research: Solid Earth*. 124, no. 6, 5811–5835, doi: 10.1029/2018JB017132.

Tytell, J., F. Vernon, M. Hedlin, C. de Groot Hedlin, J. Reyes, B. Busby, K. Hafner, and J. Eakins (2016). The USArray transportable array as a platform for weather observation and research, *Bulletin of the American Meteorological Society*. 97, 603–619, doi: 10.1175/BAMS-D-14- 00204.1.

Wald, D., and T. Allen (2007). Topographic slope as a proxy for seismic site conditions and amplification, *Bulletin of the Seismological Society of America*. 97, no. 5, 1379–1395, doi: 10.1785/0120060267.

Wessel, P., W. H. F. Smith, R. Scharroo, J. Luis, and F. Wobbe (2013). Generic mapping tools: Improved version released, *Eos Trans. AGU* 94, no. 45, 409–410, doi: 10.1002/2013EO450001.

Wilcox, R. (2012). Estimating measures of location and scale, Chapter 3, in *Introduction to Robust Estimation and Hypothesis Testing*, Third Ed., R. Wilcox (Editor), Statistical Modeling and Decision Science, Academic Press, Boston, Massachusetts, 43–101.

Wolin, E., S. van der Lee, T. Bollmann, D. Wiens, J. Revenaugh, F. Darbyshire, A. Frederiksen, S. Stein, and M. Wysession (2015). Seasonal and diurnal variations in long-period noise at spree stations: The influence of soil characteristics on shallow stations performance, *Bulletin of the Seismological Society of America*. 105, no. 5, 2433–2452, doi: 10.1785/0120150046.

Zürn, W., and E. Wielandt (2007). On the minimum of vertical seismic noise near 3 mHz, *Geophysical Journal International*. 168, no. 2, 647–658, doi: 10.1111/j.1365-246X.2006.03189.x.

3.8 Figures and Tables

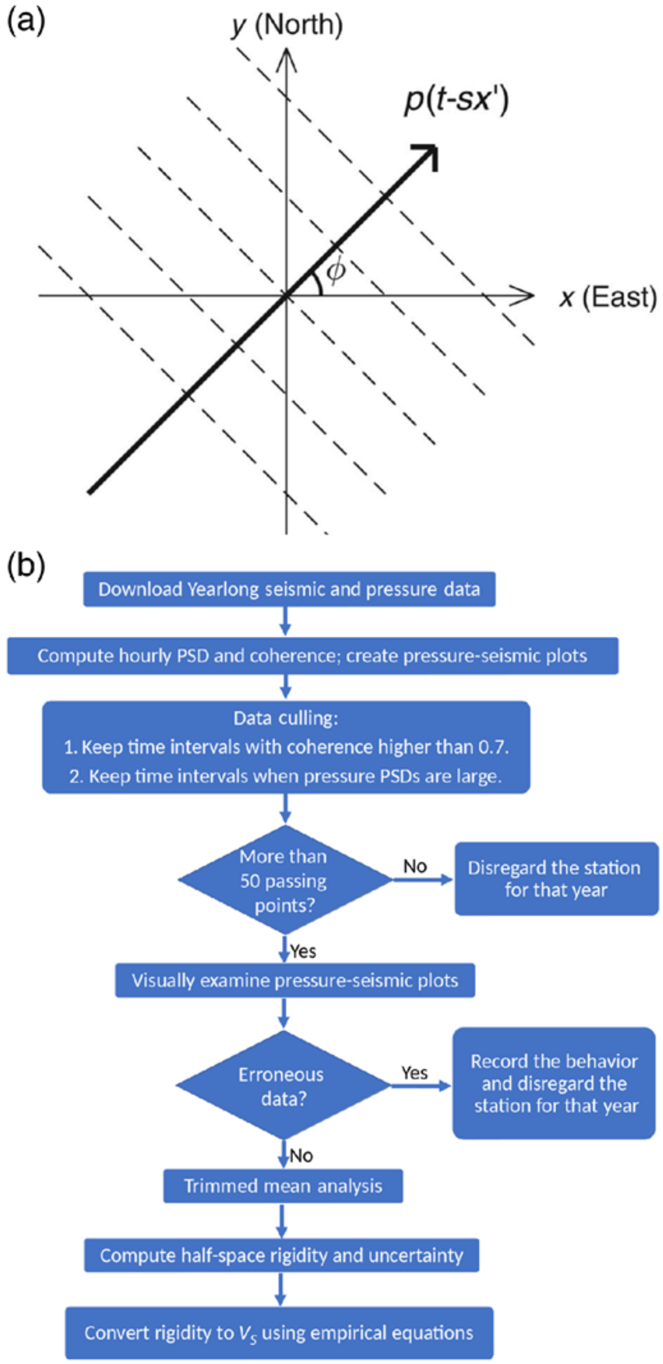

Figure 1. (a) Simplified excitation source model. Same as figure 3a in Tanimoto and Wang (2018). Arrow with the solid line represents the propagating pressure wave. A collocated station is at the origin. (b) Flowchart shows the step - by - step data analysis in our method. Data for each station of each year go through this standard process. The color version of this figure is available only in the electronic edition.

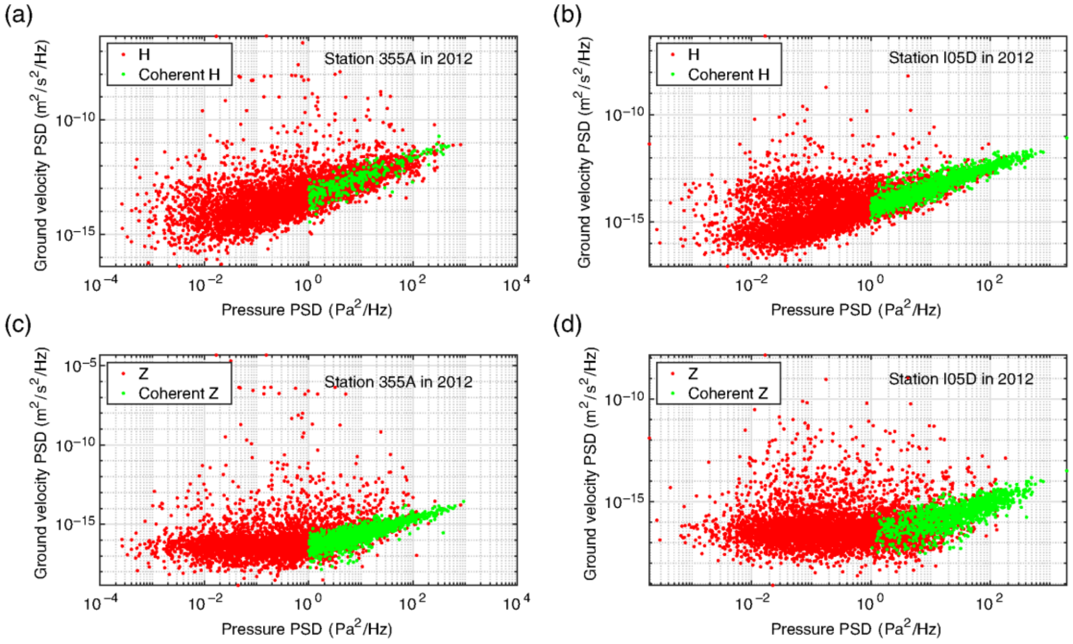

Figure 2. Comparison of ground velocity and pressure power spectral densities (PSDs) at two stations, (a,c) 355A and (b,d) I05D, at 0.02 Hz. Each point is a 1 hr PSD. Red points are horizontal and vertical components for the whole year of 2012; green points are qualified PSDs after data culling. 355A is a Transportable Array (TA) station located at Pearson, Georgia. I05D is a TA station located at Terrebonne, Oregon. The color version of this figure is available only in the electronic edition.

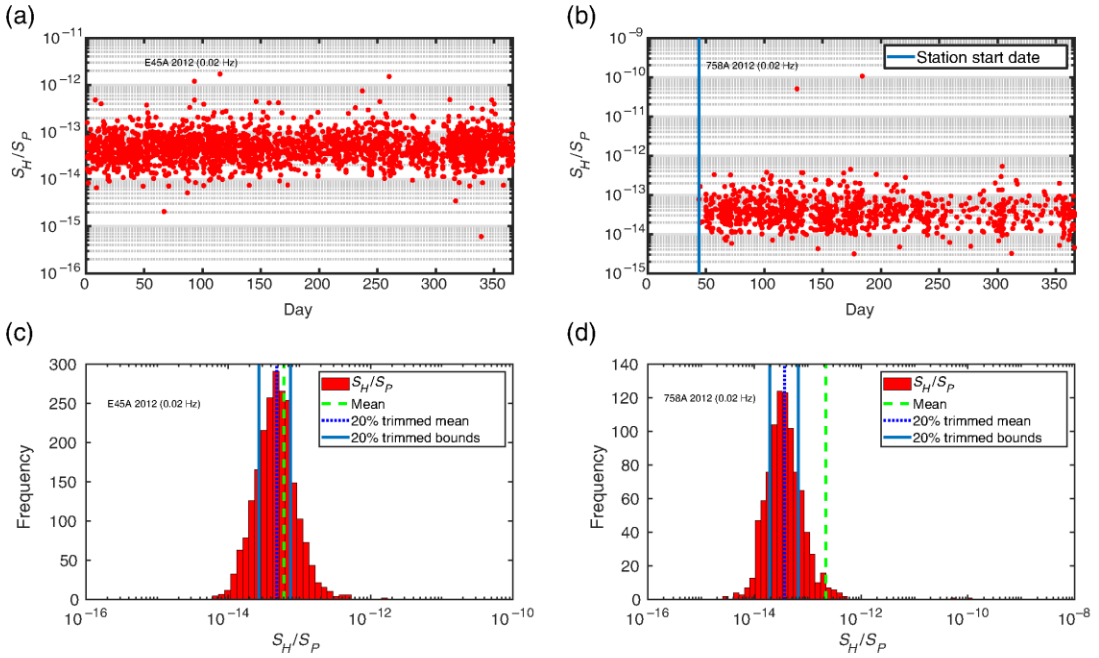

Figure 3. The 20% trimmed mean method at two stations (a,c) E45A and (b,d) 758A. (a,b) $\frac{S_H(\omega)}{S_P(\omega)}$ ratios from all qualified PSDs in 2012. Note that 758A started to operate on 13 February 2012. (c,d) Distributions of $\frac{S_H(\omega)}{S_P(\omega)}$ in histograms. Green dashed lines represent arithmetic means for all ratios. Blue solid lines represent 20% trimmed mean bounds (lower and higher limits). Blue dashed lines show 20% trimmed means, which are the arithmetic means of ratios that fall within 20% trimmed mean bounds. E45A is a TA station located in Hulbert, Michigan. 758A is a TA station located in Lake Helen, Florida. The color version of this figure is available only in the electronic edition.

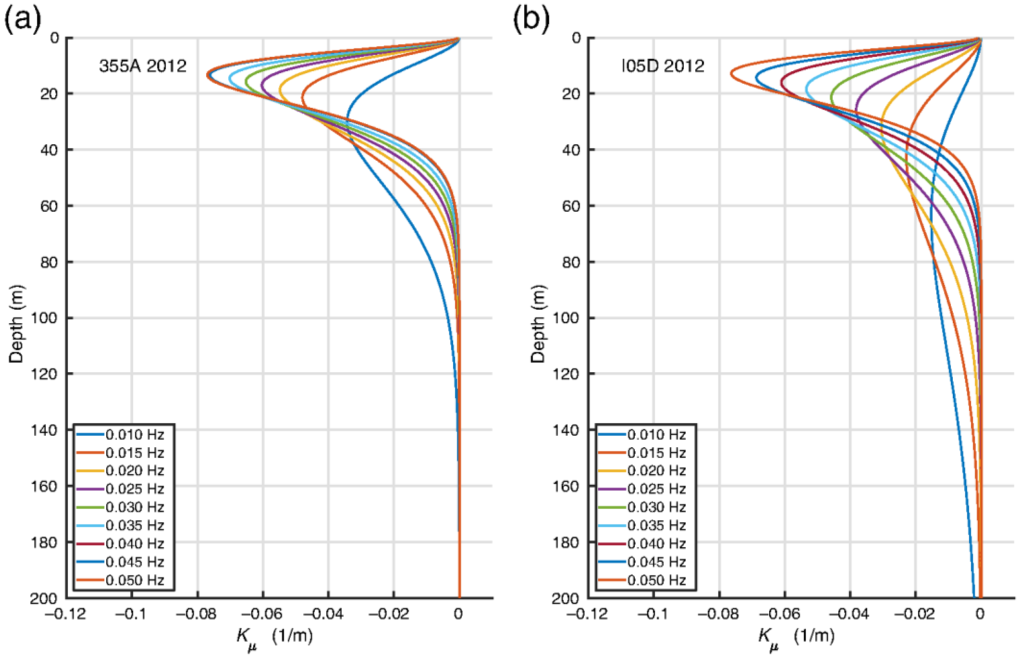

Figure 4. Depth sensitivity kernels of rigidity at two stations, (a) 355A and (b) I05D, at frequencies from 0.01 to 0.05 Hz, with an increment of 0.005 Hz. The color version of this figure is available only in the electronic edition.

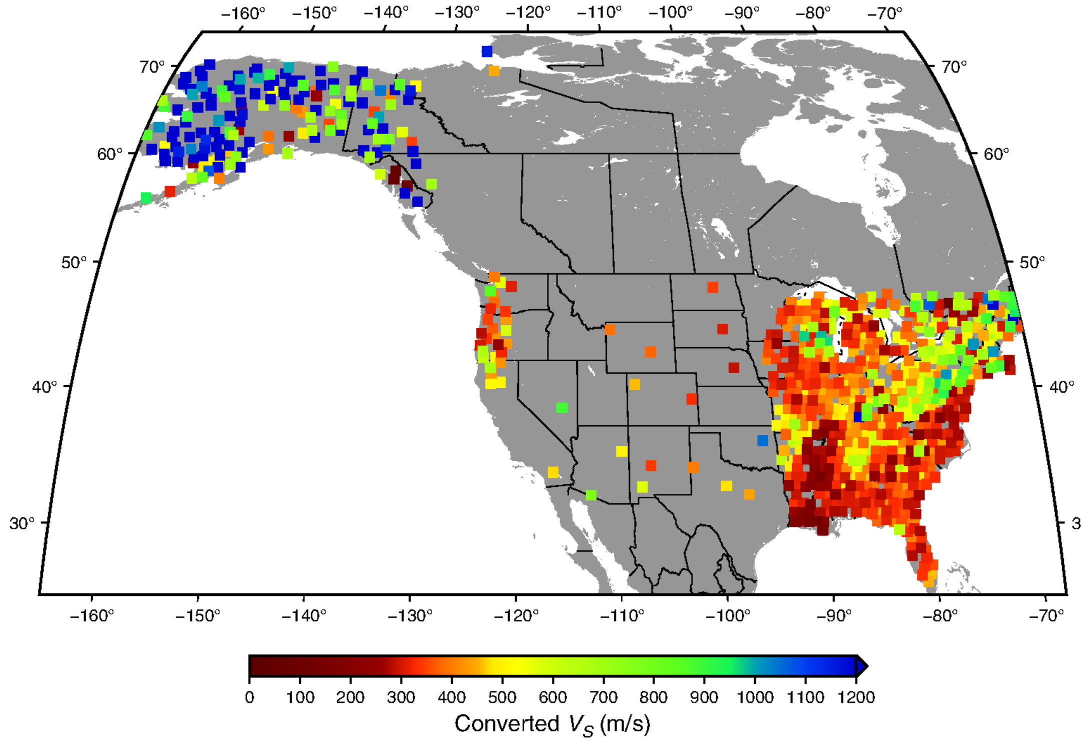

Figure 5. Our results for 784 TA stations. The color bar follows the logic for which fast V_S is blue and slow V_S is red. Stations are colored based on their corresponding V_S . Note that the color saturates at V_S of 1200 m/s, and most stations with V_S higher than 1200 m/s are in Alaska. Each station is located at the center of the square and the size of squares does not mean the whole area underneath the square has the same structure. The color version of this figure is available only in the electronic edition.

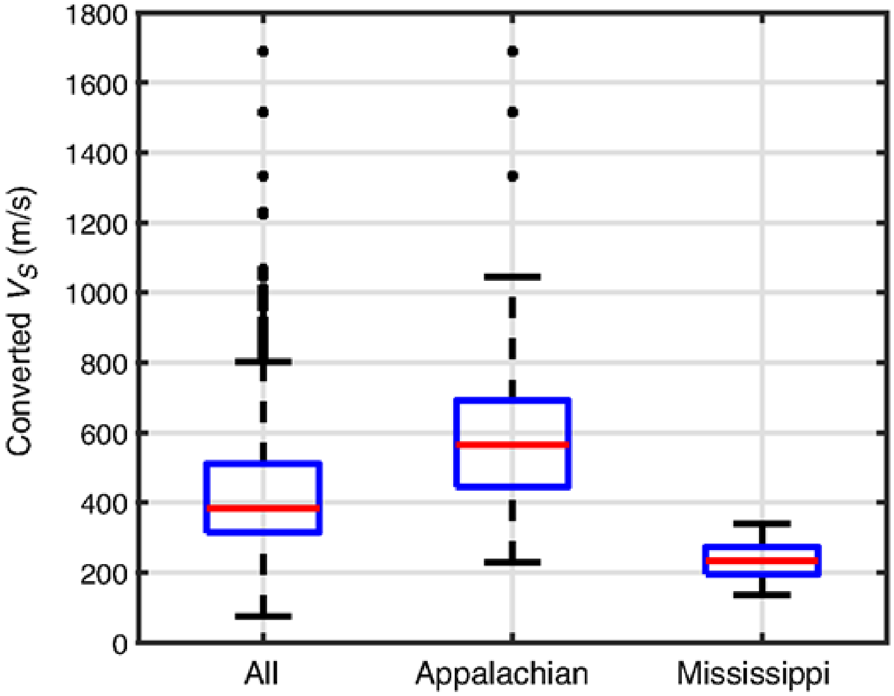

Figure 6. Box plots on results from all stations in the contiguous United States, stations on the Appalachian Mountains, and stations in the Mississippi area. Top and bottom edges of each box represent 75th and 25th percentiles, respectively, of included stations. Red lines in the center of each box are the median values. Whiskers on both ends represent ±2.7σ of included stations, and black dots are “outliers” that are outside of ±2.7σ. The color version of this figure is available only in the electronic edition.

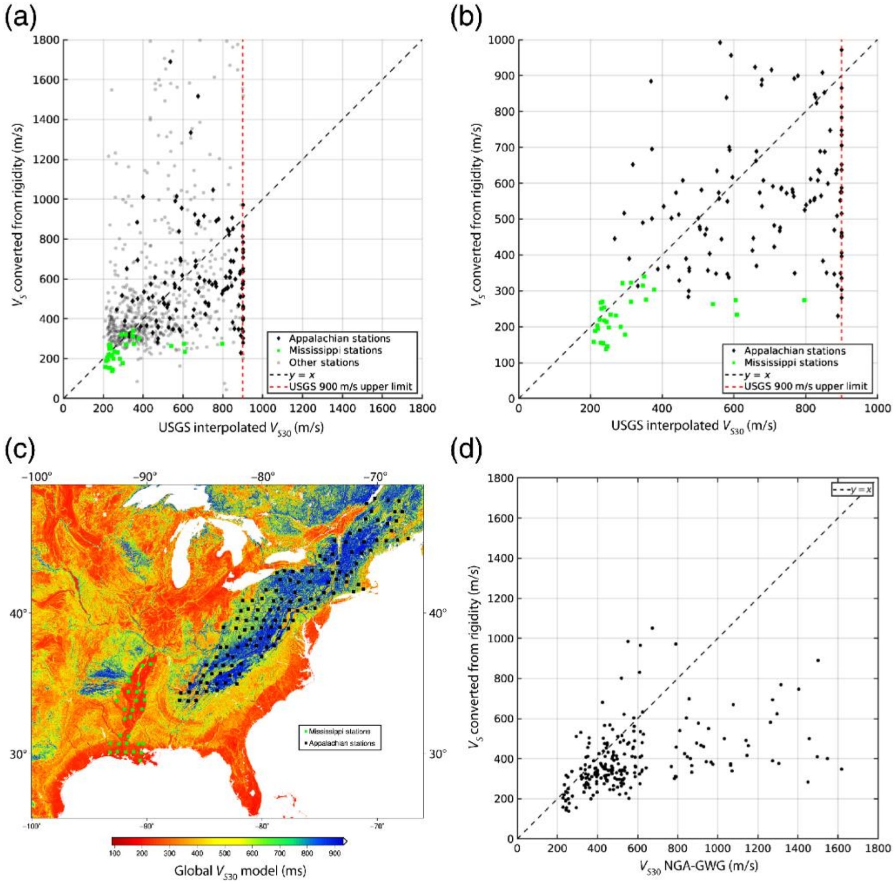

Figure 7. Comparison between the various V_{S30} models and our V_S estimates (converted from $\bar{\mu}$). (a) All stations in the contiguous United States compared with interpolated values from the U.S. Geological Survey (USGS) model. Black diamonds are TA stations in the Appalachian region, green squares are TA stations in the Mississippi Alluvial Plain region, and faded gray circles are all other TA stations. The black dashed line is the one-to-one line, and the vertical red dashed line indicates the upper limit of the USGS VS30 model (900 m/s). (b) The same information as (a) but only showing “Appalachian” and “Mississippi” stations and zoomed in on the 0–1000 m/s interval. (c) Selected “Mississippi” and “Appalachian” station locations superimposed on the USGS (Wald and Allen, 2007) V_{S30} model. (d) “Preferred” V_{S30} values from Goulet et al. (2014) compared with 216 TA stations from our results. The color version of this figure is available only in the electronic edition.

4 Estimation of Vs30 at the EarthScope Transportable Array Stations by Inversion of Low-Frequency Seismic Noise

This chapter is in preparation for publication.

4.1 Abstract

One of the main sources of seismic noise below 0.05 Hz is atmospheric pressure variations, especially when surface pressure variations are large. The amount of ground deformation under surface pressure changes reflects the characteristics of shallow elastic structure. When a surface broadband seismic station is collocated with pressure instruments, we can estimate near-surface shear-modulus structure with a propagating pressure waves assumption. We present the results from vertically heterogeneous layered models. We measure η(f)=Sz/Sp, where f is the frequency band between 0.01 and 0.05 Hz, and Sz and Sp are the power spectral densities of vertical seismic data and of surface pressure data.

We derive depth sensitivity kernels for η(f) from which we invert η(f) for elastic moduli of the shallow structure. Sensitivity kernels typically have peak at a depth that is shallower than the uppermost 50-100 meters. Based on 1-D structures, we estimate Vs30 for 744 USArray Transportable Array stations. We compare our results with various surficial geology maps. Although Vs30 has high horizontal variability over a short distance on the scale of hundreds of meters, we find correlations between Vs30 and larger regional geological structures, such as mapped units and surficial materials. We find good agreement between estimated Vs30 and mapped Quaternary sediment depths, where stations having thicker underlying sediment tend to have faster Vs30.

4.2 Introduction

This interaction between atmospheric pressure variations and the solid Earth at low frequencies can be quantified by analyzing low-frequency seismic data with collocated pressure data, particularly data in the frequency band between 0.01 and 0.05 Hz (e.g., Tanimoto and Wang, 2018). Sorrells (1971) proposed the theoretical framework with a half-space model: the excitation mechanism is wind-related pressure waves that move along the surface and cause ground deformation recorded by broadband seismic sensors. Similar principles are also applicable in ocean-bottom-seismometers compliance studies (Crawford et al, 1991) and in evaluating near-surface structure on Mars (Kenda et al., 2017). These studies share the well-known concept that shallow elastic structure determines the earth's response to applied forces (e.g., Sánchez-Sesma and Crouse, 2015; Trifunac, 2016). More specifically, stations with soft-sedimentary substrates experience larger deformation, while stations with bedrock substrates experience smaller deformation. Expanding on the work of Sorrells (1971), we can use the ratios of collocated seismic and pressure data to estimate the subsurface elastic structure at collocated stations. Better understanding of near-surface structure advances the knowledge of seismic hazards and ground motion prediction studies (e.g., Borcherdt, 1994; Trifunac, 2016). A theory for retrieving half-space structure at fixed frequencies has been demonstrated by Tanimoto and Wang (2018). This has been applied to estimate half-space structure at 784 USArray Transportable Array (hereafter TA) stations (Wang and Tanimoto, 2020).

Although half-space results illustrate near-surface structure in a straightforward manner, it lacks depth constraints that are essential for site effects parameters, such as Vs30. Vs30 is a proxy for the averaged shear-wave velocity from the surface to 30 meters below and is one of the primary quantities for ground motion prediction studies (e.g., Dobry et al, 2000). In order to estimate Vs30 for a layered structure beneath a station, we developed an inversion approach by inverting data between 0.01 and 0.05 Hz (hereafter referred to as "the inversion method") (Tanimoto and Wang, 2019). Near-surface elastic structures estimated from the inversion method have been corroborated by comparing with measured Vs30 (Yong et al, 2013) at collocated stations within the Piñon Flat Observatory (Tanimoto and Wang, 2020).

There are other approaches to infer the near-surface structure. These include invasive field-methods such as drilling and sonic logging, noninvasive field-methods such as Multichannel Analysis of Surface Waves (MASW, Park et al, 1999) with geophone arrays, analysis of the particle motions of body waves (Park and Ishii, 2018), and unique deployments such as fiber-optic distributed acoustic sensing (e.g., Dou et al., 2017). Due to the scarcity of Vs30 profiles around the world, it is also common to infer Vs30 using large-scale proxies such as geology maps and topographic slopes (e.g., Park and Elrick, 1998; Wald and Allen, 2007). Other shallow-structure techniques such as H/V spectral ratios (HVSR, e.g., Nakamura, 1989) and similarly ZH ratios (e.g., Tanimoto and Rivera, 2008) typically resolve structures at depths measured in kilometers, which are not directly applicable for estimating Vs30. These various methods have their own advantages and disadvantages; our inversion method can be a valuable addition to the field of seismic hazard studies.

We use the inversion method to estimate the layered structure and Vs30 at 744 TA stations. Our Vs30 results show good agreements with various large-scale surficial geology maps such as Quaternary sediment depths. We also find high degree of similarity between Vs30 and our previously estimated half-space Vs at 0.02 Hz (Wang and Tanimoto, 2020) after comparing results between the layered model and the half-space model. Although the inversion method provides depth constraint and an ability to estimate Vs30, the half-space approach (Tanimoto and Wang, 2018) is still a valuable approach because it is more straightforward to adopt and much less computationally expensive, while still giving robust estimates of near-surface structure comparable to Vs30 at specific frequencies.

This paper has the following sections. We first present our data with explanations of the quality-control criteria. Secondly, we describe the inversion method, with examples at two TA stations, 355A and I05D, throughout the section. Thirdly, we present Vs30 results at 744 TA stations. Then we compare layered results with previously estimated half-space Vs (Wang and Tanimoto, 2020). Lastly, we discuss future estimation of near-surface structures with low-frequency seismic noise caused by surface pressure variations.

4.3 Data Analysis

4.3.1 Data Preprocessing

Most of our dataset come from the TA stations for which high-quality pressure sensors were added since mid-2011 (Tytell et al., 2016). Broadband seismic stations typically do not have collocated pressure sensors. The lack of collocated seismic and pressure stations is partially the reason for a rather poor quantitative understanding of the land-atmosphere interaction despite theoretical work of Sorrells (1971). With the contribution of hundreds of TA stations, we now have an unprecedented amount of collocated data to study this phenomenon. Here, we analyze data at TA stations from Jan 1 2012 to Jan 1 2019. There are 912 analyzed stations which cover most of the eastern US and Alaska. For each station, we use three surface seismic channels and one infrasound-sensor pressure channel. Each has a sampling rate of 1.0 Hz. All seismic and pressure data are downloaded from the Incorporated Research Institutions for Seismology Data Management Center (IRIS DMC).

Each TA station typically operated for about two years with some backbone stations remaining operational for longer periods. We analyze data for the entire duration of each station. We apply standard processing steps on raw time series to compute hourly power spectral densities (PSDs). The processing steps are similar to, for example McNamara and Buland (2004). For each one-hour time series, we detrend, apply a Hanning window, compute Fourier spectra, and then remove instrument response (for ground velocity) in the frequency domain. Next, we compute PSDs for seismic and pressure data at frequencies from 0.01 to 0.05 Hz at an increment of 0.005 Hz. We compute hourly coherence between each individual seismic component with pressure. Coherence can be used as an effective indicator of time intervals when the ground is directly deforming due to surface pressure changes (Tanimoto and Wang, 2018). When coherence is high and pressure change is large, there exists a robust coupling between the atmospheric pressure and the solid Earth.

For each hour at each station, we obtain PSDs for LHN, LHE, LHZ, LDF and seismic-pressure coherence between three pairs: LHN and LDF, LHE and LDF, LHZ and LDF. For each hour, there are seven quantities estimated at nine discrete frequencies from 0.01 to 0.05 Hz at a frequency interval of 0.005 Hz.

4.3.2 Half-Space Structure

To prepare for the inversion method, we compute pressure-wave speed, c, and half-space modified shear-modulus, $\bar{\mu}$, which are used for the construction of starting models. We start the process with some data-culling steps to exclude time intervals when pressure and seismic data are badly correlated. Specifically, we include hourly horizontal PSDs when coherence between LHN and LDF, LHE and LDF are both higher than 0.7; we include hourly vertical seismic PSDs when coherence between LHZ and LDF, and either correlation of LHN or LHE and LDF is higher than 0.7. We also impose a pressure threshold at 1 Pa^2/Hz, i.e., we only include time intervals when hourly pressure PSDs are higher than 1 Pa^2/Hz. Time intervals with large pressure variations include stronger interaction between the pressure and ground. These coherence and pressure criteria are consistent with our previous practice in Wang and Tanimoto (2020). To better ensure the robustness of our analysis, we apply a 20% trimmed mean method (e.g., Wilcox, 2012) to exclude outliers. By definition, we exclude 20% of both ends of sorted coherent PSDs. The 20% trimmed mean method is shown to be appropriate and effective on excluding significant outliers that could have led to erroneous results (Wang and Tanimoto, 2020).

$$\frac{S_H(f)}{S_P(f)} = \frac{g^2}{4\mu^2\omega^2}\left(\frac{\lambda + 2\mu}{\lambda + \mu}\right)^2 \quad (1)$$

$$\frac{S_z(f)}{S_P(f)} = \frac{c^2}{4\mu^2}\left(\frac{\lambda + 2\mu}{\lambda + \mu}\right)^2 \quad (2)$$

$$\overline{\mu} = \mu \frac{\lambda + \mu}{\lambda + 2\mu} \qquad (3)$$

With coherent PSDs of pressure and seismic data, pressure-wave speed and half-space structure can be calculated following Tanimoto and Wang (2018). On the left-hand side of equations (1) and (2) f is frequency; $S_H(f)$ is PSD of horizontal seismic data, which is the sum of two horizontal seismic PSDs (LHN, LHE); $S_Z(f)$ is PSD of vertical seismic data; $S_P(f)$ is PSD of pressure data. On the right-hand side of equations (1) and (2), g is gravitational acceleration; μ is shear-modulus; ω is angular frequency; λ is Lame's parameter; c is pressure-wave speed at the surface. We introduce an alternative quantity $\overline{\mu}$ in equation (3), which we name "modified shear-modulus".

From equations (1) to (3), we can calculate frequency-dependent pressure-wave speed and modified shear-modulus using hourly PSDs and coherence. These will be used in the inversion method to determine the layered structure from which we can get Vs30.

4.3.3 Quality Control for the Inversion Method

As examples of our analysis, we show results from two stations: 355A and I05D. 355A is a TA station located near Pearson, GA. I05D is a TA station located near Terrebonne, OR. We analyze 21 months of data for 355A and 62 months of data for I05D. Figure 1 is pressure-seismic plots for 355A and I05D. I05D plots have more data points due to its longer duration. As illustrated in Figure 1, if we focus on green points, which are time intervals that pass coherence criterion and pressure threshold, there is clear correlation between pressure PSDs and seismic PSDs. Simply put, larger surface pressure variations lead to larger ground deformation, which is intuitive for the land-atmosphere interaction.

Tables 1 and 2 show summarized results for 355A and I05D. We create a data table for every TA station. We use the information in the table to determine whether a station is a good candidate for the inversion. We construct starting models for the inversion based on pressure-wave speed c and modified shear-modulus $\overline{\mu}$ at discrete frequencies.

"kh" and "kz" fields in Tables 1 and 2 are number of one-hour coherent and high-pressure time intervals for the entire duration of two stations. The remaining columns are computed using equations (1) – (3) with a 20% trimmed mean approach. Standard deviations are estimated from the distribution of coherent data segments (see green points in Figure 1). 355A and I05D both have large kh and kz, as can be seen in Figure 1. However, there are TA stations that have very small kh and kz, which suggest very few time intervals with high seismic-pressure coherence. The lack of coherent time intervals at some stations is potentially related to environmental factors such as local microclimates or unique site conditions, where hard-rock sites may have very little deformation under surface pressure changes (Wang and Tanimoto, 2020).

To ensure the robustness of the inversion, we impose two quality-control steps on all TA stations. First, a station will be included in the analysis only if it has five or more frequencies with both kh and kz larger than ten. With this constraint the number of stations was reduced to 754 from 912. Second, if a station is qualified by the first step, only those frequencies for which kh and kz are greater than ten are included in the inversion. For example, if a station has large kh and kz from 0.01 to 0.04 Hz, but not at 0.045 Hz and 0.05 Hz, we will invert the structure to fit data only from 0.01 to 0.04 Hz. We run the inversion algorithm at 754 qualified stations and eventually obtain stable results at 744 stations.

4.4 *Inversion Method and Examples*

Here we briefly summarize steps in the inversion method to provide context for the rest of the paper. More detailed background theory and derivation can be found in Tanimoto and Wang (2019). In the inversion method, the fundamental idea is to construct a starting model (layered structure) and perturb and update this model to fit data at multiple frequencies from 0.01 to 0.05 Hz, following criterion described in section 2.3. Specifically, we aim to fit surface observable η(f), which we define as the following.

$$\boldsymbol{\eta}(\mathbf{f}) = \frac{\mathbf{S_Z(f)}}{\mathbf{S_P(f)}} \tag{4}$$

η(f) is the ratio between vertical seismic and pressure PSDs at discrete frequencies; it is “ZP_ratio” in Tables 1 and 2. Pressure-wave speed can be estimated using equations (1) and (2), typically of the order of 1-10 m/s, as shown in Tables 1 and 2. Notably, pressure-wave speed is much slower than seismic waves; this leads to it sensitivity at much shallower depths compared to traditional seismic methods at such low frequencies. η(f) is frequency-dependent; fitting of η(f) will provide constraints on the layered model.

Throughout this method section, we present examples of the inversion at TA stations 355A and I05D. Data from these two stations are illustrated in Figure 1; important values are tabulated in Tables 1 and 2.

4.4.1 Inversion Method

We first construct starting models for each TA station by using half-space structure at different frequencies. From sensitivity kernels of shear-modulus, we find a crude empirical relationship between pressure-wave speed and peak-depth of kernels at different frequencies.

$$\mathbf{H}(\mathbf{f}) \cong \frac{\mathbf{0.15} * \boldsymbol{c}(\mathbf{f})}{\mathbf{f}} \qquad (\mathbf{5})$$

where H(f) is the peak depth of the shear-modulus kernel, c(f) is the pressure-wave speed and f is the frequency--typically selected from 0.01 to 0.05 Hz. After obtaining peak depths at each discrete frequency, we align half-space elastic structure to the corresponding peak depths. We interpolate parameters between fixed peak depths from these discrete frequencies. For example, a station with pressure-wave speed of 5 m/s at 0.01 Hz will have its deepest H(f) at 75 meters (equation 5). Then we assign density, Vp and Vs converted from modified shear-modulus at 0.01 Hz to the depth of 75 meters in the starting model. Vs profiles shown as dashed lines in Figure 2 are starting models of 355A and I05D based on information from Tables 1 and 2, respectively.

In practice, the design of a starting model works quite well with structures found by inversion converging to the quantity $\eta(\mathrm{f})$ quickly.

After setting up vertically heterogeneous starting models, we apply the inversion method following Tanimoto and Wang (2019). In the inversion method, we solve the seismic wave equations, specifically P-SV system of equations by numerical differentiation. There are four boundary conditions: pressure variations exerted at the surface, the vanishing of shear stress at the surface, and two finite radiation conditions at the top of the lowermost half-space layer (see equations 14-15 in Tanimoto and Wang, 2019).

In practice, we perturb and update layered models in each iterative step to fit the target quantity $\eta(\mathrm{f})$. Sensitivity kernels (Figure 3) are computed for each updated model and used to solve for perturbations of shear-modulus and bulk modulus. These perturbations are used to update the layered model.

4.4.2 Model Fit and Variance Reduction

With the inversion framework set up in section 4.4.1, we can start the numerical processing. In practice, at each TA station, we iterate the inversion nine times although an optimum model is typically found at earlier steps.

In Figure 4, we illustrate a theoretical $\boldsymbol{\eta}$ computed from each layered model with the starting model as the 0-th iteration. Theoretical $\boldsymbol{\eta}$ is compared with observed $\boldsymbol{\eta}$ listed in Tables 1 and 2. For 355A, the starting model fits the data well, whereas the starting model for I05D fits data less well but still within $\pm 1\sigma$ of the data. At both stations, the inversion converges after one or two iterations after which the models remain relatively constant. The upper frequency limit is 0.05 Hz for 355A and is 0.04 Hz for I05D. For all stations, we perform inversion up to 0.05 Hz and 0.04 Hz; then we visually inspect the goodness of fit for both cases. Typically, data near 0.05 Hz show more scatter and uncertainty, presumably because energy from the ocean waves starts to outweigh the effect of atmospheric pressure (e.g., Tanimoto and Wang, 2018). By examining sensitivity kernels (Figure 3) we note that peak depths for 0.04 and 0.05 Hz are very similar. We surmise that the choice between 0.04 Hz and 0.05 Hz has minor influence on the resulting earth structure.

After nine iterations, we decide which iteration is the final model by determining the improvement of the misfit using variance in equation (5) and variance reduction between the consecutive models.

$$\sigma^2 = \sum_{j=1}^{m} \left(\eta_o^i - \eta_T^i\right)^2 \tag{5}$$

In most cases, the inversion converges after one or two iterations. Although the misfit could be reduced with more iterations, improvements become quite small. Therefore, we select the final model when the normalized variance reduction of the next iterative model is less than 5% of the previous model.

Figure 5 show variance reduction plots for both 355A and I05D. All variance values are normalized to the variance of the starting model. In both cases, there are significant improvements to the misfit after the first iteration. Misfits then stay relatively flat for several more iterations which suggest improvements on the goodness of fit become small. For example, at I05D, the normalized variance in the first iteration is 23.9%, i.e., a variance reduction of 76.1%. Normalized variance at the second iteration is 9.4%, i.e., a variance reduction of 14.5%, still larger than the 5% threshold. Normalized variance at the third iteration is 6.6%, which suggests a variance reduction of only 2.8%, which falls below the 5% threshold. In this example, the final model for I05D is the layered model at the second iteration. While the 5% threshold is rather arbitrary, selecting nearby iterations would give similar results as seen from the convergence in Figure 4.

4.4.3 Uncertainty Constraints

We use two separate approaches to understand results in our layered structures. First, we estimate standard deviations using covariance matrices of data measurements and model parameters, which are common for least-square inversions (e.g., Tarantola, 2005). In essence, we assume each measurement is independent; therefore, the data covariance matrix is a diagonal matrix with data uncertainties on the diagonal. In turn, the diagonal elements of the covariance matrix of model parameters can be used as uncertainties in inverted model parameters. The covariance matrix of model parameters can be calculated using data covariance matrix and data kernel. Once we obtain uncertainties in layered structures of shear-modulus and bulk-modulus, we can estimate uncertainties in layered Vs and Vs30. Vs30 uncertainties are typically around 20-30% of the mean Vs30 estimate. Second, we quantitatively test how perturbations in observed data will map into the inversion results. In practice, we perturb surface observables $\eta(f)$, pressure-wave speed c, and modified shear-modulus $\bar{\boldsymbol{\mu}}$ by adding or subtracting 25%, 50%, 75%, 100% of their respective standard deviations. This produces eight additional scenarios. In the inversion procedure, $\eta(f)$ is the target quantity to be fitted, c and $\bar{\boldsymbol{\mu}}$ determine the starting models for each station. Values in Tables 1 and 2 list these parameters and their standard deviations. We then invert each perturbed dataset and compare their results with Vs30 results of unperturbed data. Differences between estimated Vs30 of unperturbed and perturbed datasets are quite small. Even with the largest perturbation of 100% standard deviations. Changes in final Vs30 are typically less than 10% of estimated Vs30 of unperturbed datasets. Ideally, it is more desirable to explore variations in inverted structures from randomly perturbed data and starting models in a Monte-Carlo type of effort; but this requires much more computational effort. For our purpose of understanding effects of these perturbations on the results, these eight inversions provide a good coverage of the spectrum of results.

4.5 Results

4.5.1 Vs30 at 744 Stations

For all 744 stations, we follow the steps described in sections 2 and 3. We pick time intervals with high coherence and large pressure, construct individual starting models for a half-space at discrete frequencies, invert for layered structures with nine iterative steps, and determine final models by examining variance reduction. From velocity profiles of the final model (e.g., Figure 2), we estimate Vs30 at these TA stations. Vs30 is estimated by averaging shear-wave velocities in the top 30 meters. Vs30 of 355A and I05D are reported in the titles of Figure 2.

Figure 6 illustrates spatial distribution of Vs30 values, and Vs30 values are tabulated in the supplemental file. Despite the lack of accurately measured or inferred velocity profiles at these locations, there are two predominant regions that have distinct Vs30 values among stations in the Eastern US. First, many stations along the Appalachian region have Vs30 faster than 700 m/s. Second, many stations within the Mississippian Alluvial Plain have Vs30 slower than 300 m/s. Similar patterns can be seen in various Vs30 models (e.g., Wald and Allen, 2007; Thompson and Silva, 2013). These two patterns are consistent with local geological settings. Many TA stations in the high-latitude regions such as Alaska and Territory of Yukon are quite unique. Some of these stations have Vs30 higher than the upper limit of the color bar (1200 m/s) and often have high uncertainties in the half-space estimates. There is evidence of significant seasonal changes in the low-frequency seismic noise, which is outside the scope of this paper and can be explored in the future.

In Figure 7, we can inspect distributions of Vs30 in three groups of stations, which include all stations in the contiguous US, stations in the Appalachian and stations in the Mississippi alluvial plain. The first group includes stations in the latter two groups. In the stacked histogram (panel a of Figure 7), Appalachian stations (blue) accumulate at faster Vs30 and Mississippi stations (red) accumulate at slower Vs30. Such distributions confirm the visual patterns observed in Figure 6. In panel (d) of Figure 7, a box plot of the same three groups presents similar information as histograms shown above, where each box encompasses stations in their respective histogram. While distributions of the three groups overlap, the median Vs30 among each group is distinct. All contiguous US stations have a median Vs30 of 360 m/s, Appalachian stations have a faster median Vs30 of 544 m/s and Mississippi stations have a slower median Vs30 of 213 m/s. Information shown in the box plot is consistent with visual patterns seen in Figure 6. Besides these large-scale analyses of our results, we validated results from the inversion by comparing our estimates of Vs30 with measured Vs30 in the Southern California (Tanimoto and Wang, 2020).

4.5.2 Comparison with Geology Maps

In this section, we compare our Vs30 results at 744 stations against two surficial geology maps. One map covers most of the northeast US (Soller and Garrity 2018); it includes sediment depths and overlaps with 215 TA stations. The other covers the conterminous United States (Soller et al, 2009) and includes different interpretations of surficial materials. This map includes 583 TA stations. We also compare our results with the Geologic Map of North America (GMNA, Garrity and Soller, 2009) which is a database of geological units such as rock types and rock ages. When near-surface structure is unknown, large-scale geological information and topographic slopes are commonly incorporated as proxies to infer parameters such as Vs30 (e.g., Park and Elrick, 1998; Wald and Allen, 2007). In Wang and Tanimoto (2020), we quantitatively compared our half-space results with the USGS Global Vs30 Mosaic (Wald and Allen, 2007) which is based on topographic slopes. We found that although large-scale patterns are consistent, station-wise correlation with interpolated Vs30 values from the gridded model is poor. This is expected because large-scale Vs30 models are not appropriate for interpreting local structures. Similarly, correlations with large-scale geology maps will also be limited because it is unrealistic to expect accurate information at a local scale, i.e., at a single station. In this study, we compare with the various geological maps to understand the generality of our results. The goal is to find possible correlations, not to interpret each geology map in-depth.

We group TA stations with defined units on each map by matching stations with polygons on maps. We look at distributions of estimated Vs30 within separate units and interpret them based on three categories of information: sediment depth, surficial material, and geological unit.

We first compare estimated Vs30 at 215 TA stations with Quaternary sediment depths compiled in Soller and Garrity (2018). This covers previously glaciated US east of the Rocky Mountains. In panels (a) through (c) of Figure 8, most groups have overlapping distributions of Vs30. However, in all three categories of surficial sediments (coarse-grained, fine-grained and till), there are large differences between groups with sediment depths of 0-15 meters and 15-30 meters; “coarse-grained” and “fine-grained” sediments are related to wind or water transportations. Intuitively, near-surface structure with coarse-grained sediments, such as sands and gravels, should have faster velocities than fine-grained sediments, such as silt and clay, due to their different material properties and depositional environments where coarse-grained sediments are often deposited on steeper slopes. Such interpretations are used in defining site classes based on measured profiles (Wills et al., 2000); however, this correlation often does not hold when inferring Vs30 using large-scale geological maps. Studies commonly demonstrate that locations defined as “coarse-grained sediments” do not have significantly different Vs30 from locations defined as “fine-grained sediments” (e.g., Park and Elrick, 1998). At a local scale, limited resolution of large-scale geological maps and uncertainties in the sediment depths likely contribute to the lack of correlations (Wills et al, 2015). In our comparisons between these two categories of sediments, median Vs30 of “coarse-grained sediments” are faster than that of “fine-grained sediments” in both “0-15m” and “15-30m” groups. This is consistent with the interpretations above; however, the number of “fine-grained sediment” stations is small, thus less robust. On the other hand, till is the most widespread unit due to the unique geographic setting of this map. Till sediments are deposited from the interaction with previous glaciers in the region. Till sediment generally have faster velocities than typical soils (Thompson and Silva, 2013). Median Vs30s of “till” stations are similar to that of “coarse-grained sediments” stations, which are both faster than median Vs30 of “fine-grained sediments” stations.

All groups with thinnest sediments (0-15 meters) have wider distributions of Vs30, and their median Vs30s are higher than groups with thicker sediments. Wider distributions suggest Vs30s are more variable within areas of thin sediment below the station. This should be expected because stations with minimal underlying sediments will have significantly higher Vs30 than stations with 15 meters of underlying sediment. “Till sediments” groups in panel (c) include the most stations among a total of 215 stations. We observe a large decrease in median Vs30s from “T-S 0-15m” to “T-S 15-30m” and a small decrease from “T-S 15-30m” to “T-S 30-60m”. Distributions of Vs30 between “T-S 30-60m” and “T-S 60-120m” are similar. Generally, stations with thicker underlying sediments should have slower Vs because seismic waves travel with slower speeds in the unconsolidated sediments than in bedrock. Considering Vs30 is an averaged quantity for shear-wave velocities in the shallowest 30 meters, we can expect slower Vs30 in areas with thicker sediment depths. Once sediment depths exceed 30 meters, the presence of deeper sediments should not affect Vs30. Observations are consistent with this general principle. In panel (e), first four boxes are ensembles of three categories mentioned above. Two unique groups in panel (e) are “patchy sediments 0-15m” and “bedrocks or sediments 0-15m”. While these two groups have faster median Vs30 and wider distributions than groups with thick sediments, one would expect much higher Vs30 if bedrock is exposed at or very close to the surface. Distribution of Vs30 at these locations suggest that some unconsolidated sediments likely exist, which could be due to map uncertainties. Panel (d) of Figure 8 shows a direct correlation between Vs30 and sediment depths. Sediment depths are extracted from the raster file provided in Soller and Garrity (2018); this file assigns specific depths at all points. Although there is no distinct correlation, we observe one important pattern similar to three box plots which gives a wide range of Vs30 for stations with thin sediments and for stations with tens of meters of sediments or more: Vs30 is slow. This pattern suggests that fast Vs30 stations are located in places with very thin sediments.

The second comparison is between 583 stations and their mapped surficial material units in Soller et al (2009). This map spans the conterminous US; it overlaps with more stations than the first comparison. It includes only descriptions of different units of surficial materials but not specific thickness of sediments. Figure 9 includes all groups with more than 20 stations. It shows nine groups of stations that are defined by their respective surficial materials. These are sorted by their median Vs30s. Three top groups are all defined by “discontinuous” or “thin” sediments, and three bottom groups are all defined by “Alluvial” or “Coastal zone” sediments. Top two groups are associated with colluvial and glacial till sediments. Colluvial (loess) and glacial till sediments typically have faster velocities than typical soils (Thompson and Silva, 2013). Meanwhile, alluvial and coastal sediments are expected to have slower seismic velocities. Despite the largely overlapping distributions, groupings of different stations (Figure 9) fit our general understanding on the relationship between different types of surficial sediments and near-surface velocities. Although there are no specific sediment depths, surficial material interpretations from Soller et al (2009) agree well with our Vs30 results.

Geological unit IDs are unique identifier numbers assigned to each unit in the GMNA. These IDs are non-repetitive, meaning geological units will have different IDs if they are at different locations even if they have the same geological interpretations of rock types and ages. These numbers are rather arbitrary and are only related to the list of polygons in the shapefile. Therefore, grouping of stations by unit IDs is indicative of their locations and serves as an index to distinct nearby stations. Figure 10 shows ten geological units with most stations contained within. There are two units with distinct distributions, unit 33026 and unit

33786. Unit 33026's distribution of Vs30 is much slower than other units shown in the plot. It is described as a Quaternary sedimentary rock unit. As seen on the onset map, unit 33026 covers much of the Mississippi Alluvium Plain. It is consistent with the spatial features observed in Figure 6.

In contrast, stations within unit 33786 have relatively fast Vs30. Unit 33786 is described as an Upper Devonian sedimentary rock unit; geographically it covers regions east of the Lake Erie and parts of the Appalachians. As shown in Figure 6 and 7, TA stations within the Appalachians have distinctively faster Vs30 than the rest of stations in the contiguous US. In the GMNA, geological units within the Appalachians are very complex and diverse; therefore, most individual units only contain five or fewer TA stations and are not shown in Figure 10. For instance, unit 33798 is an Ordovician sedimentary rock unit within the Appalachians, right next to unit 33786, as highlighted on the map. It is a much smaller unit; there are four TA stations within the unit. Three stations have Vs30 greater than 825 m/s and the other has Vs30 of 571 m/s. The distribution of Vs30 for unit 33798 is much faster than all units shown in Figure 10; however, due to the small number of stations, such an individual unit cannot be presented with much confidence. On the other hand, unit 33786 is a relatively large geological unit in the Appalachians. It contains enough stations to be statistically significant; stations within it have faster Vs30 compared to other units in Figure 10.

Units 106, 139 and 242 are worth noting in terms of their compact distributions and very short whiskers on both sides. Their compact distributions suggest stations within these units have very similar Vs30 results. Ideally, nearby stations within the same geological units should have similar subsurface layers, and stations with similar subsurface layers should share similar Vs30. These three geological units fit this ideal assumption; however, high spatial variability of Vs30 cannot be overlooked and complicates the situation making on-site estimates of Vs30 very important.

Surficial geological setting in Alaska is unique due to its geographic setting. In Figure 11, we focus on Alaska; we overlay the map with sedimentary basins defined in Coleman and Cahan (2012). One unique feature in Alaska is permafrost. Outside of glaciers, permafrost distribution roughly correlates with latitude where higher latitude regions tend to have more continuous and widespread permafrost (Jorgenson et al, 2008). Our Vs30 results do not correlate with latitude changes (Figure 11), but some high Vs30 stations can still be associated with nearby frozen layers. Although there are no distinctive correlations with sedimentary basins, we notice that many stations with low Vs30 (stations in dark red on the map) are typically near boundaries of sedimentary basins, e.g., the Minchumina Basin and the Nenana Basin in the middle of the map, and the Bristol Bay Basin near the Aleutian Arc in the bottom left. Stations with low Vs can be associated with sedimentary basins (e.g., Berg et al, 2020), but the typical resolved depth for Vs is kilometers, much deeper than the depth for Vs30. Although the spatial alignment of slow Vs30 stations and sedimentary basins could be promising, the roughness of comparison and small number of stations need to be taken into consideration when making such a connection.

In general, one cannot associate large-scale geological features with near-surface elastic structures at a local scale. Large-scale maps are not built for resolving local features, and near-surface structures are highly variable over a short distance both horizontally and vertically. Although comparisons with large-scale geological units are not ideal and cannot be truly indicative of the local information, we use such comparisons due to the lack of other precise on-site measurements. In particular, comparisons with surficial sediment maps show promising trends that fit one's intuitive relationship between sediment depths and Vs30.

4.5.3 Comparison with Half-Space Results

In our previous study (Wang and Tanimoto, 2020), we estimated half-space shear-modulus and Vs at 0.02 Hz using the same dataset. In that study, we analyzed data yearly to better examine temporal variation. Although half-space results cannot be used to provide Vs30 values, distributions of peak kernel depths (Figure 3) at various frequencies suggest that half-space results can provide insights on near-surface structures. Half-space results should be correlated with Vs30 estimates with various gradients.

Figure 12 show scatter plots between estimated Vs30 and half-space Vs calculated using equations (1) and (2). Data from 0.01 to 0.02 Hz are generally more sensitive to deeper structure. If we assume layers at greater depths tend to have faster Vs, half-space results from 0.01 to 0.02 Hz should provide faster Vs than Vs from higher frequencies. We can confirm this trend by looking at distributions in Figure 12. Half-space Vs at lower frequencies (three top panels) tend to be faster than Vs30, whereas half-space Vs at higher frequencies (three bottom panels) tend to be slower than Vs30.

One important pattern illustrated in Figure 12 is the correlation between half-space results and Vs30 from inversion. This correlation is not surprising for two reasons: first, the two methods are closely related. The inversion aims to fit data at discrete frequencies for which the data are proportional to half-space elastic parameters. Second, the half-space Vs can be similar to the Vs found in the near-surface layers. Although near-surface structure information obtained from the inversion is preferred due to its ability to provide depth-dependent elastic parameters, the strong correlation seen in Figure 12 shows that the half-space approach provides a first order estimate of Vs in the uppermost layers. Two advantages of the half-space approach are it is straightforward to adopt and computationally cheaper.

4.5.4 Frequency Range

While we observe high coherence between seismic and pressure data at 0.05 Hz (Tanimoto and Wang, 2018), there is a greater uncertainty. Therefore, in our inversion we consider two scenarios at every station — set the maximum frequency at either 0.04 Hz or 0.05 Hz. In our final analysis, we select the upper limit at each station by examining inverted models and fits to the data.

In Figure 13, we observe highly correlated Vs30 for the two frequency ranges which suggests inclusion of data from 0.04 to 0.05 Hz has very little effect on the Vs30 estimates. As shown in Figure 3, peak depths of kernels at 0.045 Hz and 0.05 Hz for 355A are very close to the peak depth of the kernel at 0.04 Hz. Although kernels vary among stations, this pattern generally holds for many stations implying that data between 0.04 and 0.05 Hz provide depth constraints similar to that of 0.04 Hz.

As an extension of discussion on the upper frequency limit of inversion, we compile distributions of peak depths of shear-modulus sensitivity kernels at all stations. For example, peak depths of 355A and I05D are illustrated as horizontal dashed lines in Figure 3. Figure 14 illustrates the ensemble of peak depths at discrete frequencies between 0.01 and 0.05 Hz.

The striking feature is that the median of the distribution of peak depths is nearly constant for frequencies greater than 0.03 Hz. This suggests that the depth resolution of frequencies ranging from 0.03 to 0.05 Hz are quite similar. This observation is consistent with the correlation shown in Figure 13.

In short, if data between 0.04 and 0.05 Hz show high uncertainty, we can still confidently estimate layered structure by including data only between 0.01 to 0.04 Hz; However, for each individual station, it is still more complete to use the entire frequency range from 0.01 to 0.05 Hz if the data quality is good.

One caveat about peak depths of sensitivity kernels is that kernels are closely related to pressure-wave speed, c, as reflected in equation (5). Pressure-wave speeds are the speed of propagating pressure waves at the surface. They are estimated following half-space formulations (Tanimoto and Wang, 2018), and are typically within 1-10 m/s. Peak depths of the sensitivity kernels are first determined based on the empirical relationships with the pressure-wave speeds and frequencies. At a station, if the pressure-wave speeds are particularly fast or slow, the peak depths of kernels at this station will be very different from other stations; therefore, we focus the discussion on the general distributions of peak depths across frequencies, instead of focusing on individual stations. Despite the dependency on pressure-wave speeds, distribution patterns of peak depths shown in Figure 14 illustrate the trend in the depth resolution in our results. Namely, the resolved structures become shallower for frequencies from 0.01 to 0.03 Hz and remain relatively constant at a fixed depth from 0.03 to 0.05 Hz.

Figure 14 reveals two limitations of the inversion method. First, our inverted structure profiles are much smoother compared to other higher-frequency or dense-array methods. Our velocity profiles cannot recover rapid velocity changes. This is evident in the velocity profiles in Figure 2. Because of the narrow frequency range of our study, the depth resolution is limited. On the other hand, because we aim to estimate Vs30, which is an averaged quantity for the upper 30 meters, the inversion method is still reasonable. Comparison with on-site measured Vs30 in Tanimoto and Wang (2020) supports such a claim. Second, even with the highest frequency limit of 0.05 Hz, we cannot resolve the uppermost layer if it is shallower than 5-10 meters. In Figure 14, the minimum median peak depths of shear-modulus kernels are still deeper than 10 meters. This suggests we typically lack sensitivity for structures shallower than 10 meters. Uppermost velocity profiles of 355A and I05D (Figure 2) show faster Vs at 0-10 meters than Vs at 10-20 meters due to the lack of resolution in uppermost 10 meters. The uppermost velocities are essentially aligned with half-space parameters at the highest frequency in the starting models and are not affected by the iterative process. To construct more accurate velocity profiles, we either extend to higher frequencies or combine with a different approach.

4.6 Discussion

In this study, we applied the inversion method (Tanimoto and Wang, 2019) to all available USArray TA stations operating between Jan 1, 2012 and Jan 1, 2019. We estimated near-surface elastic parameters for a layered structure and Vs30 at these stations. We compared our Vs30 results with various surficial geological maps. There are promising agreements between Vs30 and Quaternary sediment depths. We examine the nature of the inversion method by comparing with half-space results and observing peak depths of sensitivity kernels across frequencies.

We find good correlation between Vs30 and half-space Vs at discrete frequencies between 0.01 and 0.05 Hz. While the inversion method should be used to retrieve important parameters such as Vs30, the half-space approach is much easier to implement and much faster to compute. The half space Vs values are comparable with Vs30 estimated with the inversion method. The half-space approach can still be used as a quick metric to determine key information regarding the near-surface structure.

Analysis and examination of peak depths of sensitivity kernels at various frequencies reveal two limitations of the inversion method. First, our estimated velocity profiles are much smoother than those found by more conventional high-frequency approaches (e.g., MASW). The limitation is partially resolved because Vs30 is an averaged quantity; the lack of sharp velocity is not critical. Second, the inversion method currently cannot resolve structure shallower than 5 or 10 meters given the upper limit 0.05 Hz. This limitation could potentially introduce errors in our estimations of Vs30 if there are significantly different materials within the uppermost 10 m. We can resolve this limitation by extending our analysis to higher frequencies or by adding new constraints and information to our velocity models.

In conclusion, we estimate Vs30 at 744 TA stations following the inversion method (Tanimoto and Wang, 2019). Vs30 is the averaged shear-wave velocity down to 30 meters depth; it is one of the most important parameters for seismic hazard studies (e.g., Dobry et al, 2000). On a map of the US, two groups of TA stations stand out. Stations in the

Appalachian region tend to have faster Vs30; stations in the Mississippi Alluvial Plain tend to have slower Vs30. These two patterns are consistent with large-scale geological settings and are corroborated by the GMNA (Garrity and Soller, 2009). There are also good agreements between our estimated Vs30 and Quaternary sediment depths in surficial geology maps (Soller et al, 2009; Soller and Garrity, 2018), where stations with thicker underlying sediments tend to have slower Vs30; stations with thin underlying sediments tend to have wider distributions of Vs30. Different distributions of Vs30 on different categories of surficial materials also agree with the general understanding between seismic velocity and sediment types. Stations with slow Vs30 in Alaska are typically close to mapped sedimentary basins (Coleman and Cahan, 2012). Although there are no available measured velocity profiles to compare with the TA stations, we previously validated our single-station approach by comparing with measured velocity profile in the Piñon Flat Observatory (Tanimoto and Wang, 2020). We support the more straightforward half-space approach because it correlates well with Vs30 found in the layered structure. The inversion method is still preferred due to its ability to provide depth constraints and to construct layered models.

4.7 Reference

Berg, E. M., Lin, F.-C., Allam, A., Schulte-Pelkum, V., Ward, K. M., and Shen, W. (2020). Shear velocity model of Alaska via joint inversion of Rayleigh wave ellipticity, phase velocities, and receiver functions across the Alaska transportable Array, *Journal of Geophysical Research*, 125(2), doi:10.1029/2019JB018582.

Borcherdt, R. D (1994). Estimates of Site-Dependent Response Spectra for Design (Methodology and Justification). *Earthquake Spectra*, *10*(4), 617–653, doi: 10.1193/1.1585791.

Coleman, J.L., and S.M. Cahan (2012). Preliminary catalog of the sedimentary basins of the United States (*Open-File Rept.*): U.S. Geol. Survey. 2012-1111, doi: 10.3133/ofr20121111.

Crawford, W. C., Webb, S. C., and Hildebrand, J. A. (1991). Seafloor compliance observed by long-period pressure and displacement measurements. *Journal of Geophysical Research*, *96*(B10), 16,151–16,160.

Dobry, R., Borcherdt, R. D., Crouse, C. B., Idriss, I. M., Joyner, W. B., Martin, G. R., Power, M. S., Rinne, E. E., and Seed, R. B (2000). New Site Coefficients and Site Classification System Used in Recent Building Seismic Code Provisions. *Earthquake Spectra*, *16*(1), 41–67, doi: 10.1193/1.1586082.

Dou, S., Lindsey, N., Wagner, A.M. et al. Distributed Acoustic Sensing for Seismic Monitoring of The Near Surface: A Traffic-Noise Interferometry Case Study. *Sci Rep* 7, 11620 (2017), doi: 10.1038/s41598-017-11986-4.

Garrity, C.P., and Soller, D.R. (2009), Database of the Geologic Map of North America: Adapted from the Map by J.C. Reed, Jr. and others (2005): *U.S. Geological Survey Data Series 424*, doi: 10.3133/ds424.

Jorgenson, M.T., Yoshikawa, K., Kanevskiy, M., Shur, Y., Romanovsky, V.E., Marchenko, S., Grosse, G., Brown, J., Jones, B., (2008). Permafrost Characteristics of Alaska + Map, *Proceedings of the 9th International Conference on Permafrost. University of Alaska Fairbanks, Fairbanks, AK*, https://www.epa.gov/sites/production/files/2017-09/documents/ak-state_attachment_2017-06-19.pdf.

Kenda, B., Lognonne, P., Spiga, A., Kawamura, T., Kedar, S., Banerdt, W. B., et al. (2017). Modeling of ground deformation and shallow surface waves generated by Martian dust devils and perspectives for near-surface structure inversion. *Space Science Reviews, 211*, 501–524, doi:10.1007/s11214-017-0378-0.

McNamara, D. E., and R. P. Buland (2004). Ambient noise levels in the continental United States, *Bulletin of the Seismological Society of America*. 94, no. 4, 1517–1527, doi: 10.1785/012003001.

Nakamura, Y. (1989) A method for dynamic characteristics estimation of subsurface using microtremor on the ground surface. *Quarterly Report of Railway Technical Research*, 30, 25-33.

Park, S and Elrick. S (1998), Predictions of shear-wave velocities in southern California using surface geology. *Bulletin of the Seismological Society of America*, 88 (3): 677–685.

Park, B. C, Miller, D. R, and Xia. J (1999). Multichannel analysis of surface waves. *Geophysics*, 64(3), 659-992. doi:10.1190/1.1444590.

Park, S., and M. Ishii (2018) Near-surface compressional and shear wave speeds constrained by body-wave polarization analysis, *Geophysical Journal International*, 213(3), 1559-1571, doi:10.1093/gji/ggy072.

Sánchez-Sesma, F. J., and Crouse, C. B. (2015), Effects of site geology on seismic ground motion: early history. *Earthquake Engineering Structural Dynamics*, *44*, 1099–1113, doi: 10.1002/eqe.2503.

Soller, D.R., Reheis, M.C., Garrity, C.P., and Van Sistine, D.R. (2012), Map Database for Surficial Materials in the Conterminous United States: *U.S. Geological Survey Data Series 425*, doi: 10.3133/ds425.

Soller, D.R., and Garrity, C.P., (2018), Quaternary sediment thickness and bedrock topography of the glaciated United States east of the Rocky Mountains: *U.S. Geological Survey Scientific Investigations Map 3392*, doi: 10.3133/sim3392.

Sorrells, G. G. (1971). A preliminary investigation into the relationship between long-period seismic noise and local fluctuations in the atmospheric pressure field, *Geophysical Journal International*. 26, nos. 1/4, 71–82, doi: 10.1111/j.1365-246X.1971.tb03383.x.

Tanimoto, T., and L. Rivera (2008) The ZH ratio method for long-period seismic data: sensitivity kernels and observational techniques, *Geophysical Journal International*, 172(1), 187-198, doi: 10.1111/j.1365-246X.2007.03609.x.

Tanimoto, T., and J. Wang (2018). Low-frequency seismic noise characteristics from the analysis of co-located seismic and pressure data, *Journal of Geophysical Research: Solid Earth*. 123, no. 7, 5853–5885, doi: 10.1029/2018JB015519.

Tanimoto, T., and J. Wang (2019). Theory for deriving shallow elasticity structure from colocated seismic and pressure data, *Journal of Geophysical Research: Solid Earth*. 124, no. 6, 5811–5835, doi: 10.1029/2018JB017132.

Tanimoto, T., and J. Wang (2020) Shallow elasticity structure from colocated pressure and seismic stations in the Piñon Flat Observatory and estimation of Vs30, *Geophysical Journal International*, 222(1), 678–696, doi:10.1093/gji/ggaa195.

Tarantola, A. (2005). Inverse Problem Theory and Methods for Model Parameter Estimation, Statistical Modeling and Decision Science, *SIAM*, doi: 10.1137/1.9780898717921.

Thompson, E and W. Silva. (2013). Empirical Assessment of Site Amplification and Development of NEHRP Factors for CEUS: Collaborative Research with Pacific Engineering and Tufts University (*Final Technical Rept.*): U.S. Geol. Survey, https://earthquake.usgs.gov/cfusion/external_grants/reports/G12AP20004.pdf.

Trifunac, M. D (2016). Site conditions and earthquake ground motion - A review. *Soil Dynamics and Earthquake Engineering, 90*, 88-100, doi: 10.1016/j.soildyn.2016.08.003.

Tytell, J., F. Vernon, M. Hedlin, C. de Groot Hedlin, J. Reyes, B. Busby, K. Hafner, and J. Eakins (2016). The USArray transportable array as a platform for weather observation and research, *Bulletin of the American Meteorological Society*. 97, 603–619, doi: 10.1175/BAMS-D-14- 00204.1.

Wald, D., and T. Allen (2007). Topographic slope as a proxy for seismic site conditions and amplification, *Bulletin of the Seismological Society of America*. 97, no. 5, 1379–1395, doi: 10.1785/0120060267.

Wang, J., and T. Tanimoto (2020). Estimating Near-Surface Rigidity from Low-Frequency Noise Using Collocated Pressure and Horizontal Seismic Data. *Bulletin of the Seismological Society of America,* 110 (4): 1960–1970, doi: 10.1785/0120200098.

Wilcox, R. (2012). Estimating measures of location and scale, Chapter 3, in *Introduction to Robust Estimation and Hypothesis Testing*, Third Ed., R. Wilcox, Statistical Modeling and Decision Science, Academic Press, Boston, Massachusetts, 43–101.

Wills, C.J., M. Petersen, W. A. Bryant, M. Reichle, G. J. Saucedo, S. Tan, G. Taylor, J. Treiman (2000) A Site-Conditions Map for California Based on Geology and Shear-Wave Velocity. *Bulletin of the Seismological Society of America*, 90 (6B): S187–S208, doi: 10.1785/0120000503

Will, C.J., C. I. Gutierrez, F. G. Perez, D. M. Branum (2015) A Next Generation VS_{30} Map for California Based on Geology and Topography. *Bulletin of the Seismological Society of America*, 105 (6): 3083–3091. doi: 10.1785/0120150105

Yong, A., Martin, A., Stokoe, K., Diehl, J (2013). ARRA-Funded V_{S30} Measurements Using Multi-Technique Approach at Strong-Motion Stations in California and Central-Eastern United States (*Open-File Rept.*): U.S. Geol. Survey. 2013-1102, 60, http://pubs.usgs.gov/of/2013/1102/.

4.8 Figures and Tables

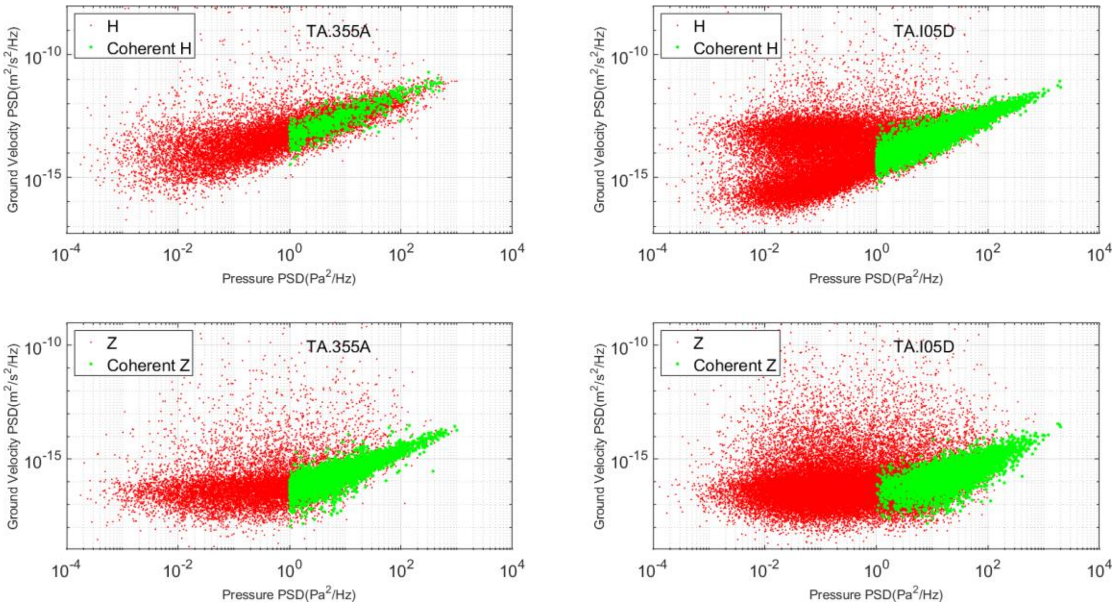

Figure 1. PSD plots of ground velocity vs pressure at 0.02 Hz for TA stations, 355A and I05D. Top panels show horizontal components; bottom panels show vertical components. Each point is an hourly PSD. Time intervals that are coherent with high pressure PSD are highlighted in green.

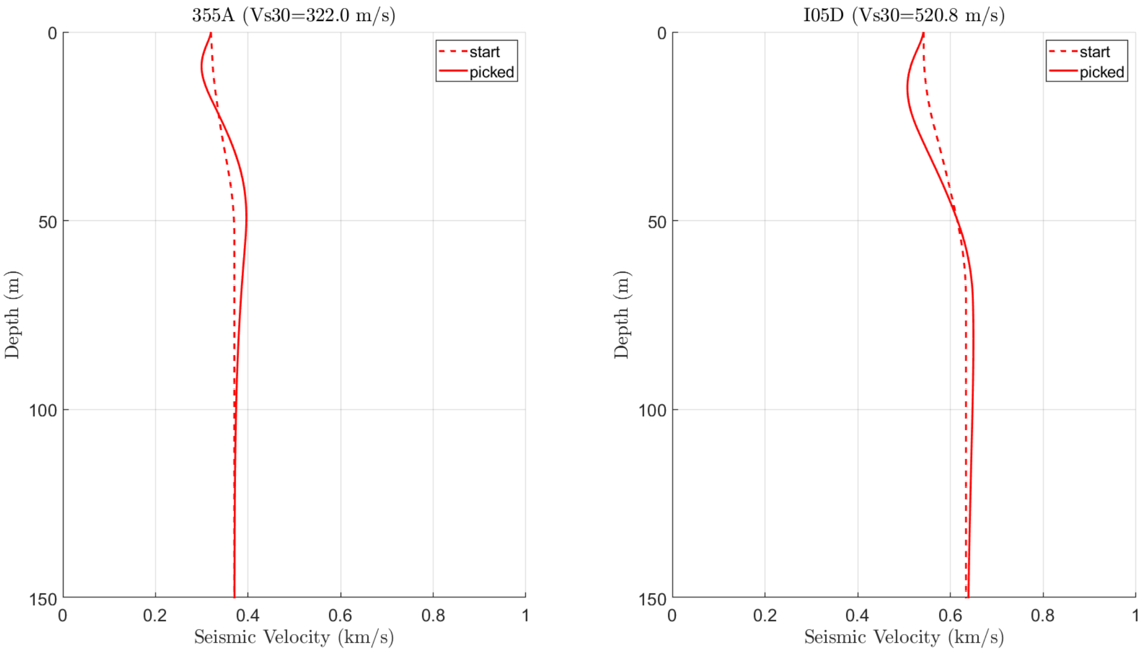

Figure 2. Starting and final Vs models at 355A and I05D

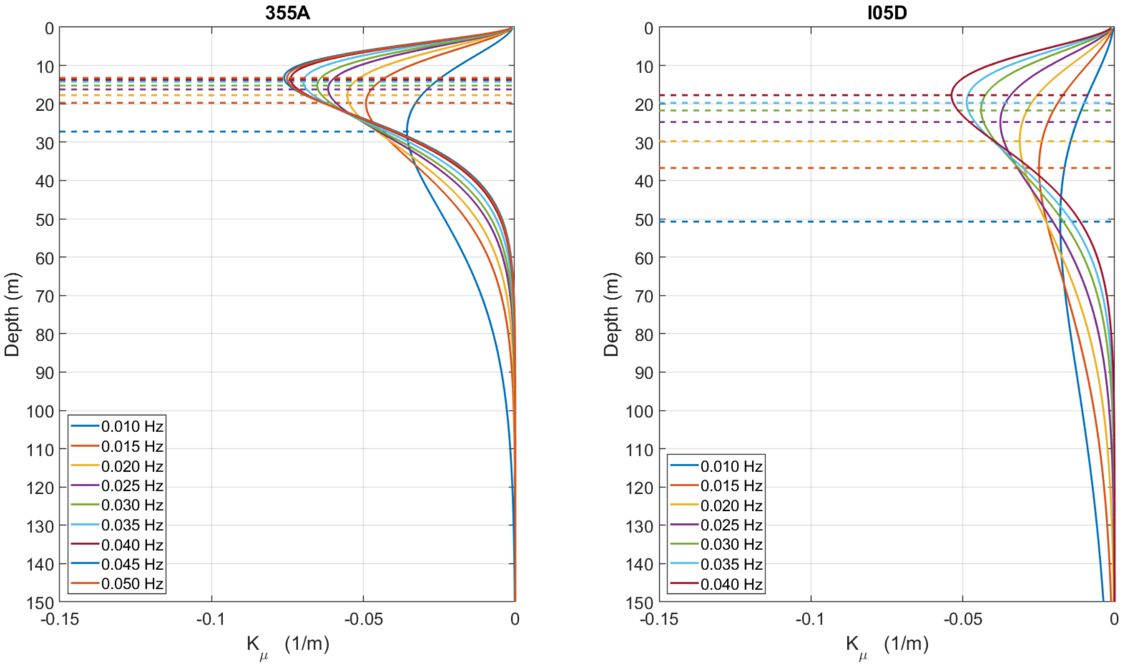

Figure 3. Sensitivity kernels of shear-modulus. Dashed lines demonstrate peak depths at all frequencies.

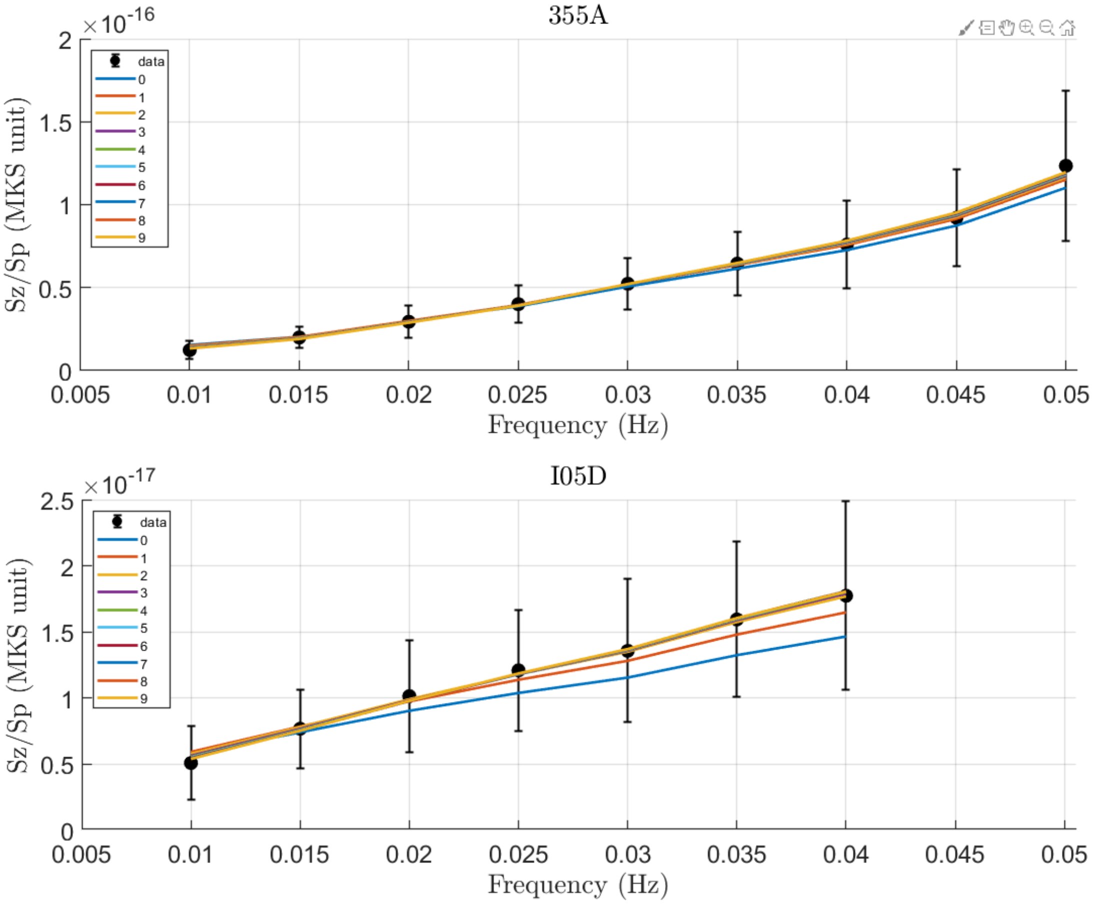

Figure 4. Nine inversion iterations and model fit at 355A and I05D. Data are observed **η** with error bar as ±1σ. Nine lines are theoretical **η** computed from layered models at each iteration.

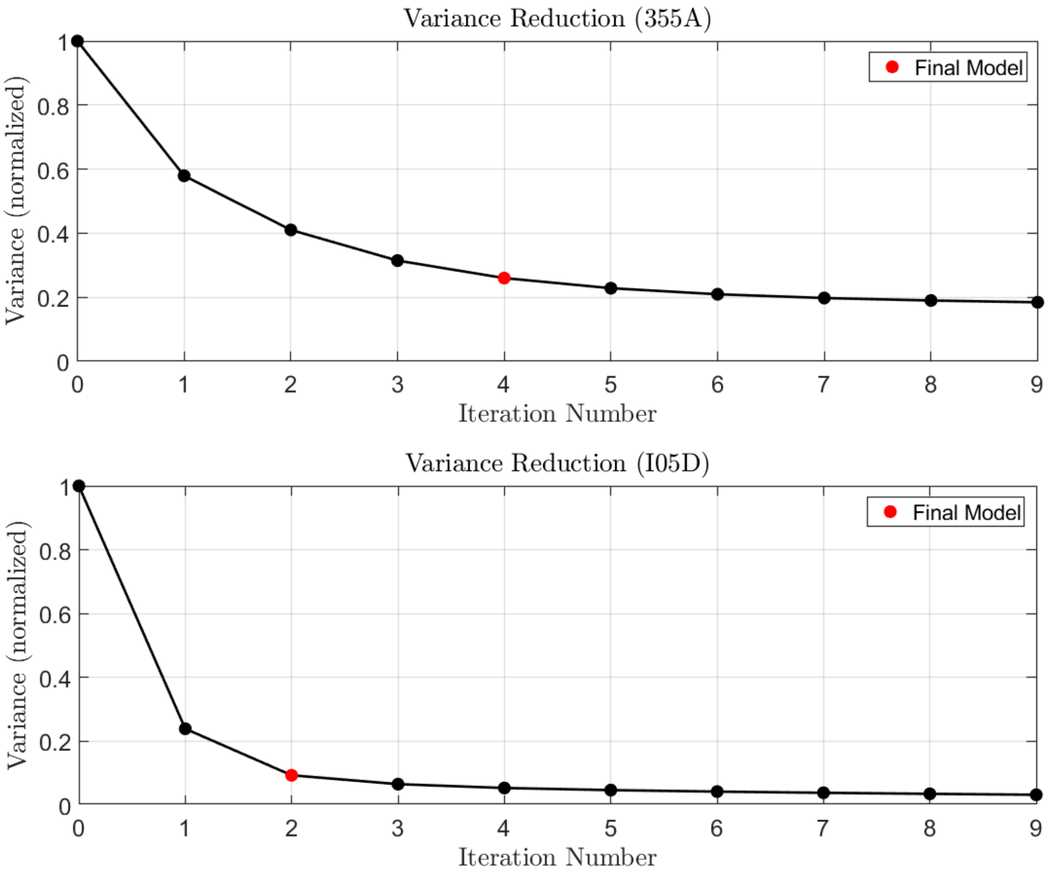

Figure 5. Variance reduction at 355A and I05D. Red points are the final models.

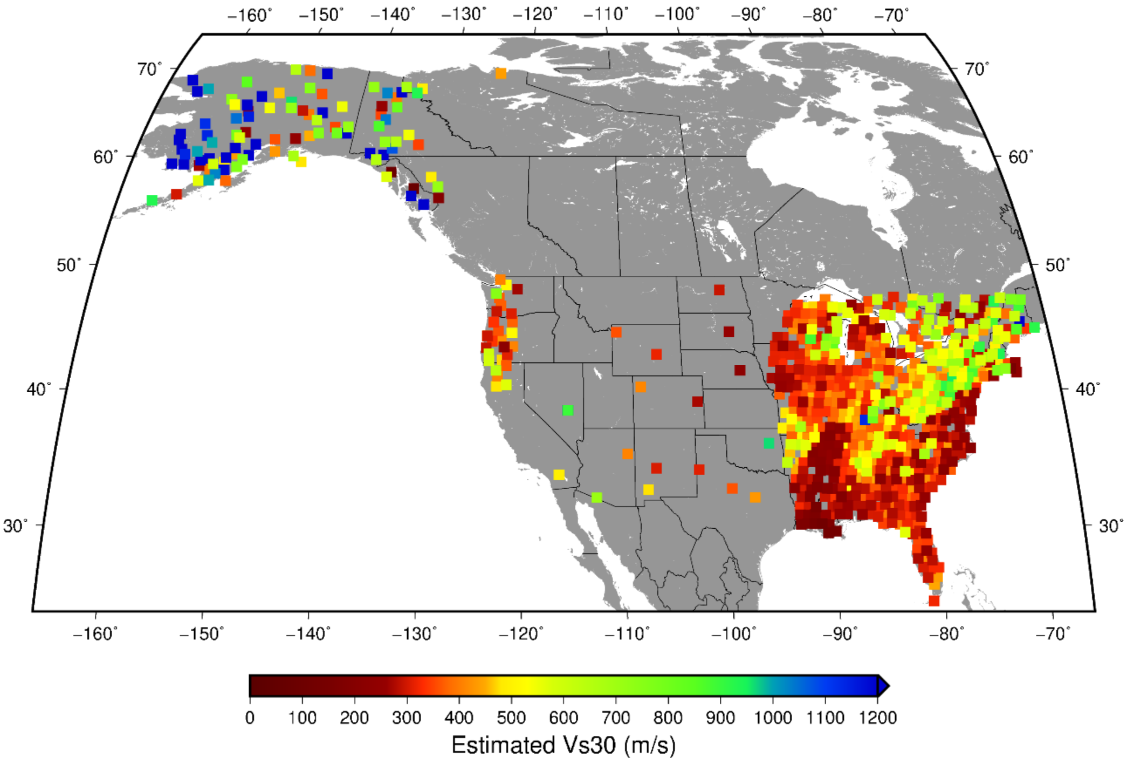

Figure 6. Vs30 results at 744 TA stations. Note that color bar saturates at 1200 m/s. Each station is located at the center of each square.

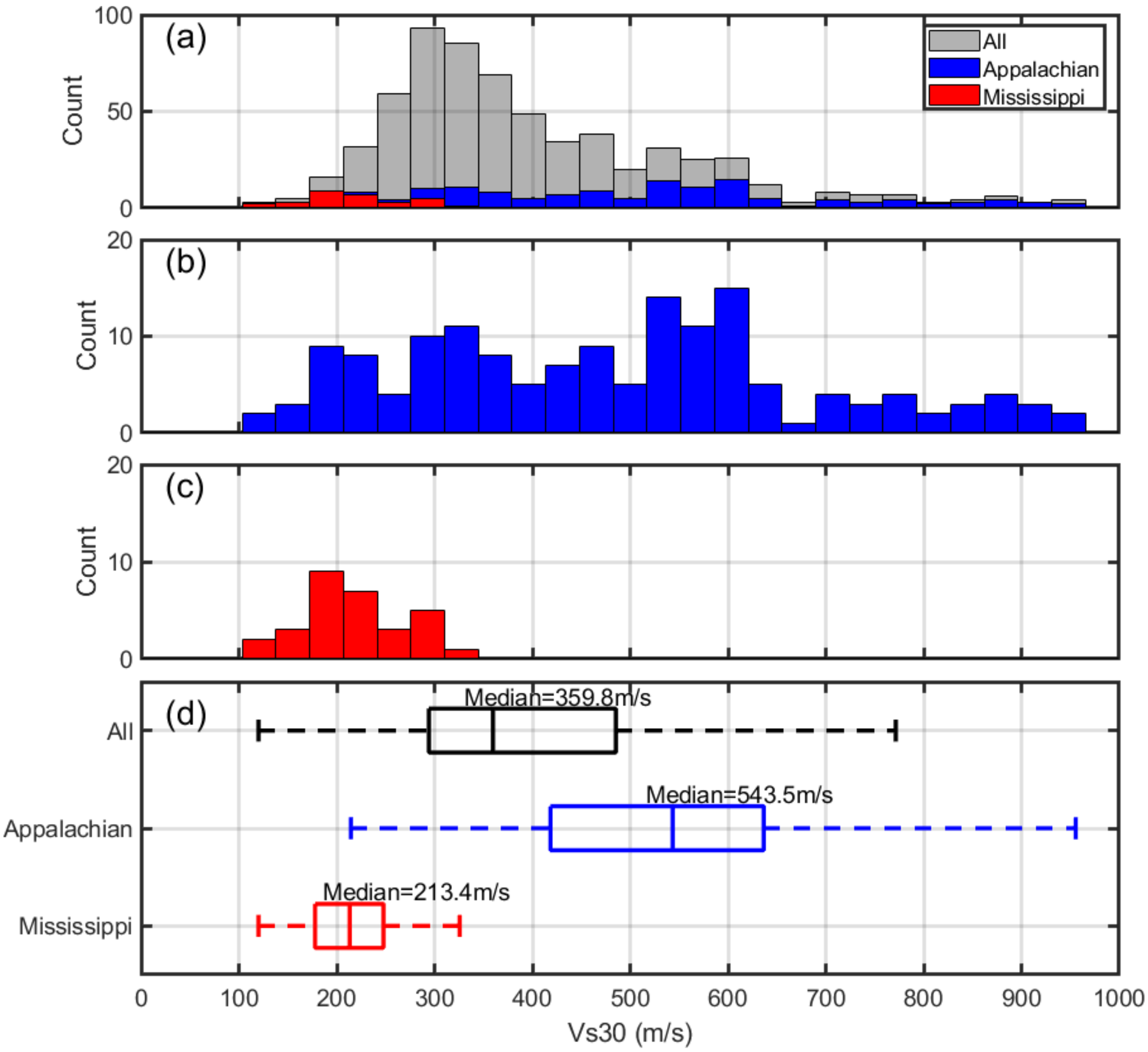

Figure 7. (a): Stacked histogram among three groups: all stations in the contiguous US, Appalachian stations and Mississippian stations. "All" stations include the latter two groups. (b): Histogram for all "Appalachian" stations. (c): Histogram for all "Mississippi" stations. (d): Box plot for three groups the same as the top panel. Vertical line within each box is the median Vs30 of that group. Boundaries of each box represent 25th and 75th percentile of that group. Whiskers extending to each side represent ±2.7σ of that group. Outliers outside of whiskers are omitted, but observable in the top panel.

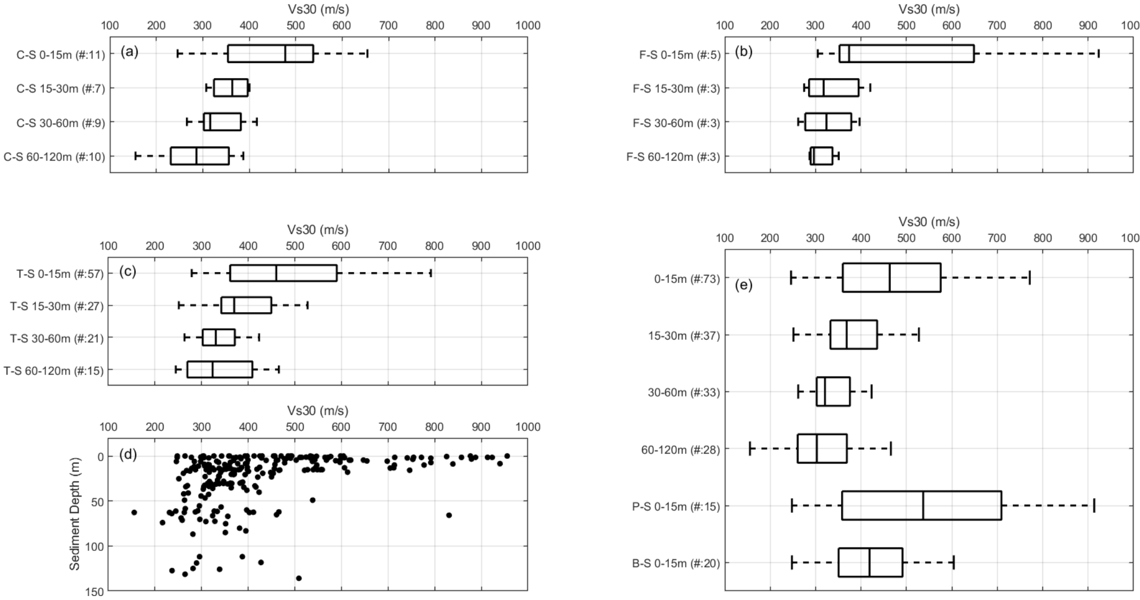

Figure 8. (a)-(c). Box plots of estimated Vs30 (x-axis) with respect to their Quaternary sediment depths. Vertical line within each box is the median Vs30 of that group. Boundaries of each box represent 25th and 75th percentile of that group. Whiskers extending to each side represent ±2.7σ of that group. (a). “C-S” stands for “coarse-grained sediments” and followed by their depths in meters. Numbers in the bracket are counts of stations within the unit. (b). “F-S” stands for “fine-grained sediments”. (c). “T-S” stands for “till sediments”. (d). Scatter plot between estimated Vs30 and sediment depths. (e). Box plot of Vs30 with three categories combined at different sediment depths. Top four boxes include all stations from (a) to (c). Bottom two boxes are two unique units. “P-S” stands for “Patchy Sediments”. “B-S” stands for “Bedrocks or Sediments”.

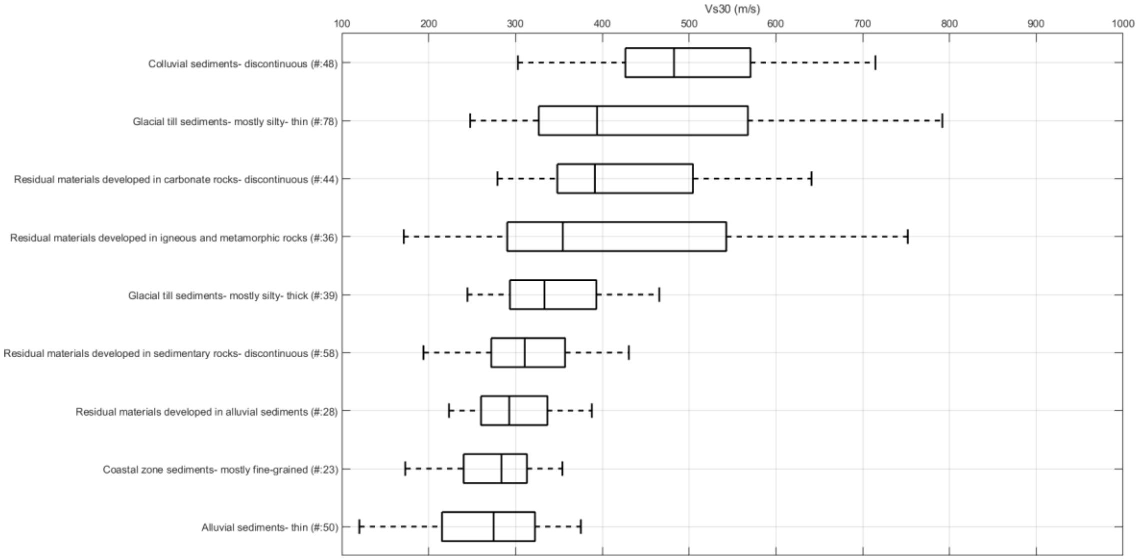

Figure 9. Box plot of estimated Vs30 (x-axis) with respect to their surficial material units. Y axis tick marks include unit names and the number of stations within that unit. Vertical line within each box is the median Vs30 of that group. Boundaries of each box represent 25th and 75th percentile of that group. Whiskers extending to each side represent ±2.7σ of that group.

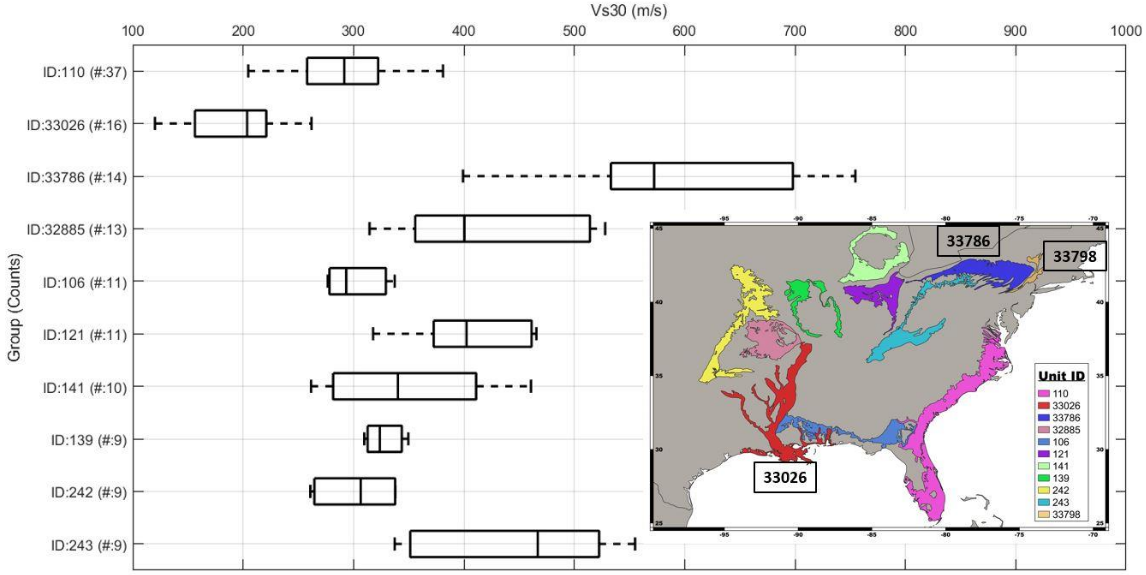

Figure 10. Box plot of estimated Vs30 (x-axis) with respect to their geological unit IDs. Units are highlighted on the onset map. Three focused units are labeled for clarity. Y axis tick marks include unit ID and the number of stations within that unit. Vertical line within each box is the median Vs30 of that group. Boundaries of each box represent 25th and 75th percentile of that group. Whiskers extending to each side represent ±2.7σ of that group.

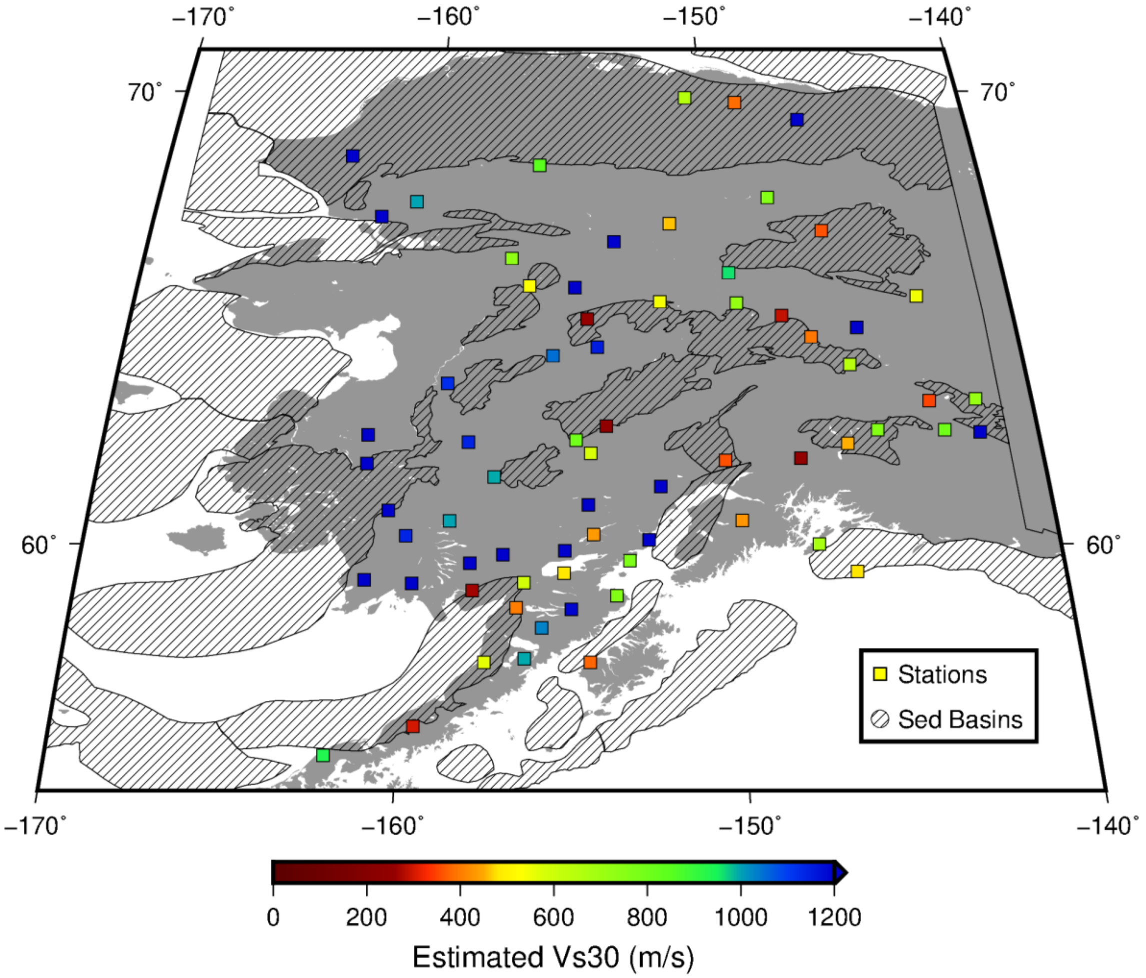

Figure 11. Vs30 results for TA stations within Alaska. Shaded areas are sedimentary basins defined in Coleman and Cahan, 2012.

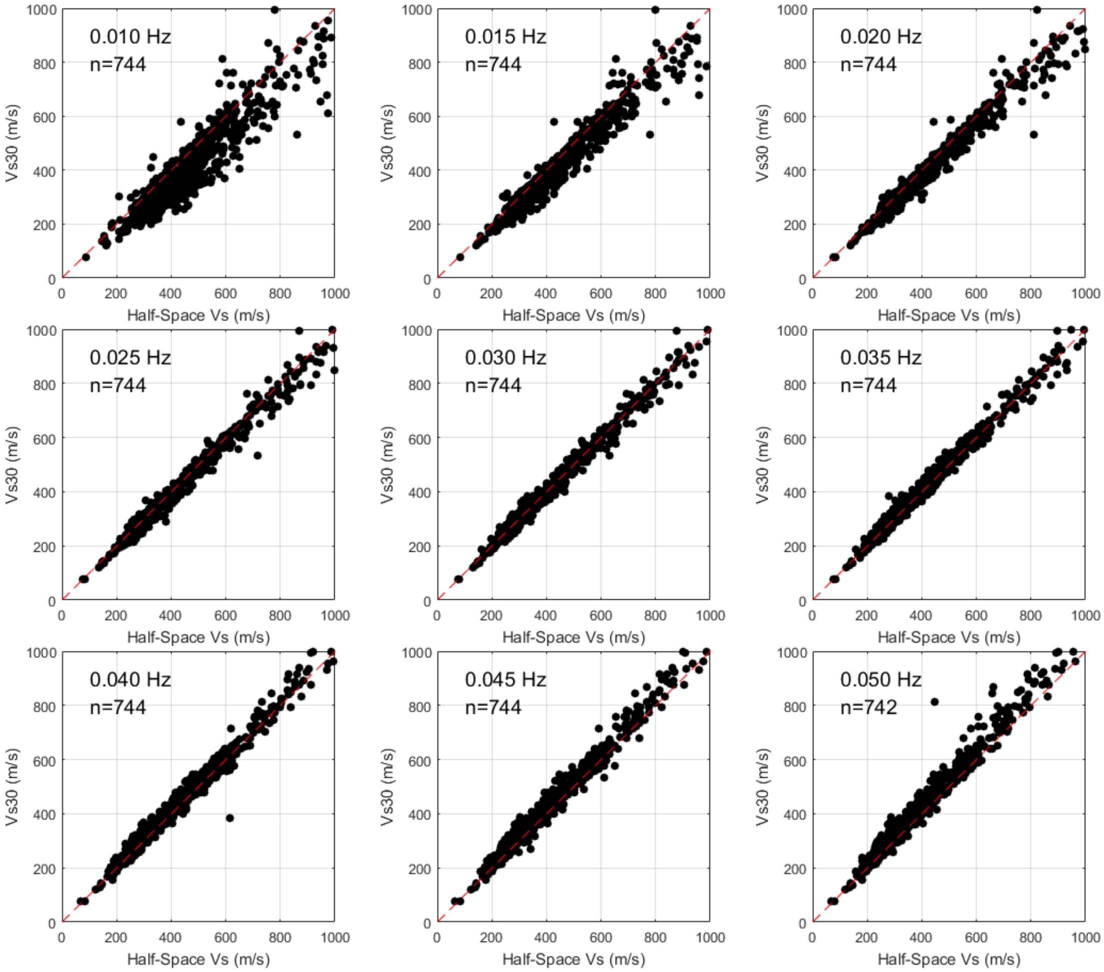

Figure 12. Comparison between half-space Vs (x-axis) and layered Vs30 at various frequencies (y-axis). Limits of all axes are set to 1000 m/s. Red diagonal dashed lines are one-to-one line. “n” is the total number of points in each panel.

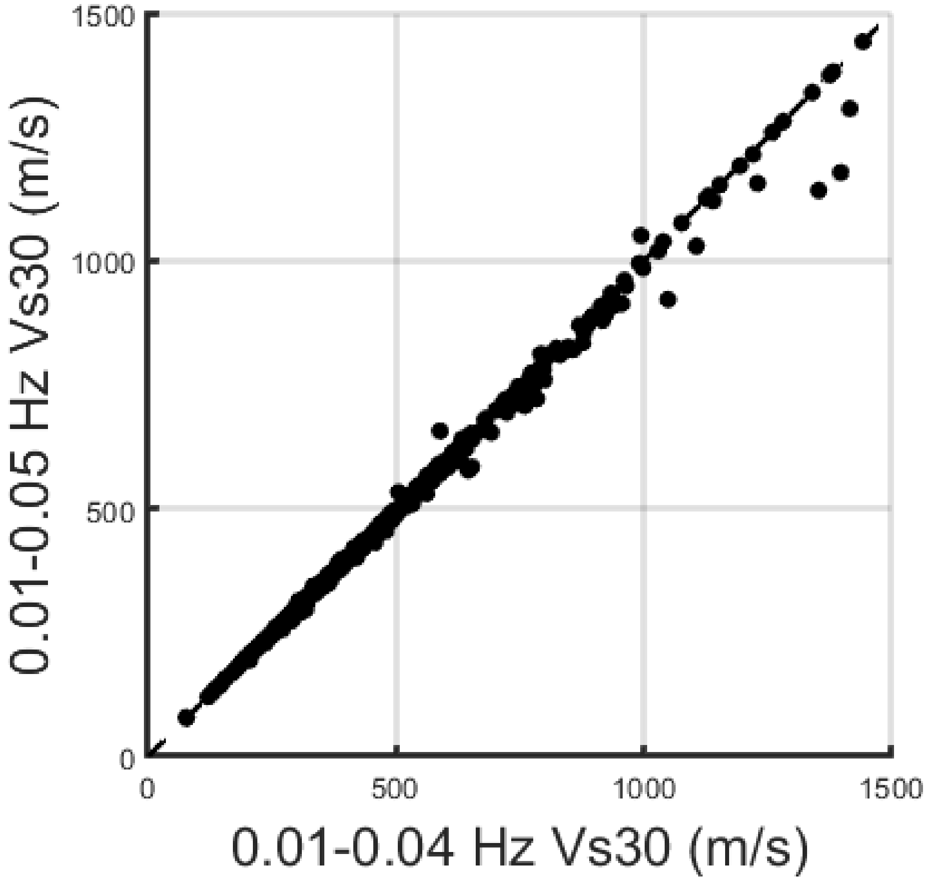

Figure 13. Comparison of inverted Vs30 in two frequency ranges: 0.01-0.05 Hz versus 0.01-0.04 Hz.

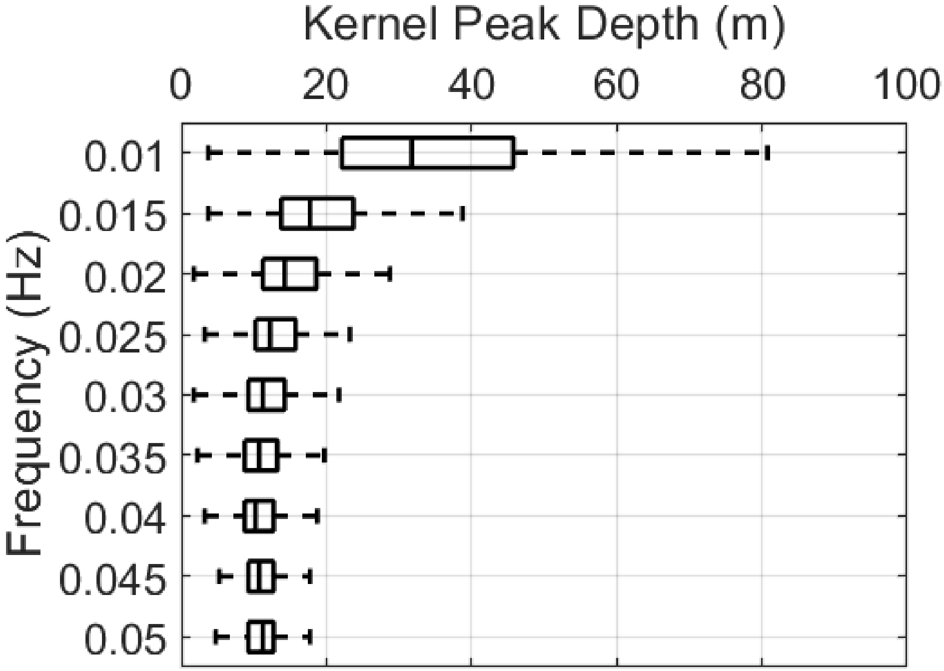

Figure 14. Box plot of peak depths of shear-modulus sensitivity kernels from 0.01 to 0.05 Hz. Vertical line within each box is the median peak depth of that frequency. Boundaries of each box represent 25th and 75th percentile of the distribution. Whiskers extending to each side represent ±2.7σ. Outliers outside of whiskers are omitted.

Frq(Hz)	kz	kh	ZP_ratio	ΔZP_ratio	HP_ratio	ΔHP_ratio	c(m/s)	Δc(m/s)	$\bar{\mu}$(Pa)	Δ$\bar{\mu}$(Pa)
0.010	517	183	1.23E-17	5.54E-18	9.25E-14	3.82E-14	1.80E+00	5.50E-01	2.56E+08	5.30E+07
0.015	2208	489	1.99E-17	6.54E-18	5.56E-14	1.70E-14	1.97E+00	4.42E-01	2.20E+08	3.37E+07
0.020	3144	708	2.94E-17	9.53E-18	3.28E-14	9.16E-15	2.34E+00	5.00E-01	2.15E+08	3.01E+07
0.025	3369	812	4.00E-17	1.12E-17	2.26E-14	5.49E-15	2.62E+00	4.86E-01	2.07E+08	2.51E+07
0.030	2991	788	5.23E-17	1.57E-17	1.60E-14	4.08E-15	2.97E+00	5.86E-01	2.06E+08	2.62E+07
0.035	2641	819	6.44E-17	1.90E-17	1.22E-14	3.00E-15	3.24E+00	6.24E-01	2.02E+08	2.49E+07
0.040	2215	742	7.59E-17	2.65E-17	9.44E-15	2.15E-15	3.50E+00	7.28E-01	2.01E+08	2.29E+07
0.045	1739	667	9.21E-17	2.93E-17	7.58E-15	1.66E-15	3.82E+00	7.38E-01	1.99E+08	2.18E+07
0.050	1134	519	1.23E-16	4.54E-17	6.50E-15	1.73E-15	4.30E+00	9.76E-01	1.93E+08	2.57E+07

Table 1. Data for 355A from 0.01 to 0.05 Hz. frq is each discrete frequency, kz is the number of vertical seismic PSDs that pass criteria, kh is the number of horizontal seismic PSDs that pass criteria, ZP_ratio is averaged ratio of S_Z/S_P, ΔZP_ratio is one standard deviation of ZP_ratio, HP_ratio is averaged ratio of S_H/S_P, ΔHP_ratio is one standard deviation of HP_ratio, c is pressure wave speed, Δc is one standard deviation of c, $\bar{\mu}$ is modified shear-modulus, $\Delta\bar{\mu}$ is one standard deviation of modified shear-modulus.

Frq(Hz)	kz	kh	ZP_ratio	ΔZP_ratio	HP_ratio	ΔHP_ratio	c(m/s)	Δc(m/s)	$\bar{\mu}$(Pa)	$\Delta\bar{\mu}$(Pa)
0.010	682	4294	5.09E-18	2.80E-18	1.09E-14	2.81E-15	3.37E+00	1.02E+00	7.47E+08	9.61E+07
0.015	2893	4707	7.68E-18	2.96E-18	6.11E-15	1.45E-15	3.69E+00	8.34E-01	6.65E+08	7.87E+07
0.020	3988	4975	1.01E-17	4.24E-18	3.97E-15	1.02E-15	3.94E+00	9.65E-01	6.19E+08	7.91E+07
0.025	4369	5343	1.21E-17	4.56E-18	2.79E-15	6.53E-16	4.11E+00	9.11E-01	5.90E+08	6.90E+07
0.030	4236	5257	1.36E-17	5.41E-18	2.05E-15	5.08E-16	4.23E+00	9.92E-01	5.74E+08	7.09E+07
0.035	3782	5198	1.59E-17	5.88E-18	1.59E-15	3.70E-16	4.46E+00	9.70E-01	5.58E+08	6.47E+07
0.040	3151	4717	1.77E-17	7.13E-18	1.26E-15	2.96E-16	4.62E+00	1.08E+00	5.49E+08	6.44E+07

Table 2. Data for I05D from 0.01 to 0.04 Hz. All fields are the same as Table 1.

5 Future Direction

Throughout Chapters 2, 3 and 4, we demonstrated that our method could have a great potential to provide important information for seismic hazard analyses; however, there is more work to be done to better understand the nature of low-frequency seismic noise and utilize it for future studies. Below we list three important topics that need to be further investigated.

5.1 Relationship between pressure waves and surface wind

First of all, we need to clarify the relationship between the excitation source-pressure waves and surface wind. It is crucial to understand how low-frequency pressure data are generated more precisely. Although pressure variations are closely connected to surface winds, yet there is no robust quantitative relationship that has been established between them at low frequencies. We can make quantitative analysis on how pressure waves in theory can be associated with surface wind flow by studying collocated wind speed and direction data. Better understanding of the excitation source will help promote our method by providing a more complete and robust theory.

5.2 Limitation in the frequency range

In the end of Chapter 4, we briefly discussed some limitations of our results that naturally arise due to the frequency range of our study. We should explore the full potential of our method by further examining the frequency range. Currently we utilize data from 0.01 to 0.05 Hz, and resolved depths are typically confined at 100 meters or less, with a lack of resolution in the uppermost 5 or 10 meters. In order to resolve the uppermost layer with our method, we have to utilize data at frequencies higher than 0.05 Hz. Data at higher frequencies exhibit more effects from the primary microseism, which sometimes mask signals generated by pressure changes; however, analysis of higher-frequency data is feasible if we only focus on time intervals when the surface pressure changes are large and overcome competing signals from the primary microseism. Theoretical formulations for data at higher and lower frequencies will also need to be revisited, due to the change of some assumptions in the derivation. In short, by exploring data at both higher or lower frequencies, we can potentially construct velocity profiles at greater depths and provide more detailed information.

5.3 Temporal and other systematic patterns

There are still systematic patterns in the low-frequency seismic noise that we do not fully understand yet, for example, seasonal variations in the seismic noise in term of drastically different amplitudes in the summer and winter months, with many stations located in Alaska. The seasonal variations can be potentially linked to the thawing of the frozen surface during season changes. Other systematic patterns include short-term temporal variations in term of different weather events such as precipitations and snowfall, and large amplitude difference between two horizontal seismic components at certain stations. These investigations will be challenging because they require cross-disciplinary knowledge of various surface processes and other additional information that might be difficult to obtain. Nevertheless, results from these investigations will greatly expand our knowledge on the low-frequency seismic noise and undoubtedly provide exciting new topics of research.

6 Appendix

This section includes supplemental materials for Chapter 3 and Chapter 4.

6.1 Appendix of Chapter 3

This supplemental material includes three tables and three figures that provide additional information of our project. Table S1 contains calculated rigidities and uncertainties at 784 TA stations. Tables S2-S3 contains names and coordinates of stations we categorized as “Appalachian” and “Mississippi” stations in Figures 5 - 6 of the manuscript. All three tables are formatted as separate csv files. Figure S1 shows pressure-seismic plots at adjacent frequency bands as references to compare with the focused frequency band of our study (0.02 Hz). Figure S2 shows examples of culled station in our data quality-control steps. Figure S3 demonstrates the consistency within our approach at 13 TA backbone stations from 2012 to 2018.

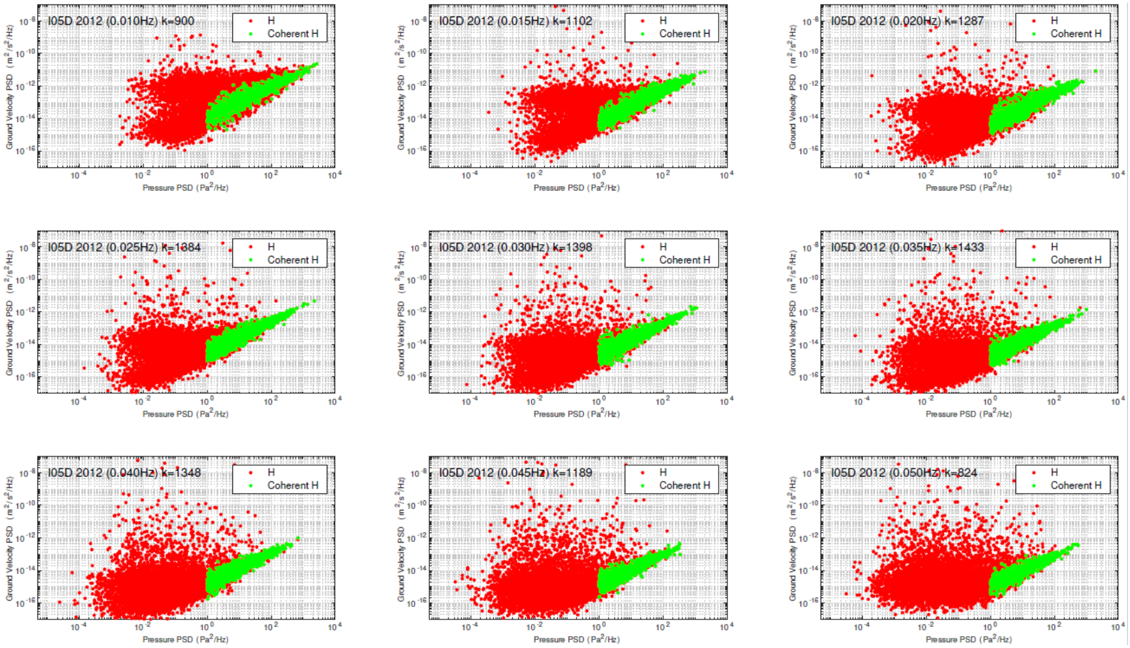

Figure S1. Comparison of pressure-seismic plots between different frequencies (0.01 - 0.05 Hz). Data are for TA station I05D in 2012. Red points are all hourly horizontal PSDs and green points are PSDs that pass the data-culling procedure. “k” in the title of each subplots denote the number of green points in each subplot.

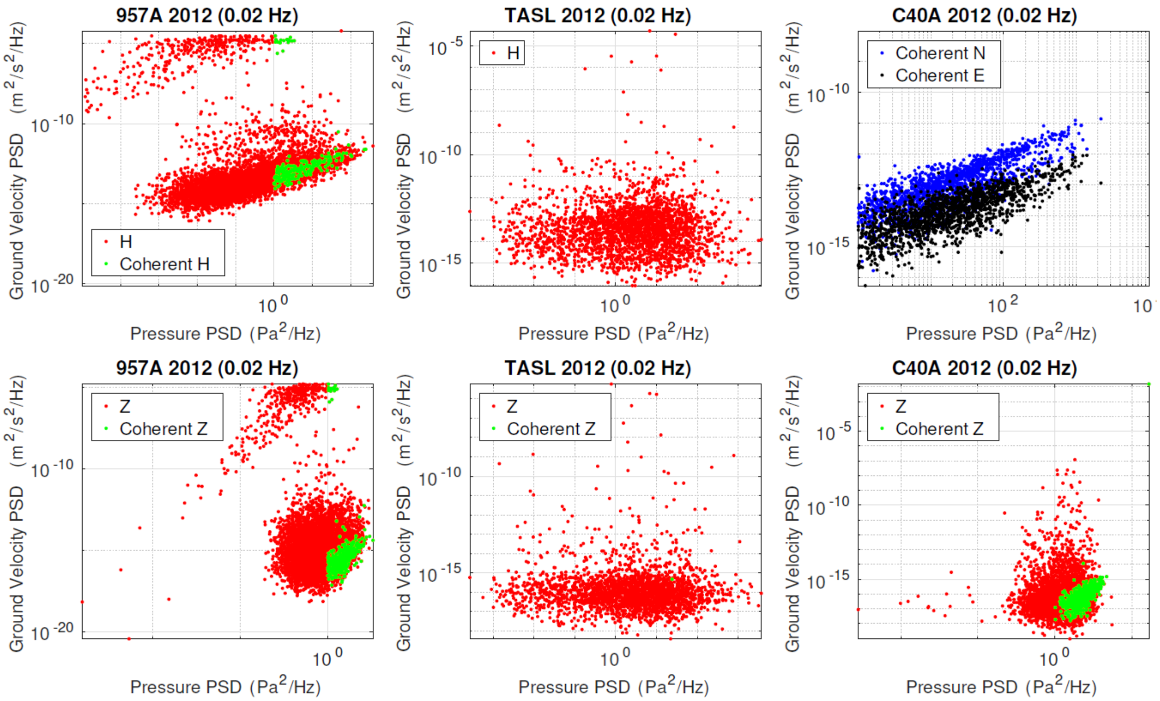

Figure S2. Examples of stations excluded from the rigidity calculation. Left panels show an example of stations that contain erroneous data portion, either in seismic or pressure data. Middle panels show an example of stations that contain less than 50 coherent PSDs. Right panels show an example of stations that show significant deviation between N-S and E-W horizontal PSDs.

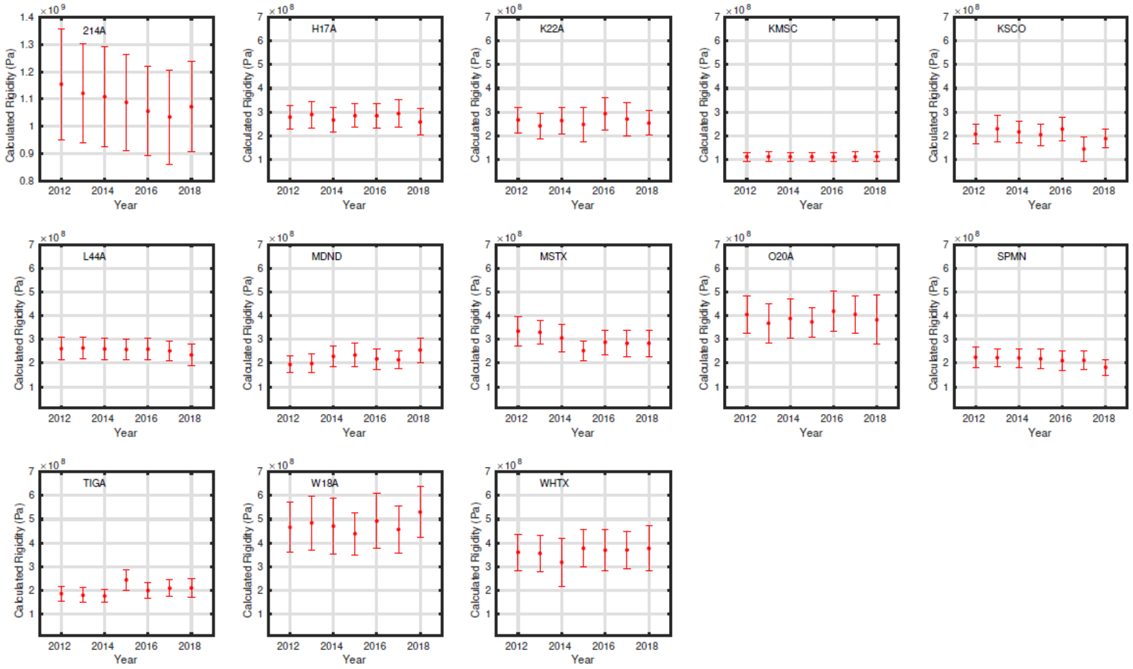

Figure S3. Rigidity estimates with uncertainties at 13 TA backbone stations from 2012 to 2018. Y-axis limit is set between 1e7 to 7e8 Pa for consistency, except for station 214A due to its high estimated rigidity.

station	Rigidity	Sigma_Rigidity	station	Rigidity	Sigma_Rigidity
059A	2.04E+08	3.42E+07	L56A	6.17E+08	7.73E+07
059Z	2.06E+08	4.48E+07	L57A	1.03E+09	2.72E+08
060A	2.36E+08	3.82E+07	L58A	1.22E+09	2.06E+08
060Z	3.92E+08	7.23E+07	L60A	1.13E+09	1.87E+08
061Z	3.80E+08	6.75E+07	L61A	6.16E+08	1.15E+08
062Z	1.78E+08	2.41E+07	L61B	8.83E+08	1.45E+08
121A	6.01E+08	1.10E+08	L62A	1.48E+08	2.92E+07
140A	9.31E+07	1.28E+07	L63A	4.28E+08	8.40E+07
141A	1.87E+08	3.31E+07	L64A	3.01E+08	5.74E+07
142A	9.67E+07	2.28E+07	L65A	1.34E+08	2.01E+07
143A	7.11E+07	1.08E+07	M02C	8.59E+08	1.38E+08
144A	9.83E+07	1.49E+07	M04C	3.36E+08	6.31E+07
145A	1.19E+08	2.30E+07	M11K	3.82E+09	1.02E+09
146A	1.98E+08	3.65E+07	M13K	7.56E+09	1.82E+09
147A	5.24E+08	7.88E+07	M14K	5.27E+08	2.69E+08
148A	1.37E+08	1.79E+07	M15K	5.11E+09	1.05E+09
149A	1.81E+08	2.85E+07	M17K	2.31E+09	5.96E+08
150A	2.52E+08	5.28E+07	M18K	4.27E+09	7.69E+08
151A	3.04E+08	4.58E+07	M19K	8.19E+08	1.89E+08
153A	2.29E+08	3.03E+07	M22K	2.77E+08	4.81E+07
154A	2.55E+08	4.27E+07	M23K	1.14E+08	3.23E+07
155A	3.55E+08	6.53E+07	M24K	4.41E+08	8.84E+07
156A	1.79E+08	3.30E+07	M26K	1.17E+09	2.30E+08
157A	2.27E+08	3.65E+07	M27K	6.00E+09	1.62E+09
158A	2.11E+08	4.65E+07	M29M	5.41E+09	1.76E+09
214A	1.09E+09	1.78E+08	M30M	9.03E+09	2.00E+09
241A	1.57E+08	2.20E+07	M31M	5.87E+08	9.09E+07
244A	1.90E+08	3.40E+07	M38A	1.71E+08	4.54E+07
245A	2.19E+08	3.95E+07	M39A	1.67E+08	3.30E+07
246A	7.21E+07	1.52E+07	M40A	2.33E+08	5.74E+07
247A	1.84E+08	3.36E+07	M41A	2.43E+08	5.51E+07
248A	1.68E+08	2.39E+07	M42A	2.11E+08	3.38E+07
249A	2.49E+08	3.38E+07	M43A	1.29E+08	3.78E+07
250A	2.01E+08	3.63E+07	M44A	2.50E+08	3.59E+07
251A	1.82E+08	2.71E+07	M45A	2.10E+08	4.51E+07
252A	1.40E+08	2.85E+07	M46A	2.16E+08	4.88E+07
253A	1.81E+08	2.71E+07	M47A	2.51E+08	4.43E+07

254A	2.59E+08	5.79E+07	M48A	3.53E+08	6.10E+07
255A	2.74E+08	3.63E+07	M49A	2.42E+08	3.83E+07
256A	2.44E+08	3.33E+07	M51A	3.51E+08	6.94E+07
257A	1.33E+08	2.35E+07	M53A	4.66E+08	8.76E+07
341A	2.06E+08	3.33E+07	M54A	5.64E+08	7.99E+07
342A	1.70E+08	3.17E+07	M55A	2.82E+08	5.08E+07
343A	4.27E+07	8.04E+06	M57A	3.85E+08	5.32E+07
345A	1.72E+08	2.20E+07	M60A	1.54E+09	3.02E+08
346A	1.87E+08	3.43E+07	M61A	3.69E+08	5.90E+07
347A	1.75E+08	3.74E+07	M63A	1.25E+09	1.86E+08
348A	1.70E+08	2.47E+07	M64A	1.43E+09	3.26E+08
349A	1.77E+08	2.83E+07	M65A	4.63E+07	1.33E+07
350A	1.56E+08	2.33E+07	M66A	1.56E+08	2.76E+07
351A	2.13E+08	4.03E+07	MDND	2.20E+08	4.29E+07
352A	1.74E+08	2.77E+07	MSTX	2.97E+08	5.37E+07
353A	3.19E+08	4.89E+07	N02D	3.48E+08	6.82E+07
355A	2.16E+08	3.20E+07	N14K	2.63E+09	8.52E+08
356A	1.52E+08	2.73E+07	N15K	2.34E+09	5.51E+08
357A	1.54E+08	2.56E+07	N16K	1.93E+09	5.48E+08
441A	1.19E+08	1.82E+07	N17K	2.44E+09	6.61E+08
442A	6.68E+07	1.57E+07	N18K	3.21E+09	1.17E+09
443A	5.53E+07	1.14E+07	N19K	1.13E+10	4.57E+09
444A	1.40E+08	1.93E+07	N20K	6.28E+09	1.91E+09
445A	1.91E+08	2.48E+07	N25K	1.21E+10	2.69E+09
446A	1.38E+08	2.22E+07	N30M	9.33E+08	3.67E+08
447A	1.44E+08	2.29E+07	N31M	1.09E+09	2.20E+08
449A	1.67E+08	2.44E+07	N32M	2.21E+08	3.91E+07
450A	2.32E+08	4.29E+07	N37A	1.79E+08	3.32E+07
451A	2.14E+08	6.03E+07	N39A	2.60E+08	4.60E+07
452A	3.71E+08	6.10E+07	N40A	1.83E+08	3.09E+07
453A	1.72E+08	4.66E+07	N41A	2.29E+08	5.89E+07
454A	2.05E+08	3.38E+07	N42A	2.09E+08	4.01E+07
455A	2.47E+08	4.70E+07	N43A	2.84E+08	4.87E+07
456A	2.32E+08	3.70E+07	N46A	3.52E+08	6.88E+07
457A	1.47E+08	2.40E+07	N47A	3.59E+08	6.87E+07
541A	6.22E+07	1.76E+07	N49A	8.72E+08	2.20E+08
542A	8.17E+07	2.11E+07	N52A	2.42E+08	3.53E+07
543A	4.08E+07	6.55E+06	N53A	4.70E+08	1.05E+08
544A	3.12E+07	6.15E+06	N54A	3.89E+08	6.89E+07

545A	7.02E+07	9.30E+06	N55A	6.33E+08	1.09E+08
552A	2.61E+08	5.30E+07	N56A	4.23E+08	8.91E+07
553A	1.80E+08	3.26E+07	N57A	2.93E+08	4.81E+07
554A	2.95E+08	4.44E+07	N58A	1.86E+09	3.42E+08
555A	2.34E+08	4.22E+07	N59A	5.42E+08	9.56E+07
556A	2.90E+08	5.38E+07	N60A	1.40E+09	2.44E+08
557A	3.14E+08	6.16E+07	N61A	5.53E+08	1.12E+08
645A	3.52E+07	7.08E+06	N62A	3.12E+08	4.56E+07
655A	7.63E+08	1.59E+08	N63A	1.13E+08	1.66E+07
656A	1.99E+08	5.30E+07	O02D	5.01E+08	8.60E+07
657A	1.80E+08	3.02E+07	O03D	4.88E+08	1.19E+08
658A	1.38E+08	2.78E+07	O03E	5.79E+08	9.35E+07
757A	3.07E+08	5.91E+07	O14K	3.41E+09	9.33E+08
758A	2.11E+08	3.49E+07	O15K	5.97E+09	1.43E+09
857A	2.07E+08	3.12E+07	O16K	7.12E+09	1.63E+09
858A	1.37E+08	2.79E+07	O17K	8.82E+09	1.93E+09
859A	2.30E+08	3.70E+07	O18K	4.43E+09	1.79E+09
957A	1.42E+08	3.63E+07	O19K	3.96E+08	8.75E+07
959A	1.89E+08	5.19E+07	O20A	3.92E+08	8.18E+07
A04D	2.90E+08	4.72E+07	O20K	4.61E+09	9.46E+08
A19K	4.12E+09	1.85E+09	O22K	3.38E+08	5.45E+07
A36M	2.40E+09	1.24E+09	O29M	5.39E+09	1.29E+09
ABTX	4.24E+08	9.02E+07	O30N	2.25E+09	4.28E+08
B05D	5.91E+08	8.88E+07	O37A	1.90E+08	4.84E+07
B18K	5.45E+09	1.41E+09	O38A	1.62E+08	3.16E+07
B21K	7.60E+09	1.70E+09	O39A	2.04E+08	4.78E+07
BGNE	1.53E+08	3.74E+07	O40A	2.97E+08	6.57E+07
C06D	1.76E+08	3.20E+07	O41A	2.00E+08	5.28E+07
C16K	2.35E+09	2.26E+09	O42A	1.85E+08	3.19E+07
C17K	4.13E+09	2.43E+09	O43A	2.52E+08	3.42E+07
C18K	4.18E+09	2.05E+09	O44A	2.36E+08	3.80E+07
C21K	2.28E+10	9.35E+09	O45A	1.96E+08	4.94E+07
C23K	1.81E+09	4.97E+08	O47A	3.24E+08	5.17E+07
C26K	1.04E+09	5.73E+08	O48A	2.62E+08	4.41E+07
C36M	3.74E+08	1.65E+08	O48B	2.89E+08	3.01E+07
D03D	1.34E+09	2.85E+08	O50A	4.47E+08	6.87E+07
D04E	3.02E+08	4.43E+07	O52A	4.71E+08	8.51E+07
D17K	1.45E+10	6.05E+09	O53A	5.16E+08	8.71E+07
D20K	1.62E+10	4.48E+09	O54A	3.17E+08	5.50E+07

D22K	1.52E+09	7.74E+08	O55A	5.65E+08	9.81E+07
D23K	2.18E+10	6.01E+09	O56A	1.04E+09	1.84E+08
D25K	2.73E+09	1.27E+09	O57A	1.72E+09	3.32E+08
D27M	1.48E+10	6.89E+09	O58A	1.34E+09	3.21E+08
D41A	3.13E+08	6.19E+07	O59A	6.96E+08	1.05E+08
D46A	3.17E+08	5.37E+07	O60A	1.30E+09	2.38E+08
D47A	6.73E+08	1.22E+08	O61A	2.42E+08	3.47E+07
D49A	2.50E+08	5.65E+07	P16K	1.22E+08	3.72E+07
D52A	7.39E+08	1.17E+08	P17K	5.04E+08	1.48E+08
D54A	1.13E+09	1.54E+08	P18K	4.31E+08	1.60E+08
D57A	8.76E+08	1.88E+08	P19K	1.02E+09	2.64E+08
D59A	1.71E+08	3.02E+07	P23K	8.77E+08	2.35E+08
D60A	1.98E+09	3.47E+08	P29M	8.95E+08	1.66E+08
D61A	9.24E+08	2.55E+08	P30M	3.84E+09	8.62E+08
D62A	1.32E+09	2.33E+08	P33M	4.15E+09	1.84E+09
D63A	1.48E+09	2.68E+08	P37A	2.43E+08	4.73E+07
E04D	2.65E+08	4.82E+07	P39B	2.40E+08	4.61E+07
E17K	8.98E+09	2.59E+09	P40A	2.53E+08	3.92E+07
E18K	1.95E+09	7.82E+08	P41A	4.75E+08	9.27E+07
E19K	8.73E+09	1.63E+09	P42A	2.56E+08	5.54E+07
E20K	1.81E+09	1.43E+09	P43A	3.86E+08	7.48E+07
E21K	1.77E+09	6.82E+08	P44A	3.17E+08	5.85E+07
E22K	4.74E+09	1.49E+09	P45A	3.06E+08	5.62E+07
E23K	7.68E+09	2.04E+09	P46A	2.43E+08	4.39E+07
E24K	3.97E+09	8.91E+08	P47A	4.01E+08	5.95E+07
E27K	1.26E+10	2.58E+09	P49A	3.91E+08	7.10E+07
E38A	2.96E+08	5.45E+07	P50A	1.29E+08	2.85E+07
E39A	4.66E+08	8.66E+07	P51A	3.60E+08	6.04E+07
E40A	4.27E+08	1.13E+08	P52A	4.72E+08	1.12E+08
E41A	2.24E+08	5.63E+07	P53A	3.67E+08	7.00E+07
E42A	5.36E+08	1.14E+08	P54A	8.92E+08	1.72E+08
E43A	6.19E+08	1.16E+08	P55A	4.89E+08	1.19E+08
E44A	1.77E+08	3.37E+07	P56A	8.82E+08	1.75E+08
E45A	1.79E+08	2.55E+07	P57A	2.50E+08	3.69E+07
E46A	3.48E+08	5.91E+07	P58A	1.56E+09	2.47E+08
E48A	2.20E+08	4.68E+07	P59A	1.19E+08	1.10E+07
E50A	2.95E+08	6.55E+07	P60A	3.27E+08	4.24E+07
E52A	1.40E+09	2.02E+08	P61A	1.48E+08	2.62E+07
E53A	7.38E+08	1.25E+08	Q16K	4.55E+08	9.39E+07

E54A	2.06E+09	3.63E+08	Q17K	2.08E+09	7.74E+08
E55A	1.57E+08	2.79E+07	Q18K	2.49E+09	6.71E+08
E56A	8.21E+06	1.40E+06	Q19K	9.22E+08	2.56E+08
E57A	8.07E+08	1.26E+08	Q20K	5.39E+09	1.29E+09
E58A	7.84E+08	1.35E+08	Q32M	8.48E+09	2.08E+09
E59A	1.47E+08	4.08E+07	Q39A	2.05E+08	4.25E+07
E61A	3.12E+09	7.72E+08	Q40A	1.35E+08	3.24E+07
E63A	1.51E+09	2.38E+08	Q41A	2.77E+08	3.99E+07
E64A	4.83E+09	1.32E+09	Q42A	1.62E+08	3.81E+07
EPYK	3.13E+08	8.42E+07	Q43A	3.17E+08	5.57E+07
F04D	1.86E+08	2.84E+07	Q44A	3.35E+08	6.82E+07
F05D	2.09E+08	4.02E+07	Q46A	3.66E+08	7.73E+07
F14K	1.87E+09	1.41E+09	Q47A	4.41E+08	7.04E+07
F15K	8.50E+08	4.82E+08	Q48A	2.13E+08	2.97E+07
F17K	1.81E+09	7.27E+08	Q49A	4.49E+08	6.41E+07
F18K	8.06E+09	2.28E+09	Q50A	1.10E+09	1.25E+08
F19K	1.47E+09	5.94E+08	Q51A	8.16E+08	1.33E+08
F20K	2.48E+09	6.88E+08	Q52A	2.83E+08	5.08E+07
F22K	5.62E+09	1.47E+09	Q53A	9.12E+08	1.51E+08
F24K	1.34E+09	5.86E+08	Q54A	5.95E+08	1.30E+08
F25K	7.52E+09	2.44E+09	Q55A	4.08E+08	8.59E+07
F26K	1.17E+10	3.44E+09	Q56A	8.80E+08	1.69E+08
F28M	1.02E+09	4.33E+08	Q57A	1.38E+09	2.69E+08
F30M	1.34E+09	7.81E+08	Q58A	7.45E+08	1.72E+08
F31M	5.05E+08	2.13E+08	Q59A	1.89E+08	3.87E+07
F37A	2.18E+08	3.54E+07	Q60A	1.55E+08	2.85E+07
F38A	1.79E+08	3.01E+07	Q61A	1.61E+08	2.78E+07
F39A	2.39E+08	4.04E+07	R11A	1.45E+09	2.97E+08
F40A	2.54E+08	5.36E+07	R11B	2.67E+09	6.31E+08
F41A	2.82E+08	7.73E+07	R16K	7.79E+08	1.64E+08
F42A	1.47E+08	2.43E+07	R17K	1.26E+09	3.34E+08
F43A	1.19E+09	2.60E+08	R18K	2.99E+08	7.26E+07
F44A	5.86E+08	7.46E+07	R32K	2.56E+06	1.01E+06
F45A	6.04E+08	1.05E+08	R38A	4.85E+08	8.54E+07
F46A	4.86E+08	5.49E+07	R39A	3.10E+08	5.02E+07
F48A	6.21E+08	1.13E+08	R40A	1.94E+08	3.28E+07
F49A	7.11E+08	1.01E+08	R41A	2.64E+08	2.98E+07
F51A	6.23E+08	1.13E+08	R42A	2.14E+08	3.66E+07
F52A	2.12E+08	4.16E+07	R43A	2.27E+08	3.45E+07

F55A	1.81E+08	2.95E+07	R44A	3.14E+08	7.75E+07
F57A	1.22E+08	2.16E+07	R45A	4.45E+08	9.33E+07
F59A	1.19E+08	3.51E+07	R46A	5.28E+08	7.90E+07
F60A	3.61E+08	1.23E+08	R47A	3.54E+08	9.85E+07
F61A	6.10E+08	1.46E+08	R48A	1.37E+08	3.53E+07
F62A	3.34E+08	8.43E+07	R49A	1.12E+09	2.00E+08
F63A	7.31E+08	1.02E+08	R51A	9.02E+07	1.12E+07
F64A	1.67E+09	2.41E+08	R53A	6.17E+08	1.02E+08
G03D	2.23E+08	3.56E+07	R54A	5.69E+08	1.15E+08
G05D	3.48E+08	6.42E+07	R55A	1.00E+09	2.09E+08
G15K	1.43E+09	6.98E+08	R56A	5.72E+08	1.20E+08
G18K	1.16E+10	2.91E+09	R57A	4.11E+08	7.81E+07
G19K	1.31E+09	2.77E+08	R58B	1.75E+08	3.31E+07
G21K	4.64E+09	1.22E+09	R59A	1.35E+08	2.17E+07
G22K	5.27E+08	9.43E+07	R60A	1.83E+08	2.78E+07
G23K	7.01E+09	1.88E+09	R61A	1.40E+08	2.12E+07
G24K	3.03E+09	8.46E+08	S12K	1.63E+09	4.70E+08
G25K	2.69E+08	4.08E+07	S14K	1.84E+08	5.12E+07
G26K	1.39E+09	4.13E+08	S31K	6.59E+08	1.66E+08
G27K	8.70E+08	1.74E+08	S32K	3.80E+06	8.65E+05
G29M	1.97E+09	4.26E+08	S39A	5.07E+08	9.43E+07
G30M	3.00E+09	1.99E+09	S40A	4.19E+08	9.14E+07
G31M	2.42E+09	5.04E+08	S41A	3.18E+08	5.39E+07
G38A	3.47E+08	7.54E+07	S42A	2.15E+08	4.08E+07
G39A	2.99E+08	4.92E+07	S44A	2.74E+08	4.89E+07
G40A	3.85E+08	6.28E+07	S45A	4.21E+08	7.56E+07
G41A	2.38E+08	5.94E+07	S46A	4.73E+08	8.57E+07
G42A	3.20E+08	6.78E+07	S47A	3.80E+08	5.74E+07
G43A	7.19E+08	1.68E+08	S48A	2.69E+09	5.45E+08
G45A	6.03E+08	9.02E+07	S49A	1.28E+09	1.94E+08
G46A	1.41E+08	2.14E+07	S50A	3.09E+08	5.05E+07
G47A	3.06E+08	6.14E+07	S51A	5.35E+08	8.78E+07
G53A	2.71E+08	5.25E+07	S52A	2.35E+08	4.56E+07
G54A	8.01E+08	1.63E+08	S53A	2.26E+08	4.26E+07
G55A	6.66E+08	1.03E+08	S54A	5.92E+08	1.23E+08
G57A	4.95E+08	1.44E+08	S55A	6.36E+08	8.35E+07
G58A	1.49E+08	2.63E+07	S56A	9.60E+07	1.71E+07
G60A	7.08E+08	1.46E+08	S57A	2.28E+08	4.38E+07
G61A	1.45E+09	2.72E+08	S58A	6.70E+07	1.23E+07

G64A	3.96E+09	8.38E+08	S59A	1.42E+08	2.11E+07
H04D	2.51E+08	4.73E+07	S60A	1.30E+08	1.99E+07
H16K	7.48E+09	1.73E+09	S61A	1.79E+08	2.81E+07
H17A	2.79E+08	5.29E+07	SFIN	4.27E+08	7.50E+07
H17K	6.45E+09	1.52E+09	SPMN	2.13E+08	3.86E+07
H18K	7.27E+09	2.14E+09	SUSD	1.71E+08	3.61E+07
H20K	9.01E+09	2.03E+09	T33K	1.10E+07	2.71E+06
H22K	1.04E+10	3.36E+09	T35M	8.84E+08	1.65E+08
H23K	4.92E+09	1.19E+09	T38A	4.95E+08	1.01E+08
H24K	2.90E+09	8.95E+08	T39A	4.27E+08	9.20E+07
H25L	1.17E+08	5.04E+07	T40A	8.96E+08	1.63E+08
H27K	9.60E+08	3.16E+08	T41A	3.22E+08	5.91E+07
H31M	2.58E+09	8.01E+08	T42A	4.67E+08	8.36E+07
H38A	3.34E+08	3.46E+07	T43A	3.09E+08	5.72E+07
H40A	5.56E+08	1.12E+08	T44A	1.27E+08	2.05E+07
H41A	8.60E+08	1.13E+08	T45A	1.11E+08	1.85E+07
H42A	1.50E+08	2.63E+07	T46A	2.02E+08	4.34E+07
H43A	6.77E+08	1.13E+08	T47A	3.98E+08	6.15E+07
H45A	1.88E+08	3.06E+07	T48A	3.38E+08	7.57E+07
H46A	2.84E+08	6.84E+07	T49A	2.55E+08	4.78E+07
H47A	1.83E+08	2.81E+07	T50A	2.42E+08	4.44E+07
H48A	1.08E+08	1.96E+07	T51A	4.15E+08	7.62E+07
H52A	2.45E+08	4.84E+07	T52A	2.24E+08	3.41E+07
H53A	7.19E+08	1.44E+08	T53A	4.33E+08	6.76E+07
H55A	4.99E+08	6.77E+07	T56A	2.53E+08	3.48E+07
H56A	1.99E+08	1.96E+07	T57A	2.32E+08	4.60E+07
H59A	7.91E+08	1.58E+08	T58A	1.92E+08	3.44E+07
H60A	3.99E+08	7.24E+07	T60A	1.37E+08	1.89E+07
H62A	5.83E+08	1.17E+08	TCOL	2.91E+08	9.65E+07
H63A	1.66E+08	2.80E+07	TIGA	2.01E+08	3.39E+07
H64A	1.46E+09	3.49E+08	TPFO	4.18E+08	9.08E+07
H65A	2.37E+08	4.42E+07	TUL1	2.00E+09	3.35E+08
H66A	1.79E+09	3.40E+08	U33K	7.07E+09	1.59E+09
HARP	8.33E+08	1.48E+08	U39A	2.57E+08	5.35E+07
HDA	3.40E+08	5.60E+07	U40A	6.30E+08	1.21E+08
I02D	1.47E+08	3.53E+07	U41A	4.45E+08	6.81E+07
I02E	5.16E+08	1.17E+08	U42A	5.39E+08	9.49E+07
I03D	2.06E+08	3.25E+07	U43A	9.91E+07	1.54E+07
I04A	3.38E+08	5.93E+07	U44A	7.39E+07	2.02E+07

I05D	6.23E+08	8.20E+07	U45A	1.81E+08	2.57E+07
I17K	1.48E+09	3.35E+08	U46A	1.65E+08	2.68E+07
I20K	1.23E+08	2.11E+07	U47A	3.53E+08	6.55E+07
I21K	7.02E+08	3.74E+08	U48A	3.36E+08	4.92E+07
I23K	9.95E+08	3.13E+08	U49A	4.38E+08	9.44E+07
I26K	5.58E+08	1.25E+08	U50A	6.14E+08	1.19E+08
I27K	5.23E+09	1.86E+09	U51A	2.73E+08	4.94E+07
I28M	5.29E+09	1.22E+09	U52A	1.84E+08	3.09E+07
I30M	9.09E+08	2.00E+08	U53A	2.01E+08	3.05E+07
I36A	1.70E+08	3.23E+07	U54A	2.24E+08	3.64E+07
I37A	1.57E+08	2.79E+07	U56A	7.21E+07	1.22E+07
I39A	2.48E+08	3.10E+07	U57A	1.52E+08	1.86E+07
I40A	1.72E+09	2.96E+08	U58A	1.41E+08	2.71E+07
I41A	1.72E+08	3.29E+07	U59A	1.86E+08	3.72E+07
I42A	1.77E+09	4.32E+08	U60A	1.77E+08	2.70E+07
I45A	1.60E+08	2.41E+07	U61A	1.36E+08	3.40E+07
I46A	2.32E+08	3.84E+07	V35K	3.35E+09	6.21E+08
I47A	4.41E+08	8.70E+07	V40A	7.45E+08	1.14E+08
I48A	2.09E+08	4.82E+07	V41A	6.77E+08	1.21E+08
I49A	5.80E+08	1.53E+08	V42A	1.39E+08	2.34E+07
I51A	5.46E+08	1.04E+08	V45A	1.47E+08	3.24E+07
I52A	2.80E+08	5.23E+07	V46A	5.86E+08	9.52E+07
I53A	2.94E+08	4.96E+07	V47A	2.96E+08	4.68E+07
I55A	1.06E+09	2.60E+08	V48A	4.29E+08	9.50E+07
I57A	7.55E+08	1.36E+08	V49A	2.76E+08	5.02E+07
I58A	1.70E+08	1.18E+07	V50A	6.31E+08	1.24E+08
I59A	4.95E+08	8.34E+07	V51A	6.44E+08	9.60E+07
I61A	3.79E+08	6.17E+07	V52A	6.13E+08	8.87E+07
I62A	7.55E+08	1.27E+08	V53A	5.36E+08	9.40E+07
I63A	6.13E+08	1.21E+08	V54A	3.07E+08	6.04E+07
I64A	2.69E+08	3.85E+07	V55A	2.45E+08	4.69E+07
J01D	2.11E+08	4.77E+07	V56A	3.82E+08	6.96E+07
J01E	1.65E+08	3.32E+07	V57A	6.91E+08	1.21E+08
J04D	1.17E+08	1.82E+07	V58A	1.98E+08	4.45E+07
J05D	3.41E+08	4.74E+07	V59A	3.55E+08	7.25E+07
J14K	1.87E+09	6.37E+08	V60A	1.45E+08	2.66E+07
J16K	4.23E+09	9.55E+08	V61A	2.24E+08	5.73E+07
J18K	1.85E+09	7.69E+08	W18A	4.77E+08	1.07E+08
J19K	3.13E+09	6.99E+08	W39A	3.80E+08	5.99E+07

J20K	2.49E+09	5.06E+08	W41B	4.30E+08	1.04E+08
J25K	4.28E+09	1.04E+09	W42A	8.53E+07	1.44E+07
J26L	9.91E+08	3.37E+08	W43A	1.38E+08	2.77E+07
J29M	2.44E+08	4.80E+07	W44A	1.39E+08	3.67E+07
J29N	2.23E+08	4.23E+07	W45A	1.10E+08	1.41E+07
J36A	2.22E+08	3.96E+07	W46A	2.38E+08	3.63E+07
J37A	1.21E+08	2.34E+07	W47A	4.44E+08	7.69E+07
J40A	3.17E+08	5.71E+07	W48A	5.77E+08	1.20E+08
J41A	2.12E+08	2.20E+07	W49A	4.47E+08	9.34E+07
J42A	1.27E+09	2.78E+08	W50A	7.49E+08	1.18E+08
J43A	1.70E+09	3.80E+08	W51A	2.44E+08	4.33E+07
J45A	2.14E+08	4.01E+07	W52A	2.26E+08	4.89E+07
J46A	1.96E+08	3.47E+07	W53A	2.09E+08	4.02E+07
J47A	3.86E+08	8.09E+07	W54A	4.17E+08	7.25E+07
J48A	3.05E+08	4.67E+07	W56A	8.81E+08	1.00E+08
J49A	2.49E+08	3.99E+07	W57A	4.84E+07	8.01E+06
J52A	5.62E+08	1.11E+08	W58A	3.42E+08	7.87E+07
J54A	2.76E+08	6.04E+07	W59A	1.63E+08	3.38E+07
J55A	4.40E+08	1.26E+08	W60A	1.72E+08	3.68E+07
J57A	5.83E+08	1.22E+08	W61A	1.73E+08	3.67E+07
J59A	6.90E+08	1.16E+08	WHTX	3.61E+08	8.47E+07
J60A	1.86E+09	4.14E+08	X39A	7.23E+08	7.63E+07
J62A	4.84E+08	8.11E+07	X40A	4.49E+08	7.98E+07
K02D	8.34E+08	1.52E+08	X41A	2.14E+08	3.16E+07
K04D	1.92E+08	2.43E+07	X42A	1.31E+08	2.63E+07
K13K	1.36E+09	4.14E+08	X43A	1.15E+08	2.46E+07
K15K	4.27E+09	1.76E+09	X44A	1.33E+08	2.04E+07
K20K	3.07E+09	7.71E+08	X45A	2.02E+08	2.53E+07
K22A	2.63E+08	6.06E+07	X46A	2.19E+08	4.21E+07
K24K	8.65E+08	1.82E+08	X47A	4.45E+08	1.03E+08
K27K	1.29E+09	3.31E+08	X48A	7.92E+08	2.06E+08
K29M	1.81E+09	5.15E+08	X49A	7.56E+08	2.01E+08
K36A	2.33E+08	5.52E+07	X50B	3.71E+08	5.46E+07
K38A	1.91E+08	3.86E+07	X51A	2.12E+08	3.64E+07
K39A	1.55E+08	4.22E+07	X52A	2.24E+08	5.15E+07
K40A	3.89E+08	8.66E+07	X53A	1.06E+08	1.91E+07
K41A	9.04E+08	2.00E+08	X54A	2.35E+08	4.00E+07
K42A	3.37E+08	7.92E+07	X55A	1.52E+08	2.93E+07
K43A	8.36E+08	1.90E+08	X56A	1.30E+08	2.41E+07

K46A	3.91E+08	6.46E+07	X57A	2.39E+08	3.47E+07
K48A	2.53E+08	3.88E+07	X58A	2.80E+08	5.21E+07
K49A	3.44E+08	5.36E+07	X59A	1.62E+08	3.06E+07
K50A	1.30E+08	2.24E+07	Y22D	2.25E+08	3.57E+07
K51A	1.66E+08	3.17E+07	Y22E	2.17E+08	3.30E+07
K52A	2.31E+08	3.99E+07	Y40A	4.51E+08	8.16E+07
K54A	7.55E+08	1.51E+08	Y41A	1.93E+08	3.30E+07
K55A	8.97E+08	1.56E+08	Y43A	8.74E+07	1.40E+07
K56A	6.90E+08	1.94E+08	Y44A	1.34E+08	2.10E+07
K57A	6.68E+08	1.41E+08	Y45A	8.87E+07	1.62E+07
K58A	5.80E+08	9.56E+07	Y46A	2.02E+08	3.14E+07
K59A	1.30E+09	3.12E+08	Y47A	3.10E+08	5.67E+07
K60A	1.82E+08	3.75E+07	Y48A	4.99E+08	8.72E+07
K61A	1.45E+08	3.46E+07	Y49A	6.44E+08	1.32E+08
K62A	6.90E+08	1.11E+08	Y50A	3.03E+08	5.21E+07
K63A	1.85E+09	3.54E+08	Y51A	1.73E+08	2.57E+07
KMSC	1.11E+08	1.96E+07	Y52A	3.35E+08	5.68E+07
KSCO	2.03E+08	4.75E+07	Y53A	1.49E+08	2.48E+07
L02D	7.13E+08	1.20E+08	Y54A	7.51E+08	1.15E+08
L04D	4.91E+08	7.22E+07	Y55A	5.67E+08	9.84E+07
L15K	5.62E+09	1.58E+09	Y56A	1.93E+08	2.77E+07
L16K	5.95E+09	1.39E+09	Y57A	2.09E+08	3.46E+07
L17K	4.36E+09	1.13E+09	Y58A	2.60E+08	3.83E+07
L18K	3.46E+09	7.80E+08	Z40A	2.34E+08	3.72E+07
L19K	1.42E+09	4.20E+08	Z41A	1.78E+08	3.46E+07
L20K	1.22E+08	2.88E+07	Z42A	1.83E+08	3.29E+07
L26K	2.26E+08	4.45E+07	Z43A	1.00E+08	2.04E+07
L27K	9.70E+08	1.61E+08	Z44A	4.07E+07	1.78E+07
L29M	1.29E+09	5.35E+08	Z45A	1.18E+08	1.61E+07
L36A	3.13E+08	6.20E+07	Z46A	2.27E+08	4.45E+07
L37A	2.18E+08	3.24E+07	Z47A	1.66E+08	3.22E+07
L39A	1.61E+08	3.96E+07	Z48A	4.29E+08	7.66E+07
L40A	2.21E+08	3.56E+07	Z49A	3.08E+08	6.97E+07
L41A	2.46E+08	4.76E+07	Z50A	4.05E+08	6.18E+07
L42A	2.44E+08	5.94E+07	Z51A	1.05E+08	2.67E+07
L43A	4.09E+08	9.91E+07	Z52A	1.80E+08	3.29E+07
L44A	2.55E+08	4.44E+07	Z53A	1.13E+08	2.23E+07
L47A	2.10E+08	4.24E+07	Z54A	3.07E+08	6.23E+07
L48A	4.34E+08	7.65E+07	Z55A	1.85E+08	2.92E+07

L49A	3.08E+08	6.56E+07	Z56A	1.66E+08	2.79E+07
L50A	4.05E+08	9.33E+07	Z57A	4.43E+08	8.37E+07
L53A	3.05E+08	5.28E+07	Z58A	2.51E+08	3.76E+07
L55A	6.53E+08	1.18E+08	Z59A	2.00E+08	4.36E+07

Table S1. List of estimated rigidities and uncertainties of all 784 TA stations.

Appalachian Stations	Longitude	Latitude	Appalachian Stations	Longitude	Latitude
D63A	-68.1066	47.037	O58A	-76.9228	40.1231
D62A	-69.0501	47.0819	N53A	-80.8377	40.8065
D61A	-70.1868	47.2022	O56A	-78.5663	40.2683
D60A	-70.9237	46.9139	N52A	-81.6876	40.8125
E64A	-67.8285	46.4184	O55A	-79.3041	40.2076
E63A	-68.4623	46.422	P58A	-77.3005	39.4891
F64A	-68.3496	45.8633	O53A	-81.2129	40.2493
E61A	-70.489	46.4312	O54A	-80.3778	40.1821
F62A	-69.9664	45.8968	P57A	-78.0126	39.4835
F63A	-69.1029	45.703	P56A	-78.8386	39.5044
F61A	-70.9921	45.9743	O52A	-81.8361	40.1158
G64A	-68.7558	45.2527	P54A	-80.4796	39.602
H66A	-67.3115	44.7859	P55A	-79.8265	39.5078
H65A	-68.2469	44.6961	Q57A	-78.4107	39.0353
G61A	-71.5273	45.2827	Q58A	-77.682	38.9413
H63A	-70.0353	44.6616	P52A	-82.1325	39.6337
H64A	-69.2203	44.6412	P53A	-81.3896	39.4868
G60A	-72.3337	45.0977	Q56A	-79.1871	39.0401
H62A	-71.1559	44.5743	Q55A	-80.0812	38.9952
I63A	-70.5809	44.0505	Q54A	-80.8338	38.9836
H60A	-72.6986	44.5606	R56A	-79.4031	38.4071
H59A	-73.6905	44.6455	R57A	-78.5232	38.297
I61A	-72.2083	43.9323	Q53A	-81.5251	38.8586
I62A	-71.3359	43.8743	Q52A	-82.2669	38.9622
I59A	-73.8744	43.7957	Q51A	-83.3456	39.026
J62A	-71.8127	43.2262	R55A	-80.1195	38.2825
J60A	-73.4212	43.2438	R53A	-81.9522	38.3307
I58A	-74.9733	43.6901	R54A	-80.9904	38.1909
J59A	-74.5041	43.4647	S55A	-80.5013	37.7724
K62A	-72.2345	42.6651	S56A	-79.5662	37.6771
K61A	-73.2676	42.6695	S57A	-78.9536	37.7605
L61B	-72.6802	42.4498	S54A	-81.3114	37.7997
L63A	-71.6095	41.8631	S53A	-82.1264	37.6815
K60A	-73.8886	42.6168	S52A	-83.0784	37.6791
K59A	-74.8525	42.775	T56A	-80.0311	37.0288

L61A	-73.5543	42.1934	S51A	-83.5935	37.6392
L62A	-72.6617	42.0328	T52A	-82.9852	37.1076
K58A	-75.6473	42.7633	T53A	-82.535	36.9823
K57A	-76.5163	42.7313	U54A	-81.8204	36.5209
M64A	-71.2102	41.5509	T51A	-83.9454	36.9655
L60A	-74.2226	41.989	U53A	-82.5765	36.3644
M63A	-72.0464	41.4038	U52A	-83.3671	36.3929
K56A	-77.3244	42.6981	U51A	-84.0165	36.3786
L58A	-75.8502	42.0447	U50A	-84.8431	36.4156
K55A	-78.0696	42.7278	V52A	-83.5959	35.8417
M61A	-73.7673	41.3104	V53A	-82.8124	35.6694
K54A	-78.6908	42.6097	V51A	-84.3511	35.8033
L56A	-77.5591	42.1365	V50A	-85.1	35.6713
L57A	-76.8492	42.0005	W53A	-83.163	35.1696
M60A	-74.625	41.3265	W52A	-83.9277	35.0935
L55A	-78.4368	42.1831	W51A	-84.7599	35.1606
N60A	-75.1	40.8704	W50A	-85.3119	35.2002
N59A	-75.7703	40.9168	W49A	-86.2645	35.1194
M55A	-78.7649	41.4686	X52A	-83.8938	34.6032
M57A	-77.128	41.3372	X48A	-87.0452	34.4517
N58A	-76.7158	40.8396	X49A	-86.326	34.5126
O60A	-75.405	40.3177	X50B	-85.6499	34.4611
M54A	-79.6647	41.5079	X51A	-84.8574	34.5658
N56A	-78.2953	40.9171	Y49A	-86.4119	33.8577
N57A	-77.5509	40.7556	Y50A	-85.7347	33.8911
O59A	-76.1859	40.3114	Y48A	-87.1696	33.9131
N54A	-79.9892	40.9617	V54A	-81.9478	35.7771
N55A	-78.9862	40.7808	W54A	-82.1859	35.0857
O57A	-77.6354	40.2104			

Table S2. List of denoted “Appalachian” stations in Figures 5-6.

Mississippi Stations	Longitude	Latitude
T44A	-89.5896	37.086
U44A	-89.6863	36.5047
U43A	-90.4057	36.3693
V42A	-91.39	35.806
W42A	-91.5224	35.2732
W43A	-90.7061	35.0877
X41A	-92.5137	34.4949
X42A	-91.6262	34.5532
X43A	-90.8812	34.518
X44A	-90.1462	34.4998
Y41A	-92.6113	33.8807
Y43A	-90.9285	33.9121
Y44A	-90.2112	33.9618
Z42A	-91.9474	33.2739
Z43A	-91.2441	33.21
Z44A	-90.4322	33.2773
142A	-91.9457	32.5488
143A	-91.4036	32.7032
342A	-92.3249	31.3747
343A	-91.6169	31.2839
441A	-93.1898	30.7498
442A	-92.4314	30.7119
443A	-91.7809	30.7642
444A	-90.7463	30.7153
445A	-90.338	30.7303
541A	-93.1875	30.0596
542A	-92.5513	30.1247
543A	-91.8557	30.0856
544A	-91.1612	30.11
545A	-90.4894	30.0441
645A	-90.5966	29.4573

Table S3. List of denoted “Mississippi” stations in Figures 5-6.

6.2 Appendix of Chapter 4

This supplemental material includes one table. Table S1 includes Vs30 values at 744 TA stations.

STA	VS30 (m/s)	VS30_SIG (m/s)	STA	VS30 (m/s)	VS30_SIG (m/s)
058A	304.6	58.1	M43A	278.8	50
059A	325	50.7	M44A	358.8	42
059Z	291.6	57.4	M45A	307.4	77.6
060A	326.1	63.9	M46A	333.4	63.3
060Z	435.1	123.2	M47A	351.5	61.9
061Z	445.6	86.2	M48A	394.9	64
062Z	321.2	35.3	M49A	363.6	75.9
121A	477	76.8	M50A	317.7	71.6
140A	205.4	39.4	M51A	394	64.7
141A	303.2	51.4	M53A	466.2	83.8
142A	210.4	42.3	M54A	536.9	118.4
143A	181.2	32.7	M55A	407.5	58.8
144A	199.9	40.6	M57A	454.3	65.6
145A	241.1	47.2	M58A	577.1	220.2
146A	284.7	51.2	M59A	511	130.2
147A	524.2	93.4	M60A	878.9	231.3
148A	280.4	44	M61A	438.4	60.7
149A	284.5	46.1	M62A	467.7	93.8
150A	362	60.9	M63A	777.2	157.4
151A	361.8	69.1	M64A	741.1	129.7
152A	290.7	60.7	M65A	155.4	41.2
153A	337	43.5	M66A	235.9	42.7

154A	325.2	52.3	MDND	293	48.9
155A	432	64.3	MSTX	310.2	64.1
156A	269.9	50.7	N02D	406.3	74
157A	309.2	62.3	N15K	1139.6	195.6
158A	303.7	56.7	N16K	997.7	154.5
214A	710.2	122.8	N19K	3172.7	898.1
241A	278.2	50.7	N20K	1650.3	646.7
242A	186.8	43.6	N30M	723.2	182
244A	293.4	38.4	N31M	652.7	96.9
245A	336.4	55.1	N32M	345.9	52.4
246A	194	41.6	N36A	269.6	69.2
247A	267.5	49.2	N37A	262.8	54.9
248A	272.3	47.4	N38A	263.3	59.3
249A	364.8	45.9	N39A	337.6	71.6
250A	313.2	50.2	N40A	315	49.2
251A	291.7	41.9	N41A	349.6	64.6
252A	265.8	54	N42A	313.8	66.1
253A	279.2	53.5	N43A	361.8	68
254A	337.3	66.4	N44A	323.8	58
255A	388	70.7	N45A	346.9	101.6
256A	345.1	49.9	N46A	385.3	90.5
257A	248	49	N47A	414.3	87.6
341A	325.2	46.8	N48A	448.2	113.7

342A	296.8	39.2	N49A	712.3	158.3
343A	145.4	32.7	N50A	453.7	102.4
345A	288.7	49.3	N52A	359.9	59.4
346A	276.7	44.9	N53A	463.2	83.7
347A	257.3	48.1	N54A	439.4	86.2
348A	281.9	46.9	N55A	581.9	81.5
349A	281.6	50.1	N56A	447.6	77.1
350A	270.8	41.9	N57A	393	59.2
351A	322.4	54.2	N58A	955.5	161.6
352A	289.3	46.8	N59A	533.2	85.6
353A	375.3	70.4	N60A	825.5	179.3
355A	322	51.9	N61A	477.6	92.9
356A	277.1	38.4	N62A	381.4	63.3
357A	264.7	50.7	N63A	231.1	41.9
441A	237	42.5	O02D	478.5	96.6
442A	188	25.7	O03D	508.8	43.3
443A	167.2	39.5	O03E	569	80
444A	256.4	43.8	O14K	1505	322.6
445A	309.7	45.6	O15K	1875.1	507.2
446A	251.2	44.1	O16K	2014.8	406
447A	262	44.9	O17K	2301.1	376
449A	251.7	48	O18K	2624.2	1481.7
450A	303	52.7	O19K	434.1	75.4

451A	301.2	54.4	O20A	410.8	69.3
452A	405.2	72.8	O20K	1396.7	248.5
453A	276.9	51.8	O22K	428.3	71
454A	308.7	49.6	O29M	1280.9	519.8
455A	336.2	61.1	O30N	1076.1	238.4
456A	312.7	62.3	O37A	256	61.7
457A	272.7	32.3	O38A	265	57.1
541A	173	33.9	O39A	271.3	78.7
542A	174.1	36.2	O40A	388	101.6
543A	139.6	23.5	O41A	366.7	107.7
544A	120.1	23.4	O42A	266	62
545A	177.9	32.2	O43A	341.8	57.6
552A	346.6	53.8	O44A	356.2	46.4
553A	295.3	59.2	O45A	323.6	54
554A	393.3	44.9	O47A	402.4	57.3
555A	321.4	51.1	O48A	368.4	58.6
556A	354.1	64.3	O48B	393.2	45.3
557A	352.6	67.4	O50A	465.7	67.6
645A	128.8	21	O52A	473.4	91.9
646A	134.7	26.8	O53A	518.7	77.6
655A	565.1	102.9	O54A	399.7	58.6
656A	292.7	55.6	O55A	546.1	78.1
657A	296.8	64.2	O56A	724.8	103.6

658A	259.7	52.2	O57A	916	230.7
757A	351.1	70.3	O58A	844.8	164.8
758A	341.8	53.7	O59A	588.5	115.1
857A	343.4	63.7	O60A	823.6	153.9
858A	246.9	50.1	O61A	325.8	53.3
859A	313.3	52.4	P16K	268.3	46.1
957A	274.1	43.7	P17K	588.6	213.3
958A	409.1	77	P18K	479.2	62.8
959A	283.6	54	P19K	770.8	135.2
A04D	405.4	76.5	P23K	679.5	127.2
ABTX	360.9	43	P29M	653.3	163.9
B05D	519.1	71.2	P30M	1415.5	436
BGNE	228.2	45.8	P37A	368.2	63.7
C06D	267.6	60.3	P39B	337.9	74.3
C17K	1374.9	374.8	P40A	361.7	67
C23K	651.5	104.5	P41A	460.2	79.2
C24K	382.6	135.7	P42A	332.3	99.5
C36M	437	97.3	P43A	424.5	61.2
D03D	752	160.4	P44A	397	75.7
D04E	369.3	37.4	P45A	398.2	77.2
D25K	1259.1	239.1	P46A	323.7	68.6
D41A	397.5	82.9	P47A	456.2	68.4
D46A	353.4	86.3	P48A	326.8	75.9

D47A	603.6	106	P49A	527.3	80.3
D49A	312.2	73.1	P50A	283.9	49.1
D51A	479.1	113.5	P51A	370.5	77.4
D52A	640.6	128.6	P52A	479.6	61.4
D54A	773.2	77.2	P53A	415.2	90.8
D57A	559.8	105	P54A	661.8	131.5
D59A	278.6	65.5	P55A	526.8	79.2
D60A	932.8	170.8	P56A	646.4	90.9
D61A	610.6	142.7	P57A	375.3	58
D62A	771.5	137.5	P58A	891.5	148
D63A	791.7	141.2	P59A	254.6	53.1
E04D	371.4	48.9	P60A	430.6	97.4
E17K	2320	406	P61A	253.3	51.2
E18K	997.4	240.1	Q16K	400.4	83.6
E20K	847.4	279.9	Q17K	1028.9	146.4
E38A	340.7	63.4	Q18K	1193.9	169.1
E39A	492.6	63.7	Q19K	759.6	173.5
E40A	470.5	80.2	Q23K	478.2	151.2
E41A	359.6	103.5	Q39A	326.3	59.9
E42A	546.4	110.1	Q40A	260.9	41.6
E43A	571.4	90.1	Q41A	385.7	53.5
E44A	245.9	59.6	Q42A	304.4	54.6
E45A	284.4	47.6	Q43A	382.4	68.9

E46A	420.4	65.7	Q44A	398.2	74.9
E48A	314.7	64.3	Q45A	297.9	93.1
E50A	364.6	62	Q46A	418.7	77.8
E51A	783.3	219.2	Q47A	485.5	72.7
E53A	617.8	134.7	Q48A	336.4	34.7
E55A	273.3	60.6	Q49A	490	59.9
E57A	648.6	122.5	Q50A	753.1	127.1
E58A	640.6	94.3	Q51A	604.2	86.1
E59A	239.6	76	Q52A	373.5	60
E63A	887.6	132.9	Q53A	620.5	127.7
EPYK	392.2	89.6	Q54A	554	78.5
F04D	292.7	46.1	Q55A	469.8	60.7
F05D	306.6	54.9	Q56A	639.4	102.1
F24K	757.1	183.3	Q57A	792.4	133.6
F28M	720.6	121.3	Q58A	617.9	89.4
F30M	678.1	160.4	Q59A	298.3	53.7
F31M	495.6	121.3	Q60A	264.2	41
F37A	330.4	58.1	Q61A	260.4	45.4
F38A	320.6	71.8	R11A	896.1	126.1
F39A	356.1	81.8	R11B	1214.9	245.1
F40A	369.9	83.3	R16K	561.7	237.8
F41A	336.7	95.7	R17K	994.6	257.9
F42A	247.8	47.9	R18K	376.2	75.1

F44A	554.9	58	R31K	78.3	18.1
F45A	524.1	86.8	R38A	478.4	62.4
F46A	520.9	80.8	R39A	400.4	61.5
F48A	581.7	61.6	R40A	314.5	64.5
F49A	613.5	58.7	R41A	375.7	43.4
F51A	589.4	115.4	R42A	335.4	61.7
F52A	338.2	91.4	R43A	334	54.9
F55A	290	67	R44A	377.4	81.1
F57A	220.5	62.9	R45A	457.3	79.5
F59A	270.5	62.6	R46A	493.5	41.8
F60A	455.8	66	R47A	429.7	85.7
F61A	563.6	92	R48A	302.8	64.8
F62A	384.5	83.2	R49A	729.9	153.9
F63A	606.5	85.6	R51A	214.4	48.9
G03D	334.6	45.5	R53A	557.3	93.1
G05D	373.1	62.4	R54A	521	89.5
G19K	735	155.8	R55A	714.7	154.4
G21K	1442	408.4	R56A	547.5	68.4
G22K	461.9	61.8	R57A	465.2	86.1
G25K	360.8	58.8	R58B	299	64.1
G29M	1029.3	361.7	R59A	229.3	45.4
G30M	1279.6	310	R60A	297.7	43.1
G31M	934.3	458.4	R61A	248.5	34.7

G38A	397.4	81.7	S12K	933.5	206.7
G39A	381.5	81.6	S14K	300.3	45.6
G40A	423.3	120	S31K	572.8	87.1
G41A	298.8	66.8	S34M	490.7	87.6
G42A	370.2	90.1	S39A	528	75.5
G43A	606.6	85	S40A	454.1	91.5
G45A	508.6	98.1	S41A	357.1	63.1
G46A	244.6	40.2	S42A	346.3	42.1
G47A	379.2	69.4	S44A	382.2	62.8
G53A	382.2	97.1	S45A	457.1	77.8
G54A	640.6	138.4	S46A	492.2	54.4
G55A	590.3	87.7	S47A	446	52
G57A	541.3	101.9	S48A	1130.8	287.9
G58A	286.8	29.3	S49A	808	131.2
G60A	614.2	91.8	S50A	404	51.9
G61A	876.5	98.7	S51A	526.9	56.7
G64A	1381	547.8	S52A	352.4	52.5
H04D	359.2	68.1	S53A	337.3	46.3
H17A	358.3	58.6	S54A	509.6	91
H19K	532.7	155.3	S55A	588.9	76
H20K	2357.5	715.9	S56A	214.5	56.8
H23K	960.6	406.4	S57A	313.5	66.7
H38A	424.9	49.2	S58A	171.3	35.8

H39A	264.4	56	S59A	265.8	41.4
H40A	537.8	109	S60A	247.4	37.7
H42A	281.3	70.1	S61A	283.8	45
H43A	613	72.6	SFIN	478.1	58.8
H45A	271.1	56.7	SPMN	303.6	67.3
H46A	338.5	70.8	SUSD	258.3	41
H47A	264.5	48.4	T33K	77.2	11.1
H48A	216.2	48.4	T35M	716.2	158.2
H52A	350.9	86.3	T38A	499.2	96.4
H53A	617.6	140	T39A	451.3	91.1
H55A	518.8	87.2	T40A	675.7	148.1
H56A	340	56.6	T41A	393.9	77.4
H59A	616.8	118.6	T42A	513.8	66.2
H60A	428.6	69.2	T43A	352.4	67.2
H62A	543.5	135.1	T44A	247.8	53.7
H63A	305.6	83.3	T45A	223.4	33.1
H64A	857.4	159.8	T46A	323.3	51
H65A	338.1	90.1	T47A	439.7	59.1
H66A	923.3	241.4	T48A	423.5	83.7
HARP	759.9	221.7	T49A	369.9	69.9
HDA	392.8	67.6	T50A	364.6	46.1
I02D	294.6	28.5	T51A	466.9	81.8
I02E	447	129.8	T52A	348.3	39.9

I03D	336	35.3	T53A	479.7	55.8
I04A	418.7	73.4	T56A	365.1	67.1
I05D	520.8	92.8	T57A	348.3	65.2
I20K	257.7	34.1	T58A	303.9	44.3
I21K	543.3	75.8	T60A	234.6	30.2
I23K	722.1	121.5	TCOL	289.6	69
I26K	547.6	92.5	TIGA	297.7	50.4
I29M	257	63.9	TPFO	493.2	76.6
I30M	812.6	220.8	TUL1	963.5	188.2
I36A	286.6	53.3	U33K	2055.7	582.2
I37A	306.4	69	U35K	192.5	45.7
I39A	358.4	49.2	U39A	370.4	55
I40A	876.6	181	U40A	509.6	113.7
I41A	307.5	82.7	U41A	423.6	89.4
I42A	791.8	254.2	U42A	527.9	146.4
I43A	746.3	224.1	U43A	216.3	34.5
I45A	281.6	49.8	U44A	201.8	44.7
I46A	326.4	37.3	U45A	293.8	41.6
I47A	427.4	80.3	U46A	270.8	43.4
I48A	316.2	65.6	U47A	391.3	68.8
I49A	557.1	131.5	U48A	385.1	70.3
I51A	539.5	61	U49A	458.3	91.1
I52A	347.1	79.3	U50A	555.1	108.2

I53A	382.5	58.9	U51A	353.3	68.2
I55A	715.3	132.6	U52A	297.8	50.2
I57A	647.1	78.8	U53A	331.6	56.2
I58A	298.1	37.2	U54A	342.7	53.5
I59A	514.9	64.4	U56A	175.2	34.4
I62A	587.5	105.3	U57A	294.4	40.7
I63A	548.1	74.9	U58A	261.5	51.9
I64A	373.8	33.6	U59A	299.3	65.7
J01D	336.2	53.5	U60A	287.7	46
J01E	290.2	43	U61A	237.7	49
J04D	222.4	41.8	V35K	1339.3	343.2
J05D	407.4	47.4	V39A	578.5	207.7
J17K	1125.3	608	V40A	609.2	70.3
J19K	1048.6	409.8	V41A	562.9	84.8
J20K	1153	548.4	V42A	286	51.2
J25K	1229.1	357.1	V43A	226	54.2
J29M	347.1	60.7	V44A	215.3	46.8
J29N	348.4	58.6	V45A	241.1	51.6
J36A	304.7	80.1	V46A	526.4	98.4
J37A	251.1	64.3	V47A	371	61.7
J38A	295.3	91.3	V48A	457.4	108.1
J40A	393.2	53.3	V49A	379.9	84.5
J41A	342.9	31	V50A	555.9	116

J42A	704.6	186.7	V51A	592.2	60.7
J43A	830.8	133.9	V52A	566.7	76.3
J45A	295.6	70.2	V53A	532.1	113.8
J46A	289.1	65.5	V54A	390.6	69.7
J47A	387.4	77.9	V55A	365.4	67.9
J48A	400.6	48.9	V56A	430.9	122.1
J49A	363.6	51.7	V57A	553.5	143.2
J52A	538.2	124.4	V58A	319.6	83.4
J54A	368.6	97.2	V59A	435.8	80.8
J55A	490.7	88.9	V60A	252.7	38.5
J57A	547	71.7	V61A	308.8	63.2
J59A	602.3	103.4	V62A	209.5	54.3
J60A	913.4	219.3	W18A	406.6	92.7
J62A	502.8	69.2	W39A	460.1	61.9
K02D	599.6	96.4	W41B	476.6	92.5
K04D	310.8	53.7	W42A	198.3	69.9
K15K	1554	545.1	W43A	223.2	46.4
K22A	317.1	62.6	W44A	246.8	52.9
K24K	645.7	152.4	W45A	224.3	42.4
K29M	1038.7	167.1	W46A	333.2	64.9
K36A	314.9	77.2	W47A	423.7	84.6
K37A	316.1	71.6	W48A	519.7	89
K38A	315	51.2	W49A	489.7	126.1

K39A	310.3	56.8	W50A	639	86.3
K40A	412.6	80.7	W51A	343.1	57.7
K41A	598.2	120.3	W52A	325.1	70.7
K42A	390.5	85.6	W53A	317.6	66.9
K43A	558.7	130.9	W54A	430.3	89.9
K46A	416.5	73.4	W56A	682	87.9
K48A	364.1	86.1	W58A	361	71.4
K49A	411.1	70.7	W59A	255.1	47.4
K50A	261.6	57.2	W60A	284.6	54.7
K51A	296.2	53.8	W61A	283.8	62.5
K52A	327	76.6	WHTX	429.3	78.9
K54A	619.8	91.2	X39A	622.3	57.9
K55A	698.1	103.3	X40A	467.1	87.6
K56A	533	104.8	X41A	325.7	48.7
K57A	597.2	93.5	X42A	218.4	45.5
K58A	543.1	78.2	X43A	201.2	42.5
K59A	838.9	149.2	X44A	244.1	38.5
K60A	304.7	92.1	X45A	311.1	41.9
K61A	278	58.3	X46A	320.6	63.7
K62A	596.7	83.4	X47A	487.1	64.3
K63A	940	224.1	X48A	629.2	106.6
KMSC	242.1	50.5	X49A	533	104.2
KSCO	272.2	46.6	X50B	434.2	44.9

L02D	584.9	127.2	X51A	315.3	55
L04D	471.5	87.2	X52A	343.6	76.6
L15K	1669.1	729.3	X53A	226.2	50.3
L17K	1141.7	556	X54A	341.4	64.8
L19K	797.1	230.3	X55A	283.2	48.6
L20K	238	71	X56A	239.6	53.8
L26K	349.2	27.9	X57A	311.7	60.7
L27K	715.8	106	X58A	342.8	58.3
L29M	870	298.5	X59A	268.4	53.6
L36A	313	81.7	X60A	224.5	54.6
L37A	328.4	65.1	Y22D	307.9	44.3
L39A	316.4	43	Y22E	303.9	53.6
L40A	346	59.9	Y40A	451.6	87.5
L41A	359.8	84.1	Y41A	282.7	51.1
L42A	337.4	61.8	Y43A	193.2	41.4
L43A	431.1	91.6	Y44A	218.7	42.2
L44A	364.8	104.8	Y45A	206.1	38.5
L47A	316.9	58.9	Y46A	332.8	34.2
L48A	460.8	79.4	Y47A	351.9	74.6
L49A	396.7	87.9	Y48A	514.1	83.8
L50A	450	112.5	Y49A	575.1	107.6
L53A	399.2	66.8	Y50A	368.1	64.9
L55A	564.6	76.9	Y51A	296.4	44.9

L56A	567.7	72.1	Y52A	417.1	71.1
L57A	714.2	129.7	Y53A	279.8	60.2
L58A	713.5	138.8	Y54A	580.1	53.6
L59A	315.4	112.8	Y55A	485.4	84.8
L60A	754.7	151	Y56A	324	53.7
L61A	570.8	50.5	Y57A	296.9	51.1
L61B	654.5	97.2	Y58A	381.1	52.9
L62A	274.8	53.9	Y59A	204.6	59.1
L63A	481.1	55.7	Y60A	366.7	61.9
L64A	352.5	98.1	Z40A	330.6	61.4
L65A	236.6	28.8	Z41A	272.1	46.6
M02C	641.1	103.5	Z42A	289.3	45.5
M04C	364	72	Z43A	217.1	44
M15K	1645.2	221.4	Z45A	233.7	38.8
M17K	993.8	227.2	Z46A	330.6	67.6
M19K	575.9	107.5	Z47A	271.5	55.6
M22K	359.6	69.2	Z48A	450.9	74.4
M23K	250.4	46.8	Z49A	391.7	80.1
M24K	452.2	55.2	Z50A	451.5	91.9
M26K	799.1	112.5	Z51A	220.4	51.6
M27K	2136.4	498	Z52A	290.3	44
M31M	546.3	96	Z53A	244.7	53.6
M37A	267.8	67.1	Z54A	406.6	101.2

M38A	306.5	53.1	Z55A	276.8	51.1
M39A	286.8	66.3	Z56A	253.4	52.3
M40A	309.1	60.9	Z57A	428.2	74.5
M41A	309.8	57.9	Z58A	345.8	42.7
M42A	291.8	81.7	Z59A	306.7	47.6

Table S1. List of estimated Vs30 and uncertainties of all 744 TA stations.